Development of High-performance Hot-deformed Nd-Fe-B Permanent Magnets by the Eutectic Grain Boundary Diffusion Process

Lihua LIU

February 2018

Development of High-performance Hot-deformed Nd-Fe-B Permanent Magnets by the Eutectic Grain Boundary Diffusion Process

Lihua LIU
Doctoral Program in Materials Science and Engineering

Submitted to the Graduate School of
Pure and Applied Sciences
in Partial Fulfillment of the Requirements
for the Degree of Doctor of Philosophy in
Engineering

at the
University of Tsukuba

To my parents

Xingkou Liu and Lan Li,

who made everything possible

Acknowledgements

When I first started the study in Prof. Kazuhiro Hono's lab, I had no idea that my research journey would last for more than 5 years. And I certainly didn't expect to pursue for the Ph.D. degree and even make the research about magnets as my life-long career. Along the way, I am very lucky to have had the brilliant supervisor, Prof. Kazuhiro Hono throughout my journey. The discussions and open conversations with you have been very empowering which I personally think are helping me to find things to change and modify. It was also the time when I can step out of the research project for a while and think broadly. Along with the sweet talking and invaluable advice, it's most possible that I would find the necessities to push harder from the current efforts I've made. In that sense, these discussions are actually keeping me motivated and activated, not staying in the comfort zone, but rather, to aim for more challenging target. I cannot express in words how much you have given me in terms of time and intellectual wisdom. Your support and thoughts have enabled me to crystallize much more refined research plans.

I was also privileged to be mentored by Dr. Sepehri Amin Hossein. You are the person who has been supporting me not only in the research but also in ways of thinking, tackling problems and finding balance between research and life. Thanks to you, I could be able to think diversely and to modify and improve on the ways to solving problems. It is also thanks to you that I learned as hard it may be in the working environment, saying no is, in fact, the right thing to do. The conversations we had ranging from researches, friendship, to career designs have inspired me to do better. Your suggestions helped me find the way to correlate the career plans and personal life goals. I couldn't have fulfilled this thesis without you.

I would also like to give my sincere acknowledgement to my current and former group members. The Research Center for Magnetic and Spintronics Materials has been very inclusive and diverse group. Being "inclusive" is because of its internal connections among staff members, post-doctors, graduate students and the supporting technicians. People in this group who have their own expertise are very accessible and helpful. Another important thing was probably the popularization of the English language here. For me, of course, it is more about our Chinese group members; it is you guys that made this 5-year long journey accompanied and meaningful. It is those get-togethers within the Chinese crews made every Chinese traditional holiday feel belonging. Being "diverse" is originated from the mixtures of different culture background of our group members. Despite the diversity in countries and languages, this research center had the welcoming atmosphere and it valued individuals' roles. More importantly, everyone is encouraged to think straight and talk straight, to stand up and talk loud. This is also the reason I didn't feel excruciating even though I had been the only female Ph.D. student for almost 5 years. The working experience with all of you who pledged the allegiance to researches has inspired my curiosity and tenacity to continue my research journey further in my life.

There are a few people I want to give special thanks to: Dr. Tadakatsu Ohkubo, for giving me countless technical trainings and superb advice. Aside from being our group leader, you are also a big supporter for me.

“Please call me if you have encountered any problems” really gave me strengths to handle those super-expensive unfamiliar instruments because I know you will always have my back out there. “Everyone is expert at something, so keep mind open and be prepared to be amazed” as I feel self-conscious on some occasions. Ohkubo san, thanks for your help and those warm words.

I am grateful for the help and accommodations from the following individuals:

Taisuke Sasaki, Jun Uzuhashi, Satoshi Hirosawa, Lan Ma, Pohan Cheng, Guanxiong Qu, Bumjin Bae, Takao Iitsuka, B.S.D.Ch.S. Varaprasad, Scheike Thomas, Marko Soderžnik, Jason P. Hadorn, Takahiro Akiya, Yoshiya Toyooka, Uma M. Rao Seelam, Seok Namkung, Felicia Angelina, Ayumi Yoshino, Tomoka Yokoyama, Xin Tang, Tae-Hoon Kim, Xiandong Xu, Ruma Mandal, Hwachol Lee, Ye Du, Jun Liu, Yukiko Maeda, Jian Wang, Qingying Xiang, Xuefei Miao, Hiroyuki Sebata, Yusuke Hirayama, Shigeyuki Hirayama, Takao Furubayashi, Yukiko Takahashi, Jiangnan Li, Almet Yagmur, Junko Kawai, Hun Seok Kim, Iktiar, Weibin Cui, Peng Sheng, and Songtian Li. I am very fortunate to have you throughout my entire study.

To my mom and dad: thanks for letting me go ahead with my decisions to study for the Ph.D. degree in Japan and pursue things I had been dreaming of. I am forever in your debt. You have given me tremendous mental support to make through those anxiety and depression time. I now understand the correlation between practicing compassion outside with how much you are able to treat yourself kindly from inside. You both make me believe that I can do something with this life. My thanks also go out to my elder sister, Aihua, for spiritual support. You are indeed always the role model for me (I think my long journey on materials science and engineering nucleated together with your footprint), and Yijun Xie, my dear friend, who, by sharing your own thoughts and wisdom on researches encouraged me to walk this far.

I also own the special thanks to the joint education system of Junior Researchers between Tsukuba University and National Institute for Materials Science (NIMS). This is the platform that requires no Japanese proficiency and offers the chance to study in the national laborites. Application for the junior research assistantship is the starting point and is the decision that I’ve made for which I’m now feeling very much grateful.

Last but not least, great acknowledgement should also be given to the financial support provided by Japan Science and Technology Agency (JST), CREST and Elements Strategy Initiative Center for Magnetic Materials (ESICMM).

Lihua LIU

January 5, 2018

Development of High-performance Hot-deformed Nd-Fe-B Permanent Magnets by the Eutectic Grain Boundary Diffusion Process

Abstract

With the most outstanding magnetic energy product $(BH)_{max}$, Nd-Fe-B permanent magnets have been the state-of-art hard magnets which have wide applications in environmental-friendly technologies, such as hybrid vehicles and wind turbines. For the time being, almost 95% of the theoretical limit for $(BH)_{max}$ (based on the saturation magnetization M_s of the $Nd_2Fe_{14}B$ phase) can be achieved for current commercial sintered Nd-Fe-B magnets. However, the magnets used in practical motors of hybrid vehicles would suffer from demagnetization from electric or magnetic circuit and thermal degradation, coercivity is extremely important for a stable functioning of the magnets. Indeed, the coercivity above 0.8 T at the temperature of about 150^{o}C is needed. Due to the relatively large temperature degradation of coercivity of sintered magnets, high coercivity of around 3 T must be attained at room temperature by substituting part of Nd with heavy rare-earth elements (HREEs) such as Dy and Tb in Nd-Fe-B based sintered magnets. However, the alloying of Dy and Tb also induces a reduction of $(BH)_{max}$ which is caused by the antiparallel exchange coupling between Dy (or Tb) and Fe atoms in the $(Nd,Dy)_2Fe_{14}B$ unit cell. Moreover, considering the scare natural reserve of these HREEs, it's vital to develop HRE-free or HRE-saving technique to fabricate the high-performance Nd-Fe-B magnets.

Many research efforts have been focusing on the refinement of the grain size of $Nd_2Fe_{14}B$ phase, succeeding in enhancing the coercivity of sintered magnets. On the other hand, anisotropic Nd-Fe-B hot-deformed magnets prepared from melt-spun ribbons have platelet-shaped grains with an average grain size of ~250 nm in length and ~100nm in width. Their temperature dependence of coercivity is substantially improved compared to that of Nd-Fe-B sintered magnets due to the reduced stray field. In addition, with improving the crystallographic texture, the remanent magnetization of anisotropic hot-deformed magnet can reach ~1.4 T or higher that is comparable to commercial sintered magnets. Hence, anisotropic Nd-Fe-B hot-deformed magnets have the potential to be used as Dy-free Nd-Fe-B permanent magnets in traction motors of electric or hybrid vehicles. However, the room temperature coercivity of real HRE-free hot-deformed magnets is limited to around 1.8 T, the main reason of which was addressed as the highly enrichment of ferromagnetic element in the intergranular phase and suggest that improvement of coercivity can be realized if chemical composition of the intergranular phase can be successfully modified to be non-ferromagnetic. There has been a revived interest in developing HRE-free or HRE-lean Nd-Fe-B hot-deformed magnets with high coercivity by the grain boundary engineering through the eutectic grain boundary diffusion process using Nd-rich eutectic alloys.

It is necessary to make the statement that the word “diffusion” used in this thesis has different meaning as the traditional term work to avoid the misconception. As the diffusion in this thesis refers to the infiltration process of the melt eutectic alloys through the grain boundaries, it mainly includes the solidification process along with the cooling which is a totally different behavior from diffusion which describes the process of mass transportation.

Coercivity, as extrinsic property, is closely related to the microstructure of the grain boundary as well as the interface feature. In this thesis, emphasis is placed on the optimization of the eutectic grain boundary diffusion process, in particular, searching for the most ideal diffusion source which gives significant coercivity enhancement with relatively small sacrifice in remanence. Meanwhile, the characterization of the Nd-rich intergranular phase as well as the interface is also carried out to understand the mechanism of coercivity enhancement, which is also critical for assisting the optimization.

In previous work, the improvement of coercivity has been achieved by applying the eutectic GBDP to the hot-deformed Nd-Fe-B magnets using Nd-Cu eutectic alloy as the diffusion source. However, systematic work is not yet exploited in terms of other Nd-rich eutectic alloys. Various RE-TM eutectic alloys for the eutectic grain boundary diffusion process were investigated. It is found that Nd-Al is most effective in view of room temperature coercivity as a result of the formation of thick Nd-rich intergranular phase and the improved anisotropy field because of Al partitioning into the matrix phase. However, in view of the high temperature coercivity, Nd-Cu alloy has been shown to be the best diffusion source. The Nd-Cu diffusion-processed magnet shows $\mu_0 H_c$ of 0.67 T at 200 ^{o}C while Nd-Al diffusion-processed magnet exhibits only 0.6 T at 200 ^{o}C while its room temperature coercivity is higher than that of Nd-Cu diffusion-processed sample The observed abnormal grain growth due to the high heat treatment temperature in Nd-Al diffusion processed magnets and the reduced Curie temperature due to Al dissolving to the main phase were believed to be the reason for the poorer thermal stability of Nd-Al diffusion processed magnets.

On the other hand, since the highest remanent magnetization is given by a perfectly aligned (magnetic texture), fully dense magnet, for example, the single crystal, it’s critical to find the balancing or compromising point between coercivity and remanence. Hence, the solution needs to be found to realize a significant enhancement in coercivity while retaining relatively high remanent magnetization. Demonstration of the merit of a quaternary $Nd_{62}Fe_{14}Ga_{20}Cu_4$ alloy as the diffusion source for the eutectic grain boundary diffusion process is made in comparison with ternary $Nd_{80}Ga_{15}Cu_5$ alloys. For $Nd_{62}Fe_{14}Ga_{20}Cu_4$ diffusion processed magnets, when the same level of coercivity improvement from 0.9 T to 2.2 T is attained as that of Nd-Ga-Cu diffusion processed one, much smaller reduction of remanence from 1.50 T to 1.30 T is observed. Similarly, M_r/M_s of the initial sample and the samples processed with $Nd_{62}Fe_{14}Ga_{20}Cu_4$ and $Nd_{80}Ga_{15}Cu_5$ were 0.94(6), 0.93(4) and 0.91(7), respectively, suggesting that the sample processed with $Nd_{62}Fe_{14}Ga_{20}Cu_4$ retains stronger c-axis texture after the diffusion process. The higher alignment of $Nd_2Fe_{14}B$ grains is also observed in BSE SEM image of $Nd_{62}Fe_{14}Ga_{20}Cu_4$ diffusion processed magnets. Moreover, the formation of Nd-rich intergranular phase is rather uniform in the sample processed with $Nd_{62}Fe_{14}Ga_{20}Cu_4$ while it has an abrupt drop in the areal fraction in $Nd_{80}Ga_{15}Cu_5$ processed sample from regions near surface to the center.

This indicates a more efficient diffusion depth of $Nd_{62}Fe_{14}Ga_{20}Cu_4$ used as diffusion sources. Indeed, when the diffusion experiments were extended by varying the amount of applied diffusion sources, the less susceptible decrement in remanence with the coercivity enhancement from initial hot-deformed magnets clearly demonstrates the merit of $Nd_{62}Fe_{14}Ga_{20}Cu_4$ as diffusion sources in terms of limiting the degradation of remanence while realizing the coercivity enhancement by the eutectic grain boundary diffusion process. It can be postulated that $Nd_{62}Fe_{14}Ga_{20}Cu_4$ enables less applied diffusion source to realize the same level of coercivity enhancement compared to $Nd_{80}Ga_{15}Cu_5$.

The effect of two HRE-alloyed diffusion sources Nd-Dy-Al and Nd-Tb-Cu alloys on coercivity and thermal stability of the hot-deformed Nd-Fe-B magnets were investigated, respectively. For Nd-Dy-Al diffusion processed magnets, the coercivity increases from around 1.30 T to 2.80 T with the reduction of remanence from 1.50 T to 1.30 T. On the other hand, Dy-vapor diffusion process which was performed at 900^{o}C exhibited the deterioration of coercivity from 1.30 T to 1.0 T and the catastrophic grain growth into the magnitude of micrometers. The significant coercivity improvement can be related to the formation of Nd-rich intergranular phase and Dy-rich shell structure on the surface of $Nd_2Fe_{14}B$ grains as well as Al dissolving in the matrix grain. Temperature coefficient of coercivity (β) for the hot-deformed, and the Nd-Cu, Nd-Al, Nd-Dy-Al diffusion-processed samples was calculated to be -0.47, -0.40, -0.43 and -0.39%$^{o}C^{-1}$, respectively. The improvement of thermal stability of Nd-Dy-Al diffusion processed magnet, despite the observed abnormal grain growth as well as Al dissolving into matrix phase is believed as the effect of Dy-rich shell structure. For Nd-Tb-Cu eutectic grain boundary diffusion process, $Nd_{60}Tb_{10}Cu_{30}$ and $Nd_{60}Tb_{20}Cu_{20}$ alloys were attempted as the diffusion sources. It is confirmed that with Nd-Tb-Cu alloys applied as diffusion sources the significant coercivity enhancement could be achieved without large decrease of remanence. The coercivity increased from 0.87 T to 2.35 T and 2.57 T for $Nd_{60}Tb_{10}Cu_{30}$ and $Nd_{60}Tb_{20}Cu_{20}$, with a small degradation in remanence from 1.50 T to 1.44 T and 1.38 T, respectively. In the meanwhile, the temperature coefficient of coercivity β was improved from -0.478 %$^{o}C^{-1}$ to -0.379 and -0.315 %$^{o}C^{-1}$, respectively. Microstructure observation indicated $Nd_2Fe_{14}B$ grains retained in highly (001) texture for both diffusion processed magnet. No obvious Tb-rich shell structure could be seen for $Nd_{60}Tb_{10}Cu_{30}$ diffusion processed magnet; only an enhanced contrast at the interface between the grain boundary and $Nd_2Fe_{14}B$ phase was confirmed in the HAADF STEM images. For $Nd_{60}Tb_{20}Cu_{20}$ diffusion processed magnet, formation of Tb-rich layers which mainly located at side surfaces of the matrix grains was observed, which should contribute to the improvement of temperature dependence of coercivity. The anisotropic formation behavior of HRE-rich shell structure has also been observed in Nd-Dy-Al diffusion processed magnet and seems the common feature of the hot-deformed magnet diffusion processed with HRE-alloyed diffusion sources.

From the practical viewpoint, this eutectic grain boundary diffusion process will eventually be employed to the production line of commercial hot-deformed magnets. When it comes to bulky samples, the limited diffusion depth would be a critical issue to overcome for establishing the eutectic grain boundary diffusion process as an ideal technique for the development of high-performance hot-deformed Nd-Fe-B permanent

magnets. The eutectic grain boundary diffusion process applied to the hot-deformed Nd-Fe-B magnets in the size of 7×7×5.6 mm^3using $Nd_{60}Dy_{10}Cu_{30}$ alloy as the diffusion source has been investigated. The average coercivity was improved from 1.4 T to 2.52 T, with the remanence degradation from 1.40 T to 1.25 T. There exists a large coercivity distribution of the diffusion-processed magnet from surface to the center region. The coercivity measured for the surface part of the magnet shows the coercivity of 2.70 T while 2.30 T for the center. The remanence also varied from 1.19 T to 1.32 T, respectively. From microstructural analysis, in the region close to surface better isolation between $Nd_2Fe_{14}B$ grains by the Nd-rich intergranular phase were observed. No Dy-rich shell can be observed both for surface and center regions in the diffusion processed magnet. In the surface region, Dy is mainly partitioning in the Nd-rich intergranular phase and substitutes Nd on the very surface layer of the $Nd_2Fe_{14}B$ grains. However, in the center region of the magnet, Dy can no longer be detected, as analyzed with the atom probe. This suggested the limited diffusion depth of the eutectic diffusion process that could be the crucial factor of applying this technique as the method to develop high-performance hot-deformed Nd-Fe-B magnets in large size. The effect of expansion constraint during the heat treatment was demonstrated by comparing the diffusion process using Nd-Ga-Cu alloy as the diffusion source. For the Nd-Fe-B hot-deformed magnet in the size of 5×5×4 mm^3 in the Nd-Ga-Cu eutectic diffusion process, when the expansion freedom was 0.1 mm, the remanent magnetization degradation was from 1.51 T to 1.32 T with the coercivity improved from 1.2 T to 2.03 T. While the magnet processed without applying expansion constraint exhibited the significant deterioration in remanent magnetization to 0.98 T. The in-depth characterization showed the improved distribution of Nd-rich intergranular phases from surface to center regions indicating a larger diffusion depth was achieved under the expansion constraint. The improved (001) texture of $Nd_2Fe_{14}B$ phase was also observed in the Nd-Ga-Cu diffusion processed magnet under partial expansion constraint with 0.1 mm expansion constraint. On the other hand, the fully constraint induced a totally destroy of alignment of $Nd_2Fe_{14}B$ grains from the surface region which was in direct contact of the constraint plate.

This thesis will focus on the optimization and investigation of the eutectic grain boundary diffusion process on hot-deformed Nd-Fe-B magnets. The term “diffusion” used in this thesis, however, is only from inhabitations for the processing routes commonly referred in this community. It has obviously large difference with the conventionally deceived “process of diffusion”. To avoid the misconception, the author wants to draw readers’ attention that the diffusion process in this thesis is more close to “infiltration” with a bulk mass transfer process. The regular diffusion process, on the other hand, as one of the most fundamental processes by which a system (material) attempts to realize phase transformation usually comes along without bulk motion.

Keywords: NdFeB, coercivity, diffusion, grain boundary phase, heavy rare earth, interface microstructure

TABLE OF CONTENTS

Page

1 Chapter 1 Introduction

1.1 General introduction

The earliest record of magnets can be tracked back to BC 3 to 4 centuries, reported by ancient Chinese in historical books of Guiguzi and Lushi Chunqiu, as the discovery of the navigational compasses “loadstone”. Loadstone is mainly comprised with ferroferric oxide (Fe3O4) from the magnetite ores, which were first found in the Greek province of Magnesia. This is also how “magnet” derived its name.

Magnetic researches have been including both basic physics prospective and technological aspects. Fundamental understanding of magnetism is built up on the basis of quantum mechanics, offering qualitative and quantitative descriptions of various sources of fields, including uniform external field, magnetic dipole filed, and crystalline electric field, also dealing with determination of exchange interactions or response of different systems (materials) to magnetic fields. Reviewing the history of magnetism and magnets has revealed the fact that many progresses made on the magnetic materials have been related more to metallurgists and chemists than to the development of physics. However, the understanding from susceptibility measurement, nuclear magnetic resonance, optical or neutron scattering processes is providing very important insights into new magnetic phenomena and has been advancing the revolution in information, geography, medical diagnosis, et al.

In fact, both the fundamental understanding and the intense technological activity have spurred the evolution in permanent magnet materials of this century, especially in the last two decades since rare-earth elements were alloyed with transition metals. Permanent magnets, also referred as hard magnets are magnetic materials that can easily saturated with applied field and can retain their magnetism when the field is removed. A broad hysteresis loop (or technical magnetization curve) is the typical feature of permanent magnets. It shows how the magnet response to external magnetic field and contains the technical terms of the saturation magnetization M_s which is the possible maximum intrinsic magnetization, the remanence M_r, which refers to the remanent magnetization when the field goes to zero and the coercivity H_c that is usually defined as the reverse field that reduces the magnetization to zero in large-coercivity materials. The maximum energy product $(BH)_{max}$ which is a key measure factor of permanent magnets, can also be derived from the hysteresis loop. It provides a measure of the largest field that a unit magnet is capable of producing outside. Theoretical limit of $(BH)_{max}$ is defined as $(4\pi M_s)^2/4$. The magnet development is indeed a longstanding process of progressively enhancing energy product that exceeds previous values. Figure 1-1 [1] shows the historical evolution of energy product value for different generations of permanent magnets in the past century. It started from ≈ 1MGOe for conventional permanent magnets steels, about 3MGOe for hexagonal ferrites, increasing to around 5~10 MGOe for Alnicos and finally reached ≈ 56MGOe for neodymium-iron-boron magnets during the past two decades.

In the early 1930s, the Alnico alloys with the typical composition of Fe-Al-Ni-Co replaced the magnet steels, and reached a top property by the development of anisotropic columnar shaped alnico 9 which possess

the energy product of 10 MGOe. These alloys have very high Curie temperature T_c of around 850°C which enables its use at high operating temperature, even in modern transformers and inductors. However, the main disadvantage is they have low intrinsic coercivity ${}_iH_c$ which comes from the shape anisotropy of the rod shaped Fe-Co phase which limits the applications against large demagnetizing fields. Moreover, to further exploit the effect from shape anisotropy, they are generally manufactured into horseshoe or long cylinder configurations which also limit their applications due to the lack of flexible machinability.

In 1966, the combination of rare-earth (RE) and transition metal (TM) emerged a new generation of permanent magnets, which takes the advantage of large anisotropy of RE and high magnetization of TM. The sintered $SmCo_5$ magnets achieved the energy product of over 20 MGOe in 1969. And later the Sm_2Co_{17} based alloy showed the energy product higher than 30 MGOe and even ideal coercivity through careful control of the microstructure which is typically composed with Sm_2Co_{17}-type cell and the cell boundaries of $SmCo_5$-type phase. Sm/Co based magnets are the most ideal magnets so far with high coercivity and large energy product; however, the use of much lest abundant light RE element Sm and the strategically important element Co has impeded their commercialization and the sales. Despite the economic constraints on the Sm/Co based magnets, the possibility of deriving large uniaxial anisotropy from the combined influence of exchange and crystalline electric field on RE ions has provoked the investigations for alternative RE-TM systems.

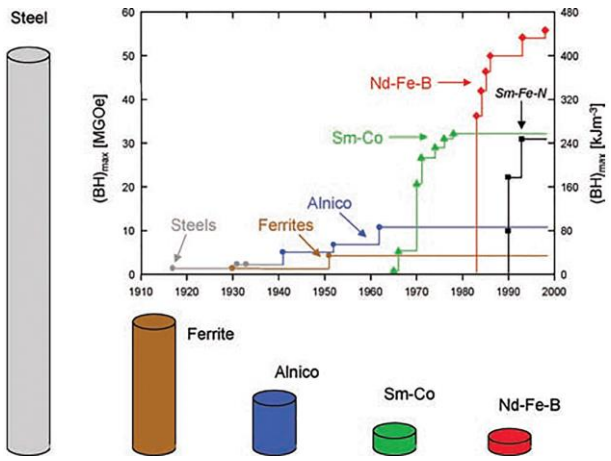

Fig. 1-1 Development in the energy density $(BH)_{max}$ at room temperature of hard magnetic materials in the 20th century and presentation of different types of materials with comparable energy product [1].

In 1984 discovery of the superior magnetic properties of Nd-Fe-B permanent magnets was made independently by Sumitomo Special Metals in Japan [2] and General Motors of USA [3] through powder metallurgical processing route and melt-spinning techniques, respectively. Apart from the obvious economic advantage of Sm/Co based magnets, the intense technological activity centering on Nd-Fe-B permanent magnets is because of its excellent intrinsic magnetic properties with M_s of 1.61 T and H_a of 7.3 T. The optimization of alloy compositions and processing conditions has succeeded to achieve the maximum energy

product of ~56 MGOe in the industrial grade of Nd-Fe-B permanent magnets. The report by Hitachi metals succeeded in producing Nd-Fe-B magnet with the energy product of ~61 MGOe, near 95 % of its theoretical limit based on the $Nd_2Fe_{14}B$ phase. There is an increasing emphasis on improving the efficiency of electricity transmission and reducing fuel consumption and emissions, along with the customers' demand for comfort and high-quality driving experience, during the last two decades, the automotive utilizing electric motors market went through a phenomenal expansion. Permanent magnet motors are capable to provide a large starting torque and wide speed range at constant power. If we bring the really big numbers, in the developed countries, such as USA, nearly one third electricity is consumed by industrial sectors; out of that, 65% is used by electric motor drives [4]. Someone calculates that a 1% improvement in efficiency means savings of hundreds of millions of dollars and a reduction in CO_2 emissions of nearly 2.2 million metric tons of carbon equivalent. From the prediction by IEA [5] the total stock of xEV (including Gasoline-Battery Car, Battery-Electric Vehicle, Plug-in Hybrid Car and Hybrid Car) in 2016 is 10 million; it will reach 25 million by the year of 2020 and exceed 200 million till 2040. France and United-Kingdom even set the national electric car deployment targets as zero new-registration sales of gasoline cars.

Each magnet is designed as to generate the same field at a same reference point from the magnet surface. With the most outstanding magnetic energy product, Nd-Fe-B magnets have been the state-of-art hard magnets which satisfy the large starting torque and wide speed range at constant power of the hybrid vehicle motors, with the minimum volume utilization. Generally, the major driving force for research and development of Nd-Fe-B permanent is the need for maximized energy product at various operating temperatures. Although the basic function of permanent magnetic materials used in electric machines is to provide magnetic flux, which requires a saturation magnetization ($4\pi M_s$ in cgs units or $J_s = \mu_0 M_s$ in SI units) as high as possible. However, for the application against different kinds of demagnetizing fields, including field demagnetization from the electric or magnetic circuit and thermal degradation due to the operating temperature, coercivity is extremely important since these two demagnetization factors work continuously while motors are running.

Two coercivity parameters are used to measure the magnetic hardness: one is intrinsic coercivity, H_{ci} (or ${}_jH_c$), and the other is normal (or technical) coercivity, H_c. Linear B curve is a very important characteristic that enables permanent magnets to be stable during operation. However, common commercial sintered Nd-Fe-B magnets are not good candidate for motor applications since a non-linear B-H curve with a "knee" is shown on its B curve, which suggests the instability when it is surrounded by the magnetic field at elevated temperature. Heavy rare-earth elements such as dysprosium are key components in producing rare-earth permanent magnets (RPMs) which show better temperature stability for motor application. As shown in Figure 1-2 [1], $(Nd_{10}Dy_4)Fe_{80}B_6$ magnets with 4 at% Dy substitution for Nd can retain linear B curves at temperatures up to about 175 ^oC. The disadvantages of this are the reduction in the energy product, $(BH)_{max}$, caused by the antiparallel exchange coupling between Dy and Fe atoms in the $(Nd,Dy)_2Fe_{14}B$ unit cell [6]. Moreover, metal prices in 2014 show that Dy costs ≈ 6 times as much as Nd metal. The work done so far has been focusing on the possibilities of minimum substitution for Nd, more ideal recycling to reduce the heavy

rare-earth content of Nd-Fe-B-type magnets, at the same time reserving their temperature stability. In order to achieve this goal as to coercivity enhancement by Dy-free or Dy-saving techniques, it is vital to understand the coercivity mechanism in Nd-Fe-B sintered magnets in greater detail. The Nd-rich phases and their distributions in the microstructure are critical for the H_{ci} of the magnet, but currently H_{ci} only reaches 20-30% of the theoretical maximum, which is the anisotropy field, H_A. This can be explained by nucleation of reversal magnetic domains caused by locally decreased anisotropy field at grain boundaries due to the existence of in-homogeneities with spatial variations in the anisotropy in real system.

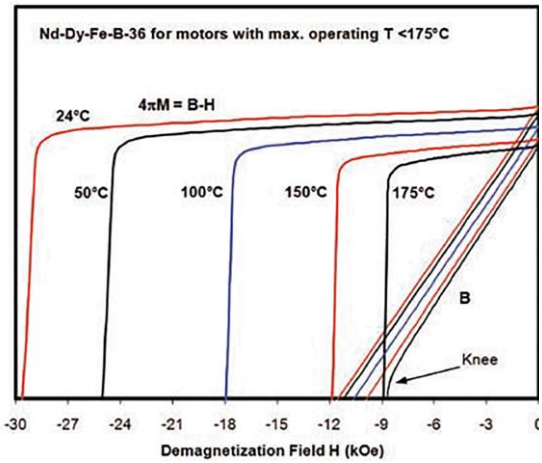

Fig. 1-2 Demagnetization curves in the 2nd quadrant at various temperatures of Nd-Dy-Fe-B used for motors

Although due to the gradually increasing cost of rare earth element, the so called “rare earth crisis” has been driving people to search for new candidate plugging the gap between ferrite and rare-earth magnets [7], $Nd_2Fe_{14}B$, without any doubt, is still the most close-to-ideal high-performance magnet so far till we succeed to find the next-generation materials that can satisfy the constraints of Curie temperature, magnetization, anisotropy and cost. It is definitely worth focusing on further improvement of coercivity of Nd-Fe-B permanent magnets through modifications of the microstructure and understanding the coercivity mechanism via detailed investigations of the grain boundary characteristics of Nd-Fe-B magnets [8].

Combine the continued investigation of coercivity-microstructure relationships with the progress in the areas underlying the understanding of intrinsic properties, such as the anisotropy field of the transition-metal sub lattice and its variation with temperature and composition, accurate determination of mean crystal-field and exchange interactions, development of more realistic models for coercivity, we can be able to get more thorough understanding of the coercivity mechanism as well as get the Nd-Fe-B magnets more optimized microstructure, so as to achieve higher coercivity which will have an substantial impact on generating renewable energy and in raising energy consumption efficiency.

1.2 Nd-Fe-B permanent magnets

The magnetic properties of Nd-Fe-B permanent magnets, especially H_c and B_r known as extrinsic properties, are very sensitive with the microstructure of the magnets. The crystallographic microstructure is closely correlated with the domain structure which in turn determines the magnetization reversal behavior.

1.2.1 $Nd_2Fe_{14}B$ phase

The $Nd_2Fe_{14}B$ phase is the matrix phase of Nd-Fe-B permanent magnets. Since it is the only ferromagnetic phase in the NdFeB-based magnets, all the extrinsic magnetic properties including H_c , B_r, $(BH)_{max}$, and temperature dependence of these properties, are related with the intrinsic properties of the matrix phase. The melting point of $Nd_2Fe_{14}B$ phase is 1185°C, the Curie temperature T_c is 585 K [9].

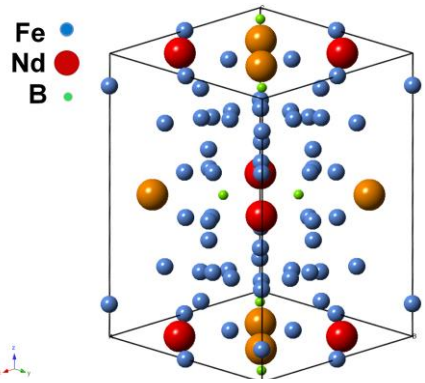

Atom	Site	x	y	z
Fe	4c	0	0.5	0
Fe	4e	0.5	0.5	0.1139
Fe	$8j_1$	0.097	0.097	0.205
Fe	$8j_2$	0.318	0.318	0.247
Fe	$16k_1$	0.224	0.568	0.128
Fe	$16k_2$	0.039	0.359	0.176
Nd	4f	0.266	0.266	0
Nd	4g	0.139	-0.14	0
B	4g	0.368	-0.317	0

Fig. 1-3 Unit cell of $Nd_2Fe_{14}B$ ($P4_2/mnm$ space group) and the atomic site coordinates [10].

The spontaneous magnetization M_s of $Nd_2Fe_{14}B$ phase is 1.61 T which is the highest among $R_2Fe_{14}B$ phases. The crystal structure determined by X-ray and neutron diffraction by Herbst [10] and Shoemaker [11] et al is in a tetragonal structure having $P4_2/mnm$ space group, as shown in Figure 1-3. There are four $Nd_2Fe_{14}B$ units (68 atoms) per unit cell. The lattice constant of $Nd_2Fe_{14}B$ crystal structure, a= 8.8 Å, c= 12.19 Å. The theoretical density of $Nd_2Fe_{14}B$ is calculated to be 7.60 g/cm^3. There are six crystallographically different Fe sites ($8j_1$, $8j_2$, $16k_1$, $16k_2$, 4c and 4e sites), two Nd positions (4f and 4g sites) and one B site (4g). The two Nd sites are separated depending on their different site-specific magnetic moment; 4g site has relatively lager volume than 4f sites.

Three types of exchange interactions are existed in the $R_2M_{14}B$ (M= Fe, Co) crystal: M-M, R-M and R-R. The main contribution of Curie temperature comes from the M-M-type exchange interactions. The spin-orbital exchange coupling between 4f and 3d electrons and the crystal field effect from Nd and Fe sublattices lead to the large anisotropy field of $Nd_2Fe_{14}B$ field. Both Fe and Nd sublattices magnetic moment contribute to the volume magnetic moment. There exists exchange-coupling between 3d spins of the M atoms and 5f spins of the R. For compounds with light R, J= L-S and L < S, the positive coupling of spins leads to a parallel alignment of R and M moments. In the case of compounds with heavy R, J= L + S and L > S, the negative coupling of spins leads to an antiparallel alignment between R and M. The parallel alignment will lead to an enhanced magnetization however antiparallel alignment results in a reduced magnetization.

1.2.2 Nd-rich phase

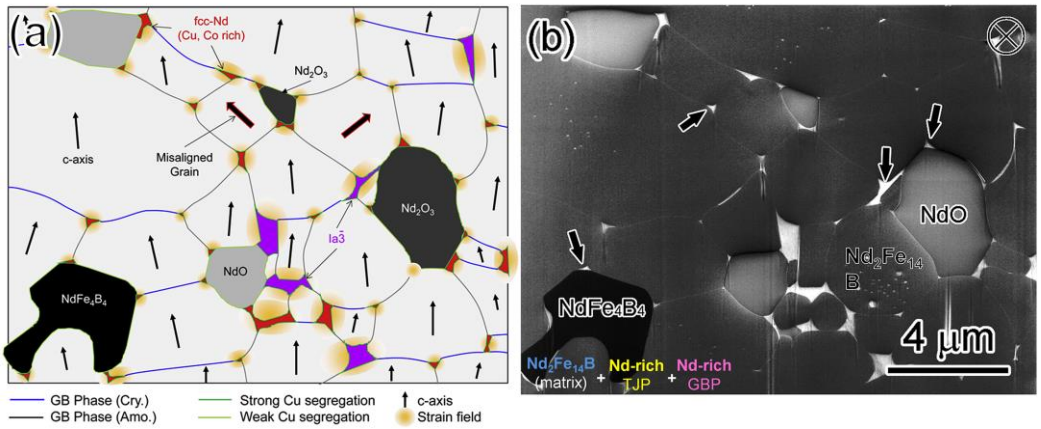

Fig. 1-4 (a) Schematic illustration and (b) IL-SEM image of a typical microstructure of the Nd-Fe-B sintered magnets. In the schematic illustration the assumed misalignment of individual grain is noted by the arrow [13].

The knowledge on Nd-rich phases has been increasing with the help of modern microscopy. In the early time, Fidler et al [12] considered Nd-rich phase as a binary Nd-Fe compounds and classified the different types of Nd-rich phases based on the composition ratio of Nd/Fe as (1) 1.2-1.4/1; (2) 2.0-2.3/1; (3) 3.5-4.4/1; (4) >7/1. Since similar Nd-enriched phase gives more or less the same contrast by the backscattered electron (BSE) SEM images, it's almost impossible to identify them only with BSE imaging technique. Recently the secondary electron (SE) SEM imaging obtained with an in-lens detector which gathers high-angle SE signals enables an unambiguous observation of various types of Nd-rich phases and further makes the transmission electron microscopy (TEM) specimen preparation out of region-of-interest possible. Figure 1-4 shows a typical microstructure of sintered Nd-Fe-B magnets obtained by IL-SEM [13]. Combination of the selected area or nanobeam electron diffraction (SAD and NBED) and 3-dimensional atom probe tomography (3DAPT) brings more accomplishment on the chemistry and structure of the various Nd-rich phases.

(a)

Name	Space group	Prototype	Structure	Lattice Constants
α-Nd	$P6_3/mmc$	La	dhcp	a=3.66 Å c=11.83 Å
NdO_x (x=0.5-2)	$Fm\bar{3}m$	CaF_2	fcc	a=5.5 Å
NdO	$Fm\bar{3}m$	NaCl	fcc	a=5.1 Å
C-Nd_2O_3	$Ia\bar{3}$	Mn_2O_3	bcc (or fcc)	a=11.1 Å
A-Nd_2O_3	$P\bar{3}ml$	La_2O_3	hcp	a=3.83 Å c=6.0 Å
$Nd_{1.1}Fe_4B_4$	$Pccn$	$Nd_5Fe_{18}B_{18}$ oP164	tetragonal	a= 7.117 Å c= 35.07 Å

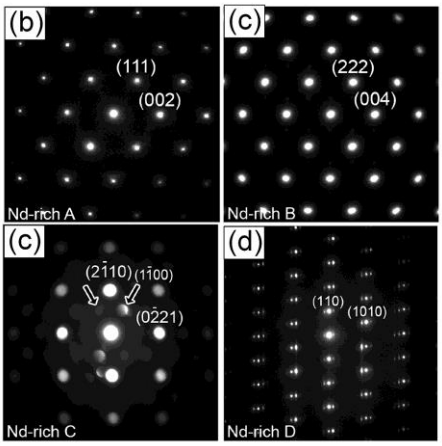

Fig. 1-5 (a) Table of various Nd-rich phases [14-16] and SAD patterns of NdO (b), C-Nd_2O_3 (c), α-Nd (d) and $Nd_{1.1}Fe_4B_4$ (d) phases [13].

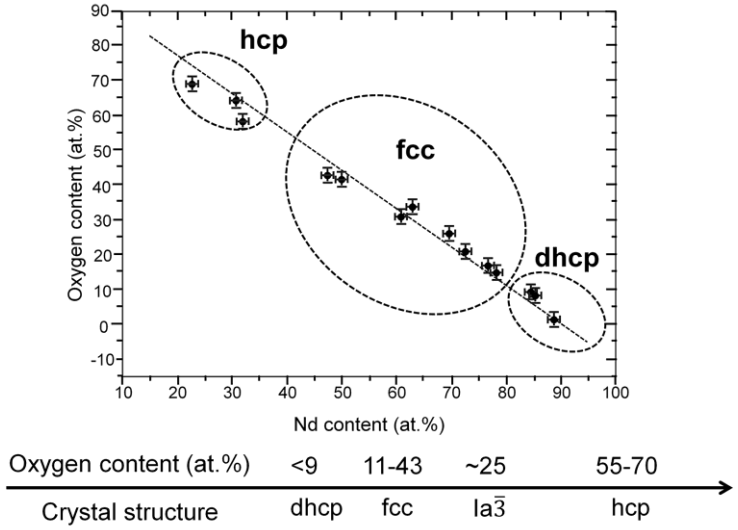

Fig. 1-6 Evolution of crystal structure as a function of oxygen content [17].

In Figure 1-5(a), the table lists out the identified Nd-rich phases including their space group, crystal structure, lattice constant [14]–[16]. The diffraction patterns of NdO, C-Nd_2O_3, α-Nd and $Nd_{1.1}Fe_4B_4$ phases are shown in Figure 1-5(b-d) respectively. The report by W. Mo et al [17] clarified the correlation between the crystal structure of different Nd-rich phases and their oxygen content and pointed out the transformation between different structures, as shown in Figure 1-6. They made the clarification that the crystal structure of the Nd-rich phases is mainly determined by their oxygen content. With the increment of oxygen from <9 at.% to 11-43 at.% to 55-70 at.%, the transformation will happen from dhcp to fcc and to hcp.

There still remain debates on whether the dhcp-typed Nd-rich phase exists in the grain boundaries of Nd-Fe-B magnets, since the minor absorption of oxygen will lead to transformation into the Ia-3 phase, in addition with the difficulty in clarification of the oxygen content.

1.2.3 Nd-rich phases and coercivity

Coercivity, as extrinsic properties also called “the defect property” is closely related to the microstructure of the NdFeB-based magnets. The typical microstructure consists of the $Nd_2Fe_{14}B$ phase and Nd-rich phases located at the triple junctions and the thin inter-grain boundaries. Detailed studies of the microstructures consider that the thin (~2nm) grain boundary phase which envelopes the $Nd_2Fe_{14}B$ grains plays the most role in tuning the coercivity of the Nd-Fe-B sintered magnets[18]–[20]. The thin GB phase was believed for a long time to be nonmagnetic phase [21], [22] which will avoid the avalanche-like propagation of the magnetic reversal process. H. Sepehri-Amin et al [23] observed the Fe concentration of about 63 at.% within the thin grain boundary phase and postulated the ferrimagnetism of the thin GB phase. The modeling work by A. Sakuma et al [24] with the fabrication of the Nd-Fe thin films observed ferromagnetism of the Nd-Fe with similar chemical composition. The ferromagnetism of the ultrathin GB phase was later characterized by a direct magnetization measurement through electron holography [25], X-ray magnetic circular dichroism (XMCD) [26] and spin-polarized SEM [27].

The fact of the anisotropic distribution and the chemistry feature of the GB phases in Nd-Fe-B sintered magnets was later revealed by T. T. Sasaki et al [28]. They carried out the careful characterization of the GB phases formed on different crystal planes of $Nd_2Fe_{14}B$ grains and attributed the difference in the crystal structure as well as the chemical composition of GB phases to the influence from the interfacial energy of the adjacent $Nd_2Fe_{14}B$ grains rather than the misorientation angle between the neighboring grains. The observation (Figure 1-7) established the crystalline GB phase parallel to the (001) plane contains more than 60 at. % of Nd (a) while the thin amorphous GB phase forms along higher-index plane has lower Nd concentration of about 35 at.% (b). As intergranular exchange coupling plays crucial role in limiting the coercivity, they suggest that making the GB parallel to the c-axis is more critical for achieving higher coercivity in grain boundary engineering.

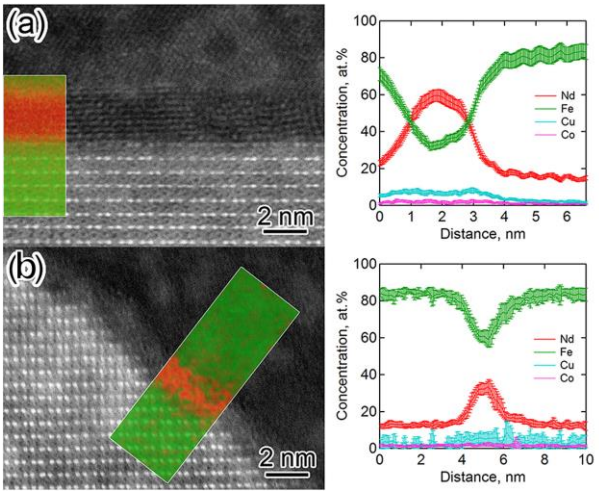

Fig. 1-7 Microstructure anisotropy of Nd-rich GB phases in Nd-Fe-B sintered magnets [28].

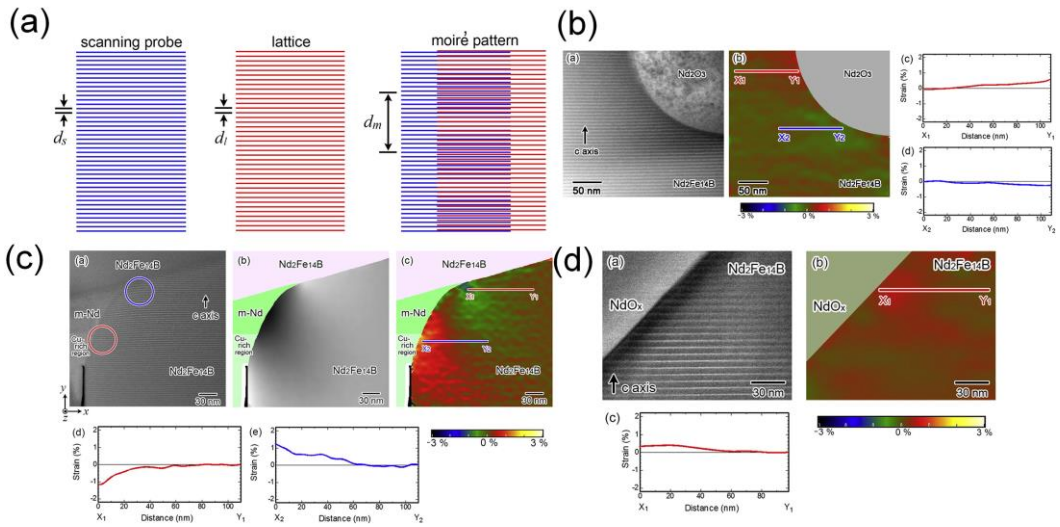

Fig. 1-8 Strain measurement using artificial moiré fringes. (a) Schematic representation of the construction of artificial moiré fringes; Strain measurement from (b) $Nd_2O_3/Nd_2Fe_{14}B$, (c) metallic-Nd/$Nd_2Fe_{14}B$ (including a Cu-rich Nd-rich GB/$Nd_2Fe_{14}B$), (d) $NdO_x/Nd_2Fe_{14}B$ interfaces [31].

Another essential problem concerning the influence of the microstructure of the Nd-rich GB phases on the coercivity is about the interfacial lattice strain from lattice misfit between the GB phase and the $Nd_2Fe_{14}B$ phase. Previous first-principle calculation has made the prediction the strain-induced lattice distortion is dramatic as to reduce the magnetocrystalline anisotropy constant K_u of $Nd_2Fe_{14}B$ phase by orders of magnitude[29], [30]. However, the direct strain measurement recently [31] by analyzing artificial moiré-fringe contrast in the obtained STEM images has been carried out for the $Nd_2Fe_{14}B$ grains in contact with different types of Nd-rich GB phases including metallic dhcp, $Ia\bar{3}$-Nd_2O_3 and the fcc-NdO_x types. The maximum strain was observed at the metallic-Nd/$Nd_2Fe_{14}B$ interface, with the value of ~1.2 %, and 0.4-0.5 % for other two cases, as shown by Figure 1-8. It will be a plausible claim that the small strain existed at the interface between $Nd_2Fe_{14}B$ grains and Nd-rich GB phases is negligible, as a result, the impact on the reduction of K_u of the matrix phase will also not be significant.

1.3 Methods for manufacturing Nd-Fe-B magnets

Most of the current-used high-performance magnets are produced by sintering, bonding and hot-pressing followed with hot-deformation processes. The common themes for the optimization of manufacturing process are aiming for higher maximum energy product, improved thermal stability, flexible near-net shape machining and of course, higher coercivity with decent remanent magnetization.

1.3.1 Sintering

Figure 1-9 (a) is a calculated transverse section of the Nd-Fe-B ternary phase diagram with Fe/B ration of 80/6, where the sample with 14 at.% of Nd is indicated by the red dashed line [32]. It can be seen that under equilibrium solidification, the primary γ-Fe phase precipitates first from the melt. At the temperature near 1156°C, $Nd_2Fe_{14}B$ phase forms through the peritectic reaction. With temperature decreasing close to 1066 °C, $Nd_{1.1}Fe_4B_4$ (B-rich) phase will form. Further decrease the temperature till 655°C, the ternary eutectic transition to Nd-rich phase, $Nd_2Fe_{14}B$ phase and $Nd_{1.1}Fe_4B_4$ phase will come.

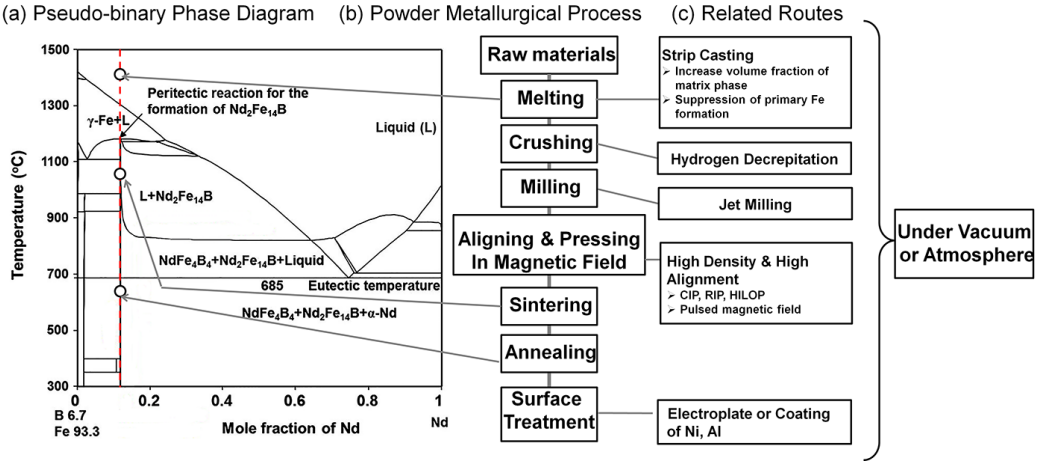

Fig.1-9 (a) Calculated pseudo-binary phase diagram of Nd-Fe-B at Fe/B ratio of 14 [32]; (b) flow chart showing sintering process and (c) the corresponding manufacturing routes.

The melting, sintering and heat-treatments in the metallurgical processes should be conducted within specific temperature range derived from the phase diagram (Fig. 1-9(b)). The temperature and time of the sintering should be determined by the composition as well as the specific powdering method. As an example, for the $Nd_{14.5}Fe_{79}B_{6.5}$ magnet, when sintering at 1313 K the sample is still porous because of 93 % relative density. But, the sample sintered at 1343 K has 96 % relative density and high ${}_iH_c$ and shows denser and finer microstructure [33].

The optimization starts with the composition design for higher $Nd_2Fe_{14}B$ phase proportions. Selecting the proper starting composition is critical to achieve the best overall magnetic properties. Closer to the stoichiometric composition of $Nd_2Fe_{14}B$ phase is beneficial to increase the volume fraction of the matrix phase, so as higher $(BH)_{max}$. The remanent magnetization of the Nd-Fe-B sintered magnets is shown by Kaneko et al [33]as the equation

$$\mu_0 M_r \propto \mu_0 M_s \beta \{\left(\frac{\rho}{\rho_0}\right)(1-\alpha)\}^{2/3} f \quad (1)$$

where M_s is the saturation magnetization of the $Nd_2Fe_{14}B$ phase, β refers to the temperature coefficient of M_s, ρ/ρ_0 is the ratio of real density over the density of the single crystal, α stands for the volume fraction of the non-magnetic phase in the magnets and f is the easy-axis alignment degree of $Nd_2Fe_{14}B$ grains.

However, excessive precipitation of Fe during equilibrium casting is detrimental to the coercivity. The Nd-rich phase, however, is essential for functioning as the lubricant in liquid-phase sintering which is important to get high density magnets. It will surround the $Nd_2Fe_{14}B$ phase during sintering, and appears to have strong influence on the coercivity value of the magnets [34]. The strip-casting technique [35] provides an over-quenched state and limits the amount of Fe precipitates, which in turn ensures more uniform formation of Nd-rich GB phases.

Further refinements have focused on the alignment and pressing of the milled powder. Conventional alignment of the green compact with parallel or perpendicular (with the direction of applied magnetic field) pressing known as Cold Isostatic Press (CIP) gives the alignment degree of 86-93 %. The Rubber isostatic pressing (RIP) developed by M. Sagawa et al [36] can produce even higher degree of alignment till ~98 %. The Hitachi low oxygen process (HILOP) [37] covers the NdFeB fine powders with organic oil which will protect the powder from oxidization and serves as lubricant during the pressing. This process enables the fabrication of fine-sized NdFeB particles through lowering the oxygen level from 5800 ppm to 1600 ppm since the Nd-rich phase is highly reactive with oxygen which cannot be fully avoided during processing of the magnets.

The coercivity of Nd-Fe-B magnets could be further increased by a post-sintering thermal treatment, which includes several steps between 900 and 600 ^oC with different cooling rates. Sagawa et al [38] attributed the enhancement of coercivity to the removal of damaged particle surface by the action of a grain boundary liquid phase, forming clearer, more continuous grain boundary phase. H. Sepehri-Amin et al also attributed the coercivity enhancement by the post-sinter annealing to the formation of continuous grain boundary by the eutectic reaction from the liquid into Nd-Cu and Nd-rich phase in the sintered NdFeB magnets containing small amount of Cu and Al [23].

1.3.2 Bonding

Both isotropic and anisotropic magnets can be fabricated through bonded routes. For anisotropic-bonded magnets, they start with extremely fine grain size rapid solidified or HDDR powder [39] [40] and followed by grinding and alignment in a magnetic field. By a HDDR process, the coarse-grained structure in starting ingot is transformed into the one composed of fine $Nd_2Fe_{14}B$ grains of about 0.3 μm diameter. B_r and $(BH)_{max}$ are directly related with the amount of the binder used, which is typically 2wt.% in compression molded magnets and 8-15 wt.% in injection molded magnets.

Bonded magnets can be categorized into four types [41] by different fabrication techniques: (a) calendaring type using a flexible binder, (b) extrusion type using a thermoplastic resin, (c) injection type also using a thermoplastic resin, and (d) compression type using thermoset resin. With appropriate tool design, both compression and injection molding techniques can produce magnets with near net shape. Usually, the combination of an epoxy binder and compression molding method enables to obtain the highest volumetric fraction of magnetic powders [42], while a wider variety of shapes and a greater spectrum of applications magnets can be produced using injection molding technique .

A change in remanence was reported as a function of volume fraction of hard magnetic phase and was attributed to changes in magnetic exchange-coupling interactions between particles [43]. The dipolar interactions increase rapidly with volume fraction at low-volume fractions and slowly at high-volume fractions. The internal shear loss, originated from the static magnetic coupling can be reduced by isolation magnetic powders shearing with each other through the dispersion in the polymer matrix. The typical bonded magnets produced by this optimization is MQP-B (isotropic melt-spun) powder which has a B_r ~ 0.9 T and $(BH)_{max}$ ~16.3 MGOe. Anisotropic bonded magnets will further suffer from a reduction of B_r during the alignment of the isotropic powders in magnetic field. The alignment of anisotropic nano-size grains is the challenge issue since the alignment requires very large fields close to 2.4 T to achieve high alignment degree. With the usage of soft metal binder, such as Al, Zr, Sn, Cu in the 0.25 %, the densities obtained has been assessed for proper machinability and mechanical strength, under the premise of ideal remanence value.

1.3.3 Hot-deformed magnets

An alternative method for producing high-energy Nd-Fe-B magnets is the hot-deformation. Hot-deformed magnets were manufactured by hot-pressing the isotropic Nd-Fe-B ribbons or HDDR powers to a full dense isotropic precursors [44], and then deforming or upsetting the sample to achieve a specific amount of plastic deformation. This method was first prepared as a feasible process for remanence enhancement of magnets produced from melt-spun Nd-Fe-B ribbons by Lee et al [45]. The microstructure of hot-deformed magnets has been described as composed with platelet-shaped grains (50-100 nm thick and 200-600 nm in diameter) where the short dimension corresponds to the c-axis of the tetragonal $Nd_2Fe_{14}B$ crystalline phase.

With the quenching rates of the melt-spinning process, the liquid intergranular phase can solidify in the non-crystalline form. The difficulties associated with the crystallization of thin films of liquid [46] (due to difficulties of nucleating crystallites, volume change effects with crystallization as well as the two-

dimensional diffusion operative for phase separation at the eutectic point [47]) facilitate the formation of this two-phase microstructure in the melt-spun ribbons.

Proper quenching rate is necessary to get optimal coercivity value by affecting effective pinning sites formed at the grain boundary [48] [49]. The absence of any barriers for magnetic reversal process of over-quenched ribbons accounts for the absence of coercivity in these materials.

The key for the hot workability is the presence of Nd-rich grain boundary phase which is in liquid state at the deformation temperature [50]. The hot-deformation mechanism is suggested to be a solution-precipitation creep model [51] [52] [53]. This densification and deformation are possible in the temperature range from 700 ^{o}C to 750 ^{o}C because a liquid grain boundary phase is present above 670 ^{o}C [54]. Since there is no evidence of dislocations in the $Nd_2Fe_{14}B$ phase, the conventional slip mechanisms of deformation is unlikely to be operative. It is proposed that the texture induction is due to the anisotropic grain boundary sliding and preferential oriented grain growth under stress which leads to platelet shaped grains [55] [56] [57].This could be due to the anisotropy of crystal growth of the tetragonal $Nd_2Fe_{14}B$ phase [58] or the anisotropy of its elastic properties.

W. Grünberger et al [59] pointed out the hot-deformation effect on texturing is related to the microstructure-dependent quality (fine-grained microstructure), stress strain rate, effective activation energy of the process, and hot-deformation temperature. The optimization of hot-deformation condition includes proper height reduction degree, stress loading rate, and deformation temperature [60]. The low forces (pressure loading rate) required for deformation process and the absence of cracks reveal a good hot workability [61] [62]and a high degree of anisotropy [63]of the hot-deformed magnets.

The low levels of additives are particularly useful in improving the coercivity. For example, 1 at% Ga in hot-deformed Nd-Fe-B magnets increase the coercivity by 100% compared to an additive free magnet [63].

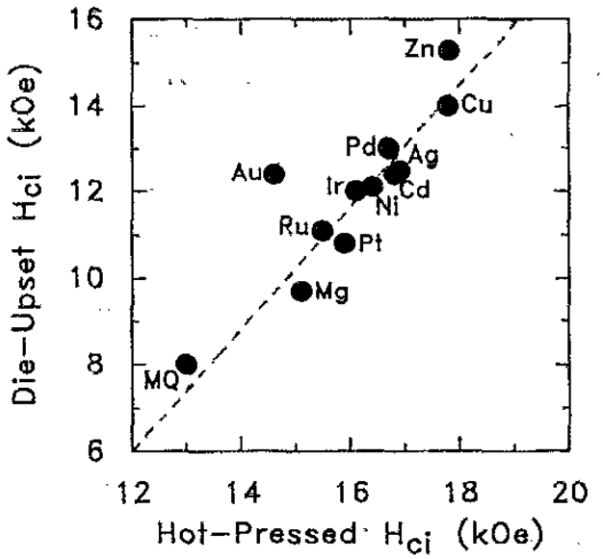

Fig. 1-10 Coercivity (H_{ci}) for die-upset versus hot-pressed magnets containing the same additive. The additive-free magnet is denoted by MQ. The broken line is a guide to the eye, indicating the general relationship between the coercivity of a die-upset magnet and its hot precursor [64].

Fuerst and Brewer [64] listed out the effect of various additives in hot-deformation process for improving the coercivity, as shown in Figure 1-10. In the figure, the addition percent is 0.5 wt.%, except Mg, where the concentration was 0.3 wt.%. In small quantities, all the additives are able to increase the coercivity. The effect of the low melting additives such as Al, Ga, Zn, Ga, et al on the enhancement of coercivity of hot-deformed Nd-Fe-B magnets are explained as the formation of lower melting-point Nd-rich intergranular phases which induces better wettability with the matrix phase, better deformability during hot-deformation [65].

1.4 Coercivity of Nd-Fe-B permanent magnets

1.4.1 Nucleation model versus pinning model

The magnetic state of a magnet is determined by the domain structures formed to minimize the total magnetic energy, which can be expressed by the equation of

$$\varepsilon_{tot} = \varepsilon_{ex} + \varepsilon_a + \varepsilon_d + \varepsilon_Z + \varepsilon_{stress} + \varepsilon_{ms} \quad (2)$$

The energy items refer to exchange energy, anisotropy energy, dipolar energy, Zeeman energy, strain energy and magnetostriction energy, respectively. Taking exchange stiffness A as 8 pJ/m and K_1 as 4900 kJ/m^3, the single domain particle size R_{SD} of $Nd_2Fe_{14}B$ can be derived to be 260 nm with the equation$R_{SD} = \frac{9}{\mu_0 M_s^2}\sqrt{AK_1}$. The coercivity is strongly related to the domains structure of the magnets so as to the microstructure of the magnets. Ferromagnets can reverse its direction of magnetization either continuously, through coherent or incoherent rotation processes, or discontinuously, through domain processes. Coercivity will be determined by the easiest of these processes. To achieve high coercivity, it is therefore essential to impede magnetization rotation with magnetic anisotropy, usually crystal or shape anisotropy, and to impede either nucleation or the growth of reverse domains [66].

Three related parameters of relevance to the coercivity issue are the domain wall width δ, the domain wall energy density σ_w and the critical single-domain particle diameter D_c; for Nd-Fe-B at room temperature δ ~50 Å, σ_w ~ 30 mJ/m^2 and D_c ~260 nm. D_c represents the diameter of an isolated spherical domain below which formation of a domain wall is energetically unfavorable and above which a multi-domain configuration is stable. Its value provides a qualitative distinction between sintered Nd-Fe-B magnets, whose average grain size D_g ~10 μm is much larger than D_c, and a hot-deformed magnets, for which D_g ~200 nm ≤ D_c. This contrast suggests that different coercivity mechanisms may be necessary when it comes to these two magnets.

Magnetocrystalline anisotropy is the most effective fields of impeding magnetization reversal by rotation processes. It provides an energy barrier resisting departure from the easy (low-energy) direction of magnetization that impedes both coherent and incoherent rotation processes, regardless of volume fraction and particle size.

The assumption of nucleation models is that at large fields all domain walls are removed. A single-phase uniaxial magnet with anisotropy K ($K \geq 2\pi M_s^2$) will thus behave as a large single domain particle. The

magnetization of this particle can be reversed at $H_c = H_K = 2K/M_s$. Calculating with the values of *K* and M_s for $Nd_2Fe_{14}B$ phase H_c is predicted to be around 7 T. This value is much larger than the experimental values of 1~1.5 T. To explain this discrepancy, it was assumed that nucleation takes place at secondary phases or chemical and physical defects with lower *K* and (or) at grains with large demagnetizing factors *N* (grains with sharp corners) where the nucleation fields H_N are smaller with

$$H_N = H_K - NM_s \tag{3}$$

In some cases, residual reverse domains may be present because of incomplete saturation. Small reverse domains may resist expansion as a result of the surface tension of domain walls, and their final propagation on reaching a critical size can be viewed as the nucleation event.

In Kromüller's work, H_{ci} is written as

$$H_{ci} = \frac{2K_1}{M_s}\alpha_K\alpha_\Psi - N_{eff}(4\pi M_s) \tag{4}$$

where K_1 is the first anisotropy constant, $\alpha_K$stand for inhomogeneity of the magnetocrystalline anisotropy in grain boundary regions whose anisotropy is lower than that of the matrix phase and in which reverse domain nucleation is easier to happen, α_Ψ accounts for misaligned grains and N_{eff} is an average effective local demagnetization factor.

The Kromüller equation considers a planar inhomogeneity of thickness r_0 and compares predictions for both pinning and nucleation descriptions, for which different forms of α_K and α_Ψ will be used for the prediction. The pinning approximation is found to yield contradictory results, while in the nucleation case plots H_{ci}/M_s vs. $(2K_1/M_s^2)\alpha_K^{nuc}\alpha_\psi^{nuc}(\min)$, where $\alpha_\psi^{nuc}(\min)$ is chosen to give a lower limit for H_{ci}, can be fit with a spectrum of r_0 values and are linear over an extended temperature range. The departures from linearity for $T \geq 450$ K indicate that domain wall pinning governs the coercivity in that high temperature range.

To simplify the equation, we define $c = \alpha_K\alpha_\Psi$ as the structural factor. Then we have the equation

$$H_{ci} = H_a c - N_{eff}(4\pi M_s). \tag{5}$$

With *c* =1, this equation specifies the lower bound for the coercivity of an isolated, single domain particle, which represents empirical extensions of the non-interacting single particle rotation to bulk magnets.

According to this equation, we can get several hints relative to increase the coercivity value of Nd-Fe-B magnets. First, small $Nd_2Fe_{14}B$ grains are necessary for minimizing the density and size of nucleating defects and by subdivision into fine regions in which the probability of such defects is small, and the grains should be smooth to limit the vital effect of local demagnetizing (stray) fields at sharp edges. Second, a thin, smooth and defect-free grain boundary layer will works to magnetically isolate the $Nd_2Fe_{14}B$ grains and provides a barrier to demagnetization to neighboring grains. Finally, it is helpful to minimize the amount of secondary phases such as B-rich regions and oxides, as well as pores, which can also act as nucleation sites.

Research on the origin of coercivity in melt-spun systems, especially hot-deformed magnets, is less extensive and less consistent than that for sintered magnets. Hadjipanayis et al [67] showed evidence of domain wall pinning at grain boundaries in optimum ribbons by Lorentz microscopy investigations.

However, Durst and Kronmüller [68] pointed out that such observations, carried out for thin samples in a demagnetized state, may not provide definite evidence for a pinning mechanism. Pinkerton and Fuerst [69] later checked the strong pinning ($r_0 < \delta_B$, i.e the pinning sites which have the different magnetic property with $Nd_2Fe_{14}B$ phase are in smaller or comparable with that of the domain wall width) model by applying on hot-deformed magnets by measuring the temperature dependence of coercivity, concluding that the model proposed by Gaunt [70], describing H_{ci}(T) by

$$\left(\frac{H_{ci}}{H_0}\right)^{\frac{1}{2}} = 1 - \left(\frac{75kT}{4bf}\right)^{\frac{2}{3}}, \tag{6}$$

where H_0 is the critical field in the absence of thermal activation, $4b$ is the range of interaction between domain wall and pin, and f is the maximum restoring force per pin, is in good agreement with the coercivity H_{ci} (T) between temperature range 200 K-585 K. Pinkerton found that ${}_iH_c$ (T) can be well described by equation (3) with c=0.25 and N_{eff} = 0.26. This value is in consistent with the value predicted by Kronmüller [71] for which pinning model is valid for temperature dependence of ${}_iH_c$, the maximum value of c parameter is 0.3 obtained by the test of pinning mechanisms.

The initial magnetization curve of hot-deformed magnets exhibits much lower initial susceptibility than that of sintered magnets. Furthermore, the coercivity develops more slowly with applied field, attaining its maximum, high-field value ${}_iH_c = {}_iH_c(\infty)$ only for $H > {}_iH_c(\infty)$. These characteristics are suggesting the disparate behavior of the magnetic viscosity for melt-spun magnets and sintered magnets [72]. Pinkerton and Van Wingerden [73] explain the low-field behavior to domain propagation, with subsequent pinning in intergranular regions making further wall movement in larger magnetizing fields progressively more difficult.

According to the pinning theory of Bloch walls [74] [75], the pinning mechanism that is active in the magnetization process of hot-deformed magnets mainly refers to the strong pinning model, which is provided by the pinning sites in the comparable dimensions as the domain wall width, such as the planar defects of grain boundary phase, it will completely cover the reversed domains, thus making the magnetization reversal process hard to propagate. The randomly distributed defects can also become pinning sites when they work statistically, which were called as weak pinning sites.

In general, the pinning force provided by the grain boundary phase can be expressed as the equation [76]

$$H_c \propto \frac{KW}{\delta_D}\left(\frac{\Delta A}{A} + \frac{\Delta K}{K}\right), \tag{7}$$

where K and K_0 represents the magnetocrystalline anisotropy of $Nd_2Fe_{14}B$ and grain boundary phase, respectively; A, A_D refer to the exchange energy of $Nd_2Fe_{14}B$ and grain boundary phase; W indicates grain boundary thickness and δ_D is the domain wall width.

1.4.2 Coercivity and grain size of $Nd_2Fe_{14}B$ phase

One well-known method to increase the coercivity of Nd-Fe-B permanent magnets is to refine the grain size of the $Nd_2Fe_{14}B$ phase. As has been stated as the Kromüller's equation before, the discrepancy of actual coercivity value from the anticipated theoretical value comes from the reduced local magnetocrystalline anisotropy originated from the microstructural defects [30], described by the structure factor, c, in the

equation at the same time, the snow-slide patterned propagation of magnetization reversal due to the intergranular exchange coupling that is caused by the ferromagnetic GB phase [21] [23].

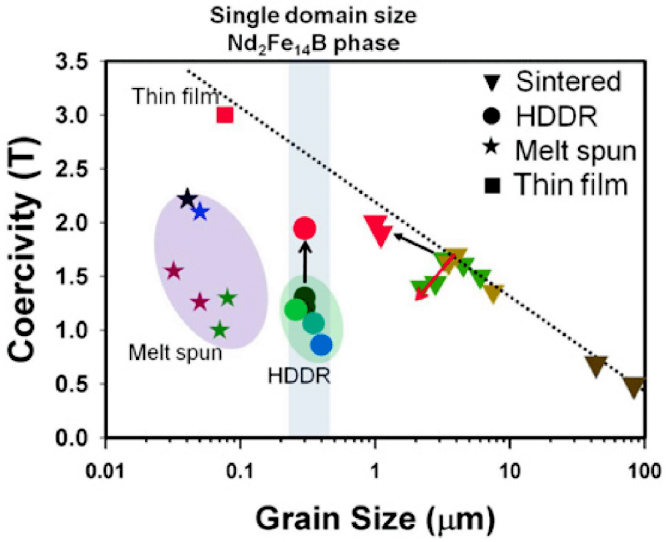

Fig. 1-11 Empirical plot of coercivity in the relationship with the mean grain size of NdFeB magnets [77].

Fig. 1-11 [77] shows the coercivity dependence on the gain size of $Nd_2Fe_{14}B$ phase fabricated through various manufacturing routes. The dotted line in the figure is predicted by Ramesh and his co-workers. Assuming that magnetization reversal occurs by the nucleation of reverse domains from the grain boundaries of magnetically isolated grains, they derived that the coercivity increases as the grain size decreases following $1/lnD^n$ relationship [78] [79]. However, when the grain size is further reduced to around 3 μm, coercivity begins to deviate to a much lower value. Li et al [80] showed that this deduction of coercivity below this critical grain size originated from the oxidation of Nd-rich phases, which mainly dominated by neodymium oxides while a certain fraction of Nd metallic present with a larger grain size. Normal grain size dependence was achieved by the suppression of the oxidation of the Nd-rich phase by a press-less sintering process. The fine-grained magnet has a two-step initial magnetization curve. The initial high susceptibility is explained by the domain wall propagation within grains. Since the grain size the same order of dimension as that of the dingle domain particles, some of the grains don't contain magnetic domains. Then, the domain wall is pinned at the grain boundaries, the domain wall propagation becomes more and more difficult, and the magnetic field higher than the pinning force is required to reverse the single-domain particle.

By the conventional metallurgy method of manufacturing, further grain size refinement cannot be possible. However, through hot-deformation route, there is still room to refine the grain size, since the ribbons contain multi-particles which is much smaller than the single-domain particles, at the same time, not exposed to the oxygen. This makes it possible to produce the magnets composed with the $Nd_2Fe_{14}B$ grain size comparable with the single domain size (~250 nm).

The explanation of the grain size refinement effect on coercivity enhancement can be the decrement of density of defects on the $Nd_2Fe_{14}B$ grain surface due to the reduction of grain size. It can also be attributed to

the reduction of the stray field that is generated from surface charge that may come from the surface that is not parallel to the easy axis or non-uniform magnetization [81].

1.4.3 Coercivity and trace element addition

Coercivity, as extrinsic property, can be manipulated via both intrinsic structure modification, such as the anisotropic field and the grain size of $Nd_2Fe_{14}B$ phase, and at the same time, can be improved through modifications made to the grain boundary phase and the interface between the $Nd_2Fe_{14}B$ phase and the grain boundary phase.

The microstructure modifications have been made through trace element addition. A review has been made by J. F. Herbst [9] on the use of additives. In general, additives can be classified into different types. Type1 additives are low-melting metals like Al, Ga, Cu, Sn or Zn, which form new intergranular phases with an improved wettability behavior during liquid-phase sintering. Type 2 additives are high-melting refractory metals (Nb, V, Mo and Ti), which form precipitates and high-melting borides. These two types of additives mainly influence the microstructure, e.g. they lead to a better magnetic decoupling of the grains and therefore increase the coercivity. Type 3 additives substitute the magnetic elements in the hard magnetic phase, e.g. Co, Dy and Pr. These elements change the intrinsic material parameters J_s, K_u and the Curie temperature T_c. In most cases, the use of these type 3 additives has the disadvantage of a reduced remanence J_r. Co has a lower magnetic moment than Fe and the heavy rare earth elements (Dy) couple antiparallel to the Fe atoms, thus reducing the magnetic moment per formula unit.

In this review, general description of different additives functioning on coercivity improvement has been made. Ga can partially dissolve in the hard magnetic phase, $Nd_2Fe_{14}B$ phase, and form a two-phase intergranular region consisting of Nd_3Ga and platelet-like precipitates of composition $Nd_5(Ga,Fe)_3$ [82]. Similar with Ga, Al introducing to the grain boundary can also improve the wettability between Nd_2Fe_{14} and the surrounding liquid during sintering and could afford more complete separation of $Nd_2Fe_{14}B$ grains, enhancing H_{ci} by reducing exchange interactions among them. Aside from the enrichment of Al in the intergranular phase, Al substitution of Fe in the matrix phase was also reported. This substitution behavior was believed to change the intrinsic magnetic properties, as has been stated in the part of 1-3-3. It has a peak in the changing of anisotropic field of $Nd_2Fe_{14}B$ phase till to around 0.8 at%, and will decrease the Curie temperature as well as the magnetization of the magnet.

Type 2 additives addition such as Nb will form precipitates within the hard-magnetic grains and may be responsible for improving H_{ci} by serving as domain-wall pinning sites. Besides, these precipitates are also considered to be able to induce grain refinement of the sintered magnets.

Since Type 3 additives would cause changes to the room temperature magnetic properties as well as the thermal stability. Co substitution increases T_c and decreases temperature coefficient of coercivity. Aside from the extension of the useful operating temperature range, Co substitution introduces microstructural changes, formation of the soft-magnetic Laves phase $Nd(Fe,Co)_2$ in the grain boundary is postulated to be accompanied by loss of coercivity. Partial replacement of Nd by Dy substantially enhances H_{ci} and reduces

temperature coefficient of remanence, chiefly by increasing the anisotropy field of $Nd_2Fe_{14}B$. Combined Dy and Co substitution is effective in raising T_c and H_{ci} and in decreasing coercivity temperature coefficient. Using low-field arc thermomagnetic analysis, Strnat et al found evidence for a thin ferromagnetic grain-boundary layer having T_c 50-80 K lower than that of the bulk in a (Nd,Dy)-(Fe,Co)-B magnet; pinning of residual domain walls in that layer was suggested as the mechanism for coercivity.

In fabrication of real Nd-Fe-B magnets, it is common to combine all the three types of additives to achieve a high-performance permanent magnet, which means three principle requirements of (i) Curie temperature T_c significantly exceeding any magnet operating temperature, (ii) high spontaneous magnetization M_s, (iii) a large magnetocrystalline anisotropy Ha that dictates the intrinsic coercivity value.

1.4.4 Heavy rare-earth element grain boundary diffusion process (HRE-GBDP)

In the interior permanent magnet synchronous motors design, the permanent magnets are subjected to strong demagnetizing fields and moderately high temperature. The poor thermal stability of sintered Nd-Fe-B magnets significantly limits their applications. The most efficient technique to develop high-performance Nd-Fe-B permanent magnets is the utilization of heavy rare-earth elements (HREs), such as Dy, Tb, et al. Before the year of 2011, the challenge to apply HREs in the manufacturing of Nd-Fe-B permanent magnets was unsteady price due to limited supply options and the consideration of cost-to-performance. Figure 1-12 [83] depicts the ratio of each RE element accounted in the whole RE reserve in a typical ore body. For reference, the total rare earth elements natural reserve is around 155 ppm while the element of silicon existed in the earth ore is 277, 100 ppm. Before 2011, the restriction in applying HREs in the manufacturing of Nd-Fe-B permanent magnets is mainly unstable global price and high-risk supply chain, with the improvement in security of supply, visibility into pricing and long-term supply agreements, the approaches with application of less Dy through grain boundary diffusion (GBD) techniques come into play in producing industrial-graded Nd-Fe-B permanent magnet products.

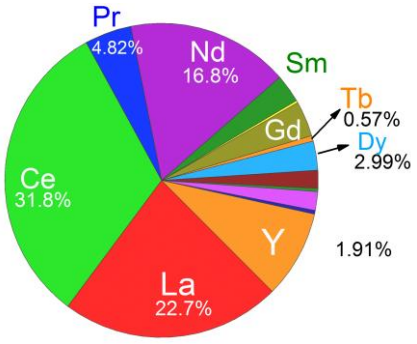

Fig. 1-12 Natural reserve of each rare-earth element. The pie figure shows the ratio of each rare-earth element over the total rare earth elements.

However, the efforts to reduce or eliminate use of Dy by localizing Dy only at the periphery of $Nd_2Fe_{14}B$ grains are not only because of the price and supply problems, but are also based on the consideration of avoiding the degradation of M_s as a result of Dy substitution for Nd of $Nd_2Fe_{14}B$ phase. There is an exchange coupling between 3d spins of the M atoms and 5f spins of the R. For compounds with light R, J= L-S and L < S, the positive coupling of spins leads to a parallel alignment of R and M moments. In the case of compounds with heavy R, J= L + S and L > S, the negative coupling of spins leads to an antiparallel alignment between R and M. The parallel alignment will

lead to an enhanced magnetization however antiparallel alignment results in a reduced magnetization, as has been illustrated in Figure 1-13 [6].

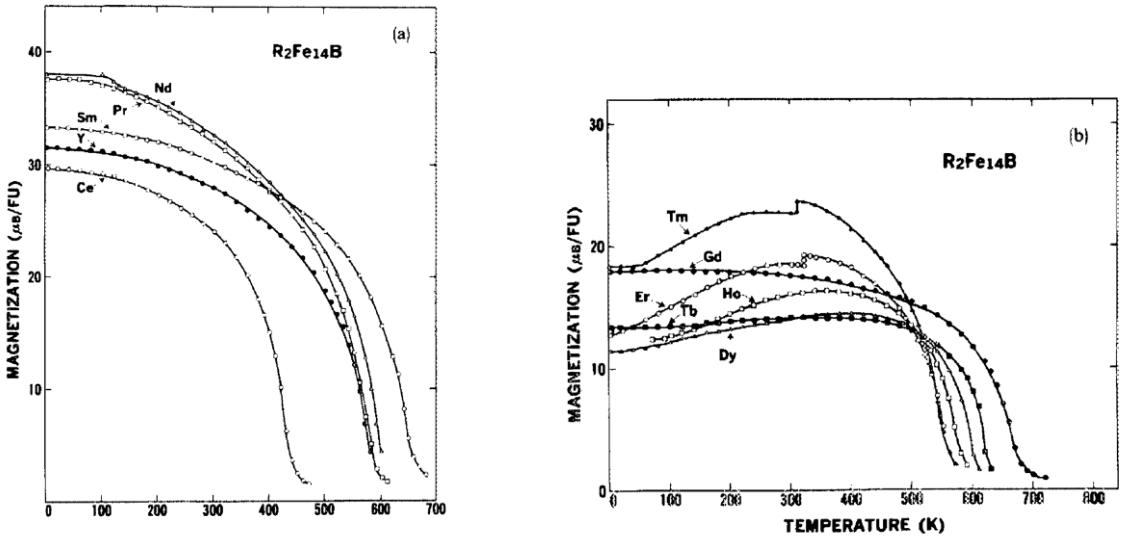

Fig. 1-13 Temperature dependence of $R_2Fe_{14}B$ compounds (R= light REs (a) and heavy REs (b)) [6].

There are three typical GBD techniques reported by the top Japanese sintered magnets makers. The first technique is to blend Dy_2O_3 powder with NdFeB powder followed by heat-treatment to introduce Dy-rich layer on the surface of $Nd_2Fe_{14}B$ grains, known as HAL process by TDK. This process saves 20-50 % Dy compared with tradition sintering process. The second technique is to heat the magnets with coating Dy_2O_3 or DyF_3 slurries to concentrate Dy at the grain boundaries, reported by Shinetsu, realizing savings in Dy by around 60 % from original two-alloy method. The third method is the Dy-vapor diffusion process developed by Hitachi metals in 2014.

The research has been focusing on clarifying the mechanism of HRE-rich shell structure formation. The recent studies pointed out the asymmetric nature of the Dy-rich shell along GBs which cannot be explained through the simple solid diffusion model [32]. Based on the phase diagram and EBSD orientation maps, they think the faceted shell structure is a result of coherent grow (or solidification) from the $Nd_2Fe_{14}B$ cores during cooling of Dy-enriched liquid and suggest further increase of Dy content in the shell structure could not be realized by the GBD process, in their work, Dy-vapor diffusion process. However, report by T.-H. Kim et al [84] holds different view of points. They claim that the formation of Dy-rich shell is due to the diffusion from grain boundaries to the $Nd_2Fe_{14}B$ grains and further enrichment of Dy in GBs would be capable to further increase the Dy content in the shells.

1.4.5 Temperature dependence of coercivity

The Nd-Fe-B permanent magnets are subjected to the high temperature during the functioning in the traction motors; the typical working temperature is above 150 ^oC. The magnets will suffer from a thermal degradation in coercivity as well as remanent magnetization. Although the thermal stability of the permanent

magnets is mainly characterized by *T*c (the transition point from ferromagnetic to ferromagnetic), manipulation of the microstructure is also critical to obtaining a good thermal stability, especially a small temperature dependence coefficient of coercivity usually denoted as β,

$$\beta = \frac{H_c\,(T_1) - H_c(T_0)}{H_c(T_0)(T_1 - T_0).} \tag{8}$$

The unit is %/$_o$C. It's used as a measure of the irreversible loss of coercivity over the temperature range of T_0-T_1.

The temperature-dependent coercivity can be simulated with the phenomenological micromagnetic equation as

$$H_c(T) = \alpha H_A(T) - N_{eff} M_s(T). \tag{9}$$

(a)

Magnets	α	N_{eff}	Ref.
Sintered	0.6-0.7	1.4-1.8	68, 71
Melt-spun	0.6-0.7	0.8-1.0	82, 85, 86
Hot-deformed	0.8-1.0	0.8-1.4	87
Thin film	0.4	0.1-0.4	88

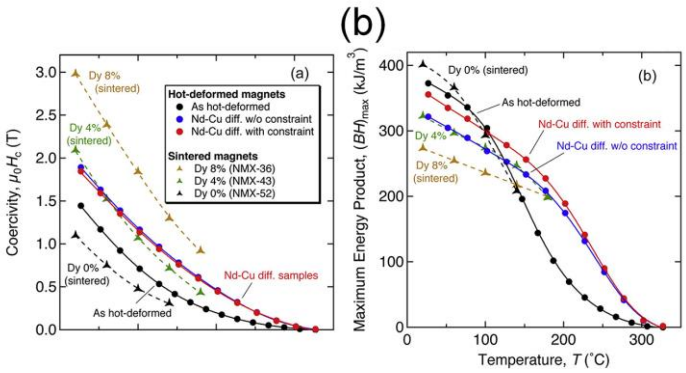

Fig. 1-14 (a) Micromagnetic parameters of permanent magnets; (b) Comparison of thermal stability as for coercivity and energy products of sintered magnets and hot-deformed magnets.

This is based on the nucleation model of coercivity assuming the expansion of reversed magnetic domains in a uniform system. The typical microstructure factors α and the effective demagnetizing factor N_{eff} are listed as shown in Figure 1-14 (a) ([68], [71], [82], [85]–[88]). The micromagnetic simulation by H. Sepehri-Amin et al [81] has shown that the grain size refinement of $Nd_2Fe_{14}B$ grains will lead to a better thermal stability of the magnets due to the smaller localized stray field. Previous reports [89] consider the smaller N_{eff} value of hot-deformed magnets is due to the modification of the geometry of the $Nd_2Fe_{14}B$ grains. Figure 1-14 (b) shows the comparison of temperature dependence of coercivity between hot-deformed and sintered Nd-Fe-B magnets. Hot-deformed Nd-Fe-B magnets exhibit much better thermal stability compared with that of sintered Nd-Fe-B magnets.

1.5 Summary and outlook

In this chapter, remarks on different aspects of Nd-Fe-B permanent magnets have been made. We started with the intrinsic properties and physics of the $Nd_2Fe_{14}B$ compounds and then discussed the two typical coercivity mechanisms in modeling practical coercivity. Later on, practical technological aspects including different manufacturing methods of Nd-Fe-B magnets and microstructure modifications by grain size refinement and trace element addition were described.

We have understood that technical magnetic characteristic coercivity, H_{ci}, as extrinsic property, depends crucially on the microstructure of the material. The microstructure involves the size, shape, and orientation of the crystallites of the compound and also the nature and distribution of secondary phases, i.e. grain boundary phase, which usually control domain-wall formation and motion and hence determine the magnetization and demagnetization behavior. (In the opposite extreme of a single crystal, reversed domains can nucleate and grow very easily at room temperature; H_{ci} and the other technical properties are negligible, since there is no impediment to domain wall motion.)

This century has witnessed an enormous increase in magnetic energy product, which is the most widely used general measure of hard-magnet performance. This development has guaranteed the application of Nd-Fe-B magnets in the hybrid car motors which require high starting torque and large speed range at constant power. However, for the usage against various demagnetization factors, especially thermal degradation at the typical operating temperature, 200^{o}C also, high coercivity value at room temperature and good thermal stability are highly desired. By examination of real motors, coercivity of around 0.8 T at 200^{o}C is demanded to satisfy practical applications as stable motors. Over 10 wt.% Dy is added in the current commercial sintered magnets to appeal to this requirement. But aside from the great capability of enhancing coercivity, Dy substitution also decreases romance as the antiparallel coupling between Fe and Dy in $Nd_2Fe_{14}B$ phase. Besides, considering the scarce natural reserve of Dy, Dy-saving technique in coercivity enhancement is necessary.

In current work, efforts have been focused on the coercivity enhancement of hot-deformed magnets through the grain boundary diffusion process. Details on experimental techniques, including fabrication and analysis equipment will be introduced in chapter 2. In chapter 3, systematic work is carried out to study the mechanism of coercivity enhancement of the grain boundary diffusion by extending diffusion sources to various eutectic alloys; while in chapter 4, the merit of a quaternary Nd-Fe-Ga-Cu compound as the diffusion source of the eutectic grain boundary diffusion process will be demonstrated, focusing on the effect of retaining high degree of easy-axis texture and possessing more sufficient penetration depth. Chapter 5 describes the employment of heavy rare-earth element, Dy and Tb alloyed Nd-rich eutectics are selected as the diffusion sources, attempting to bring up the coercivity further with utilization the higher anisotropic field of the $(Nd, Dy)_2Fe_{14}B$ or $(Nd, Tb)_2Fe_{14}B$ phase formed on the surface of the matrix phase. Chapter 6 will illustrate the practical prospective when the eutectic grain boundary diffusion process is applied to bulky magnets and discuss the effect of expansion constraint on the magnets during heat treatment. For these aspects of these diffusion processes, careful analysis was carried out by SEM and TEM to characterize grain boundary microstructure as well the interface nature, emphasizing on the understanding of the coercivity enhancement mechanism by the grain boundary diffusion process.

In the final part, concluding remarks will be given by benchmarking current work with conventional sintered magnets to show the merits of the grain boundary process applying to hot-deformed magnets. Moreover, proposals towards the problems unsolved of this work will be made. More importantly, since

some of the practical problems require very sophisticated techniques or knowledge from multi-fields to figure out, pursuing more comprehensive understanding of coercivity will be the life-long journey.

References

[1] O. Gutfleisch, M. A. Willard, E. Brück, C. H. Chen, S. G. Sankar, and J. P. Liu, "Magnetic Materials and Devices for the 21st Century: Stronger, Lighter, and More Energy Efficient," *Adv. Mater.*, vol. 23, no. 7, pp. 821–842, Feb. 2011.

[2] M. Sagawa, S. Fujimura, N. Togawa, H. Yamamoto, and Y. Matsuura, "New material for permanent magnets on a base of Nd and Fe (invited)," *J. Appl. Phys.*, vol. 55, no. 6, pp. 2083–2087, Mar. 1984.

[3] J. J. Croat, J. F. Herbst, R. W. Lee, and F. E. Pinkerton, "Pr-Fe and Nd-Fe-based materials: A new class of high-performance permanent magnets (invited)," *J. Appl. Phys.*, vol. 55, no. 6, pp. 2078–2082, Mar. 1984.

[4] W. M. H., L. J. F., and D. P. C., "Current status of permanent magnet industry in the United States," *Proceeding 20th Int. Workshop RARE EARTH PERMANAENT Magn. THEIR Appl.*, Sep. 2008.

[5] IEA, *Global EV Outlook 2017*. Paris: Organisation for Economic Co-operation and Development, 2017.

[6] S. Hirosawa, Y. Matsuura, H. Yamamoto, S. Fujimura, M. Sagawa, and H. Yamauchi, "Magnetization and magnetic anisotropy of R2Fe14B measured on single crystals," *J. Appl. Phys.*, vol. 59, no. 3, pp. 873–879, Feb. 1986.

[7] J. M. D. Coey, "Permanent magnets: Plugging the gap," *Scr. Mater.*, vol. 67, no. 6, pp. 524–529, Sep. 2012.

[8] K. Hono and H. Sepehri-Amin, "Strategy for high-coercivity Nd–Fe–B magnets," *Scr. Mater.*, vol. 67, no. 6, pp. 530–535, Sep. 2012.

[9] J. F. Herbst, "$R_2Fe_{14}B$ materials: Intrinsic propeties and technological aspects," *Rev. Mod. Phys.*, vol. 63, no. 4, pp. 819–898, Oct. 1991.

[10] J. F. Herbst, J. J. Croat, F. E. Pinkerton, and W. B. Yelon, "Relationships between crystal structure and magnetic properties in Nd2Fe14B," Phys. Rev. B, vol. 29, no. 7, pp. 4176–4178, Apr. 1984.

[11] C. B. Shoemaker, D. P. Shoemaker, and R. Fruchart, "The structure of a new magnetic phase related to the sigma phase: iron neodymium boride Nd2Fe14B," Acta Crystallogr. C, vol. 40, no. 10, pp. 1665–1668, Oct. 1984.

[12] J. Fidler and P. Skalicky, "Metallurgical factors determining the coercivity of ND-FE-B magnets," *Microchim. Acta*, vol. 91, no. 1–6, pp. 115–124, Jan. 1987.

[13] T. T. Sasaki, T. Ohkubo, K. Hono, Y. Une, and M. Sagawa, "Correlative multi-scale characterization of a fine grained Nd–Fe–B sintered magnet," *Ultramicroscopy*, vol. 132, pp. 222–226, Sep. 2013.

[14] T. Fukagawa and S. Hirosawa, "Influence of $Nd/Nd_2Fe_{14}B$ interface microstructure on the coercivity of surface Nd2Fe14B grains in Nd-sputtered Nd–Fe–B sintered magnets," *Scr. Mater.*, vol. 59, no. 2, pp. 183–186, Jul. 2008.

[15] J. Fidler and K. G. Knoch, “Electron microscopy of Nd-Fe-B based magnets,” *J. Magn. Magn. Mater.*, vol. 80, no. 1, pp. 48–56, Aug. 1989.

[16] Y. Shinba, T. J. Konno, K. Ishikawa, K. Hiraga, and M. Sagawa, “Transmission electron microscopy study on Nd-rich phase and grain boundary structure of Nd–Fe–B sintered magnets,” *J. Appl. Phys.*, vol. 97, no. 5, p. 053504, Feb. 2005.

[17] W. Mo, L. Zhang, Q. Liu, A. Shan, J. Wu, and M. Komuro, “Dependence of the crystal structure of the Nd-rich phase on oxygen content in an Nd–Fe–B sintered magnet,” *Scr. Mater.*, vol. 59, no. 2, pp. 179–182, Jul. 2008.

[18] R. Ramesh, “A microstructure based magnetization reversal model in sintered Fe-Nd-B magnets. I,” *J. Appl. Phys.*, vol. 68, no. 11, pp. 5767–5771, Dec. 1990.

[19] F. Vial, F. Joly, E. Nevalainen, M. Sagawa, K. Hiraga, and K. T. Park, “Improvement of coercivity of sintered NdFeB permanent magnets by heat treatment,” *J. Magn. Magn. Mater.*, vol. 242–245, no. Part 2, pp. 1329–1334, Apr. 2002.

[20] W. F. Li, T. Ohkubo, and K. Hono, “Effect of post-sinter annealing on the coercivity and microstructure of Nd–Fe–B permanent magnets,” *Acta Mater.*, vol. 57, no. 5, pp. 1337–1346, Mar. 2009.

[21] T. Schrefl, H. F. Schmidts, J. Fidler, and H. Kronmüller, “The role of exchange and dipolar coupling at grain boundaries in hard magnetic materials,” *J. Magn. Magn. Mater.*, vol. 124, no. 3, pp. 251–261, Jun. 1993.

[22] O. Gutfleisch, “Controlling the properties of high energy density permanent magnetic materials by different processing routes,” *J. Phys. Appl. Phys.*, vol. 33, no. 17, p. R157, 2000.

[23] H. Sepehri-Amin, T. Ohkubo, T. Shima, and K. Hono, “Grain boundary and interface chemistry of an Nd–Fe–B-based sintered magnet,” *Acta Mater.*, vol. 60, no. 3, pp. 819–830, Feb. 2012.

[24] A. Sakuma, T. Suzuki, T. Furuuchi, T. Shima, and K. Hono, “Magnetism of Nd–Fe films as a model of grain boundary phase in Nd–Fe–B permanent magnets,” *Appl. Phys. Express*, vol. 9, no. 1, p. 013002, Dec. 2015.

[25] Y. Murakami *et al.*, “Magnetism of ultrathin intergranular boundary regions in Nd–Fe–B permanent magnets,” *Acta Mater.*, vol. 71, pp. 370–379, Jun. 2014.

[26] T. Nakamura *et al.*, “Direct observation of ferromagnetism in grain boundary phase of Nd-Fe-B sintered magnet using soft x-ray magnetic circular dichroism,” *Appl. Phys. Lett.*, vol. 105, no. 20, p. 202404, Nov. 2014.

[27] T. Kohashi, K. Motai, T. Nishiuchi, and S. Hirosawa, “Magnetism in grain-boundary phase of a NdFeB sintered magnet studied by spin-polarized scanning electron microscopy,” *Appl. Phys. Lett.*, vol. 104, no. 23, p. 232408, Jun. 2014.

[28] T. T. Sasaki, T. Ohkubo, and K. Hono, “Structure and chemical compositions of the grain boundary phase in Nd-Fe-B sintered magnets,” *Acta Mater.*, vol. 115, pp. 269–277, Aug. 2016.

[29] T. Suzuki, Y. Toga, and A. Sakuma, “Effects of deformation on the crystal field parameter of the Nd ions in $Nd_2Fe_{14}B$,” *J. Appl. Phys.*, vol. 115, no. 17, p. 17A703, Jan. 2014.

[30] G. Hrkac *et al.*, "The role of local anisotropy profiles at grain boundaries on the coercivity of $Nd_2Fe_{14}B$ magnets," *Appl. Phys. Lett.*, vol. 97, no. 23, p. 232511, Dec. 2010.

[31] Y. Murakami, T. T. Sasaki, T. Ohkubo, and K. Hono, "Strain measurements from Nd2Fe14B grains in sintered magnets using artificial moiré fringes," *Acta Mater.*, vol. 101, pp. 101–106, Dec. 2015.

[32] U. M. R. Seelam, T. Ohkubo, T. Abe, S. Hirosawa, and K. Hono, "Faceted shell structure in grain boundary diffusion-processed sintered Nd–Fe–B magnets," *J. Alloys Compd.*, vol. 617, pp. 884–892, Dec. 2014.

[33] Y. Kaneko, K. Tokuhara, and N. Ishigaki, "Research on high performance Nd-Fe-B sintered magnets," *Vacuum*, vol. 47, no. 6, pp. 907–910, Jun. 1996.

[34] J. Fidler and J. Bernardi, "Transmission electron microscope characterization of cast and hot-worked R-Fe-B:Cu(R=Nd,Pr) permanent magnets," *J. Appl. Phys.*, vol. 70, no. 10, pp. 6456–6458, Nov. 1991.

[35] J. Bernardi, J. Fidler, M. Sagawa, and Y. Hirose, "Microstructural analysis of strip cast Nd–Fe–B alloys for high (BH)max magnets," *J. Appl. Phys.*, vol. 83, no. 11, pp. 6396–6398, Jun. 1998.

[36] M. Sagawa and H. Nagata, "Novel processing technology for permanent magnets," *IEEE Trans. Magn.*, vol. 29, no. 6, pp. 2747–2751, Nov. 1993.

[37] M. Takahashi, K. Uchida, F. Taniguchi, and T. Mikamoto, "High performance Nd–Fe–B sintered magnets made by the wet process," *J. Appl. Phys.*, vol. 83, no. 11, pp. 6402–6404, Jun. 1998.

[38] M. Sagawa, S. Fujimura, H. Yamamoto, Y. Matsuura, and K. Hiraga, "Permanent magnet materials based on the rare earth-iron-boron tetragonal compounds," *IEEE Trans. Magn.*, vol. 20, no. 5, pp. 1584–1589, Sep. 1984.

[39] P. J. McGuiness, A. Ahmed, D. G. R. Jones, I. R. Harris, S. Burns, and E. Rozendaal, "The hydrogen decrepitation behavior of alloys and magnets based on $Nd_{16}Fe_{76}B_8$," *J. Appl. Phys.*, vol. 67, no. 9, pp. 4626–4628, May 1990.

[40] R. Nakayama, T. Takeshita, M. Itakura, N. Kuwano, and K. Oki, "Magnetic properties and microstructures of the Nd-Fe-B magnet powder produced by hydrogen treatment," *J. Appl. Phys.*, vol. 70, no. 7, pp. 3770–3774, Oct. 1991.

[41] K. Kurima and H. Satoshi, "Chapter 208 Permanent magnets," in *Handbook on the Physics and Chemistry of Rare Earths*, vol. 32, vols., Elsevier, 2001, pp. 515–565.

[42] B. M. Ma, J. W. Herchenroeder, B. Smith, M. Suda, D. N. Brown, and Z. Chen, "Recent development in bonded NdFeB magnets," *J. Magn. Magn. Mater.*, vol. 239, no. 1, pp. 418–423, Feb. 2002.

[43] J. M. D. Coey and K. O'Donnell, "New bonded magnet materials (invited)," *J. Appl. Phys.*, vol. 81, no. 8, pp. 4810–4815, Apr. 1997.

[44] S. Liesert *et al.*, "Preparation of anisotropic NdFeB magnets with different Nd contents by hot deformation (die-upsetting) using hot-pressed HDDR powders," *J. Alloys Compd.*, vol. 266, no. 1, pp. 260–265, Feb. 1998.

[45] R. W. Lee, "Hot-pressed neodymium-iron-boron magnets," *Appl. Phys. Lett.*, vol. 46, no. 8, pp. 790–791, Apr. 1985.

[46] R. Raj, “Morphology and Stability of the Glass Phase in Glass Ceramic Systems,” *J. Am. Ceram. Soc.*, vol. 64, no. 5, pp. 245–248, May 1981.

[47] S. Fushimi and T. Ikeda, “Phase Equilibrium in the System PbO-TiO2–ZrO2,” *J. Am. Ceram. Soc.*, vol. 50, no. 3, pp. 129–132, Mar. 1967.

[48] R. K. Mishra, “Microstructure of melt-spun Nd-Fe-B magnequench magnets,” *J. Magn. Magn. Mater.*, vol. 54–57, pp. 450–456, Feb. 1986.

[49] J. J. Croat, “Manufacture of Nd-Fe-B permanent magnets by rapid solidification,” *J. Common Met.*, vol. 148, no. 1–2, pp. 7–15, Apr. 1989.

[50] M. Leonowicz and H. A. Davies, “Effect of Nd content on induced anisotropy in hot deformed Fe-Nd-B magnets,” *Mater. Lett.*, vol. 19, no. 5–6, pp. 275–279, May 1994.

[51] R. K. Mishra, E. G. Brewer, and R. W. Lee, “Grain growth and alignment in hot deformed Nd-Fe-B magnets,” *J. Appl. Phys.*, vol. 63, no. 8, pp. 3528–3530, Apr. 1988.

[52] Hae-woong Kwon, Y. S. Kang, G. S. Choi, and J. H. Yu, “Effect of Grain Size and Die-Upset Temperature on Texture in Die-Upset Nd-Fe-B Magnet,” *IEEE Trans. Magn.*, vol. 45, no. 6, pp. 2590–2593, Jun. 2009.

[53] S. Guruswamy, Y. R. Wang, and V. Panchanathan, “Plastic deformation modeling of die-upset process for magnequench NdFeB magnets,” *J. Appl. Phys.*, vol. 83, no. 11, pp. 6393–6395, Jun. 1998.

[54] M. Leonowicz, D. Derewnicka, M. Wozniak, and H. A. Davies, “Processing of high-performance anisotropic permanent magnets by die-upset forging,” *J. Mater. Process. Technol.*, vol. 153–154, pp. 860–867, Nov. 2004.

[55] L. Li and C. D. Graham, “The origin of crystallographic texture produced during hot deformation in rapidly-quenched NdFeB permanent magnets,” *IEEE Trans. Magn.*, vol. 28, no. 5, pp. 2130–2132, Sep. 1992.

[56] R. K. Mishra and R. W. Lee, “Microstructure, domain walls, and magnetization reversal in hot-pressed Nd-Fe-B magnets,” *Appl. Phys. Lett.*, vol. 48, no. 11, pp. 733–735, Mar. 1986.

[57] R. Lee, E. Brewer, and N. Schaffel, “Processing of Neodymium-Iron-Boron melt-spun ribbons to fully dense magnets,” *IEEE Trans. Magn.*, vol. 21, no. 5, pp. 1958–1963, Sep. 1985.

[58] P. Tenaud, A. Chamberod, and F. Vanoni, “Texture in Nd-Fe-B magnets analysed on the basis of the determination of $Nd_2Fe_{14}B$ single crystals easy growth axis,” *Solid State Commun.*, vol. 63, no. 4, pp. 303–305, Jul. 1987.

[59] W. Grünberger, D. Hinz, A. Kirchner, K.-H. Müller, and L. Schultz, “Hot deformation of nanocrystalline Nd-Fe-B alloys,” *J. Alloys Compd.*, vol. 257, no. 1–2, pp. 293–301, Jul. 1997.

[60] J. Song *et al.*, “Structure and magnetic properties of bulk nanocrystalline Nd-Fe-B permanent magnets prepared by hot pressing and hot deformation,” *J. Rare Earths*, vol. 31, no. 7, pp. 674–678, Jul. 2013.

[61] G. M. Pharr and M. F. Ashby, “On creep enhanced by a liquid phase,” *Acta Metall.*, vol. 31, no. 1, pp. 129–138, Jan. 1983.

[62] C. Rong *et al.*, "Effect of pressure loading rate on the crystallographic texture of NdFeB nanocrystalline magnets," *J. Appl. Phys.*, vol. 111, no. 7, p. 07A717, Feb. 2012.

[63] Y. Nozawa, K. Iwasaki, S. Tanigawa, M. Tokunaga, and H. Harada, "Nd-Fe-B die-upset and anisotropic bonded magnets (invited)," *J. Appl. Phys.*, vol. 64, no. 10, pp. 5285–5289, Nov. 1988.

[64] C. D. Fuerst and E. G. Brewer, "Diffusion-alloyed additives in die-upset Nd-Fe-B magnets," *J. Appl. Phys.*, vol. 69, no. 8, pp. 5826–5828, Apr. 1991.

[65] A. Kirchner, J. Thomas, O. Gutfleisch, D. Hinz, K.-H. Müller, and L. Schultz, "HRTEM studies of grain boundaries in die-upset Nd–Fe–Co–Ga–B magnets," *J. Alloys Compd.*, vol. 365, no. 1–2, pp. 286–290, Feb. 2004.

[66] J. D. Livingston, "A review of coercivity mechanisms (invited)," *J. Appl. Phys.*, vol. 52, no. 3, pp. 2544–2548, Mar. 1981.

[67] G. C. Hadjipanayis and A. Kim, "Domain wall pinning versus nucleation of reversed domains in R-Fe-B magnets (invited)," *J. Appl. Phys.*, vol. 63, no. 8, pp. 3310–3315, Apr. 1988.

[68] K.-D. Durst and H. Kronmüller, "The coercive field of sintered and melt-spun NdFeB magnets," *J. Magn. Magn. Mater.*, vol. 68, no. 1, pp. 63–75, Aug. 1987.

[69] F. E. Pinkerton and C. D. Fuerst, "Coercivity of die upset Nd-Fe-B magnets: A strong pinning model," *J. Magn. Magn. Mater.*, vol. 89, no. 1, pp. 139–142, Sep. 1990.

[70] P. Gaunt, "Domain Wall Pinning as a Source of Magnetic Hardening in Alloys," *J. Appl. Phys.*, vol. 43, no. 2, pp. 637–638, Feb. 1972.

[71] H. Kronmüller, K.-D. Durst, and M. Sagawa, "Analysis of the magnetic hardening mechanism in RE-FeB permanent magnets," *J. Magn. Magn. Mater.*, vol. 74, no. 3, pp. 291–302, Oct. 1988.

[72] G. B. Ferguson, K. O'Grady, and J. Popplewell, "Magnetisation mechanisms and magnetic viscosity in NdFeB alloys," *IEEE Trans. Magn.*, vol. 25, no. 5, pp. 3449–3451, Sep. 1989.

[73] F. E. Pinkerton and D. J. Van Wingerden, "Magnetization process in rapidly solidified neodymium-iron-boron permanent magnet materials," *J. Appl. Phys.*, vol. 60, no. 10, pp. 3685–3690, Nov. 1986.

[74] H.-R. Hilzinger and H. Kronmüller, "Pinning of curved domain walls by randomly distributed lattice defects," *Phys. BC*, vol. 86–88, no. Part 3, pp. 1365–1366, Jan. 1977.

[75] H. R. Hilzinger and H. Kronmüller, "Statistical theory of the pinning of Bloch walls by randomly distributed defects," *J. Magn. Magn. Mater.*, vol. 2, no. 1, pp. 11–17, Dec. 1975.

[76] D. I. Paul, "General theory of the coercive force due to domain wall pinning," *J. Appl. Phys.*, vol. 53, no. 3, pp. 1649–1654, Mar. 1982.

[77] Hono K., Ohkubo T., and Sepehri-Amin H., "Microstructure-Coercivity Relationships of Nd-Fe-B Base Permanent Magnets," *J. Jpn. Inst. Met.*, vol. 76, no. 1, pp. 2–11, 2012.

[78] R. Ramesh and K. Srikrishna, "Magnetization reversal in nucleation controlled magnets. I. Theory," *J. Appl. Phys.*, vol. 64, no. 11, pp. 6406–6415, Dec. 1988.

[79] R. Ramesh, G. Thomas, and B. M. Ma, “Magnetization reversal in nucleation controlled magnets. II. Effect of grain size and size distribution on intrinsic coercivity of Fe-Nd-B magnets,” *J. Appl. Phys.*, vol. 64, no. 11, pp. 6416–6423, Dec. 1988.

[80] W. F. Li, T. Ohkubo, K. Hono, and M. Sagawa, “The origin of coercivity decrease in fine grained Nd–Fe–B sintered magnets,” *J. Magn. Magn. Mater.*, vol. 321, no. 8, pp. 1100–1105, Apr. 2009.

[81] H. Sepehri-Amin, T. Ohkubo, M. Gruber, T. Schrefl, and K. Hono, “Micromagnetic simulations on the grain size dependence of coercivity in anisotropic Nd–Fe–B sintered magnets,” *Scr. Mater.*, vol. 89, pp. 29–32, Oct. 2014.

[82] M. Seeger, J. Bauer, H. Kronmüller, J. Bernardi, and J. Fidler, “Magnetic and microstructural properties of sintered FeNdB-based magnets with Ga and Nb additions,” *J. Magn. Magn. Mater.*, vol. 138, no. 3, pp. 294–300, Dec. 1994.

[83] N. Haque, A. Hughes, S. Lim, and C. Vernon, “Rare Earth Elements: Overview of Mining, Mineralogy, Uses, Sustainability and Environmental Impact,” *Resources*, vol. 3, no. 4, pp. 614–635, Oct. 2014.

[84] T.-H. Kim, S.-R. Lee, H.-J. Kim, M.-W. Lee, and T.-S. Jang, “Simultaneous application of Dy–X (X=F or H) powder doping and dip-coating processes to Nd–Fe–B sintered magnets,” *Acta Mater.*, vol. 93, pp. 95–104, Jul. 2015.

[85] G. Rieger, M. Seeger, L. Sun, and H. Kronmüller, “Micromagnetic analysis applied to melt-spun NdFeB magnets with small additions of Ga and Mo,” *J. Magn. Magn. Mater.*, vol. 151, no. 1, pp. 193–201, Nov. 1995.

[86] J. Bauer, M. Seeger, and H. Kronmüller, “Magnetic properties and microstructural analysis of rapidly quenched FeNdBGaNb permanent magnets,” *J. Magn. Magn. Mater.*, vol. 139, no. 3, pp. 323–334, Jan. 1995.

[87] D. C. Crew, L. H. Lewis, and V. Panchanathan, “The effect of evolving grain shape and alignment on the coercivity in thermomechanically deformed $Nd_{13.9}(Fe_{0.92}Co_{0.08})_{80.3}B_{5.3}Ga_{0.5}$ permanent magnets,” *J. Magn. Magn. Mater.*, vol. 223, no. 3, pp. 261–266, Feb. 2001.

[88] W. B. Cui, Y. K. Takahashi, and K. Hono, “Microstructure optimization to achieve high coercivity in anisotropic Nd–Fe–B thin films,” *Acta Mater.*, vol. 59, no. 20, pp. 7768–7775, Dec. 2011.

[89] M. Grönefeld and H. Kronmüller, “Initial magnetization curve and hardening mechanism in rapidly quenched Nd-Fe-B magnets,” *J. Magn. Magn. Mater.*, vol. 88, no. 3, pp. L267–L274, Aug. 1990.

2 Chapter 2 Experimental

2.1 General introduction

In this chapter, basic principle of the instruments and devices that are used in the different topics from Chapter 3 to 6 will be introduced. Since in this work, the hot-deformed magnets are provided from our collaborators, the processing detail will not be included. Alloys applied as diffusion sources are prepared with single-roller melt-spinning technique. The melt-spun ribbons are crushed into powders or flakes with them soaked in organic solution to avoid from oxidization. The same solution is also used for the temporal storage of ribbons. Melting-point of the melt-spun ribbons is measured by differential thermal analysis (DTA). Diffusion process is carried out with rapid thermal annealing (RTA) furnace. The magnetic properties of bulk samples are measured with B-H loop tracer, while the hysteresis loops of small size specimen are obtained by a superconducting quantum interface devices (SQUIDs) with the vibrating scanning magnetometer (VSM) sensors. It has been discussed in Chapter 1 that coercivity of Nd-Fe-B magnets, as extrinsic property, can be adjusted by optimizing microstructure and chemistry of the intergranular phase. The observation of the characteristics of intergranular phase as well as the interface between the $Nd_2Fe_{14}B$ phase and the intergranular phase is essential to understand the coercivity mechanism of Nd-Fe-B permanent magnets, as a result, to develop high-performance Nd-Fe-B permanent magnets. Given to existence of the grain boundary phase with extremely small thickness of around 2 nm, characterization techniques with ultra-high resolution is necessary, such as STEM imaging and atom probe tomography. All the analysis methods will be listed out and generally described in this chapter. These techniques include scanning electron microscope (SEM), transmission electron microscope (TEM) and three-dimensional atom probe tomography (3DAP). To outline the experimental procedure of our research, we will start with a brief explanation of melt-spinning process, RTA furnace and DTA principle, followed by introduction of different characterization instruments and techniques.

2.2 Melt-spinning, DTA and RTA furnace

a) Melt-spinning

Melt-spinning is a technique used for rapid cooling liquids. A wheel is cooled internally, usually by water or liquid nitrogen, and rotated. A thin stream of liquid is then dripped onto the wheel and cooled, causing rapid solidification. This technique is used to develop materials that require extremely high cooling rate in order to form, such as metallic glass. The cooling rates achievable by melt-spinning are in the order of 10^4-10^7 K/S.

It has been shown that many physical properties of melt-spun ribbons as well as the thermal stability of non-equilibrium structures sensitively depend on the values of the processing parameters such as the wheel speed, V_S, gas ejection pressure, P_E, melt temperature, T_E, nozzle-wheel gap etc.

It is found [1] that the cooling rate at the vicinity of the melting temperature monotonically increases by increasing the wheel surface speed, while the ribbon thickness decreases. Both the thickness of melt-spun ribbons and the cooling rates increase with applied ejection pressure. Increasing the melt-temperature leads to smaller ribbon thickness and lower cooling rates at the melting temperature.

In this work, the melt-spun ribbons were fabricated by a laboratory scale single roller melt-spinning device. Target alloys were placed into quartz crucibles of internal diameter 14 mm, melted in a resistance furnace under flowing argon and then gas ejected through the nozzle with a circular or slot-shaped orifice onto the outer surface of the rotating quenching wheel (22 cm in diameter) made of aluminum bronze.

Before each melt-spinning run, the outer surface of the quenching wheel was polished with 1200 grit silicon carbide paper. In order to get the ribbons of similar thickness, each melt-spinning run, the diameter of the nozzles was 0.80 mm and the distance from the tip of the nozzle to the wheel surface was kept at 1 cm throughout the study. When the vacuum level approaches ~10^{-3} Pa, before ejection of the melt, Ar gas is introduced to make the chamber pressure around 0.05 of the atmosphere pressure to avoid severe evaporation of rare-earth elements. The partial pressure in the nozzle is kept as 10 kPa since the total amount of the alloy in the quartz crucible of one batch is only around 3~5 grams. After the fabrication, melt-spun ribbons were kept in organic solutions to protect from oxygen and moisture. In this work, the long-chain alkane Heptane (C_7H_{16}) is used because of its low boiling point ~90.5 ^{o}C which ensures its complete vaporization during the heat-treatment and in turn results in no influence on the magnetic properties that may come from carbon residues.

b) DTA devices

Differential thermal analysis is a technique in which the temperature difference between an active substance and the reference sample (non-reactive) is measured as a function of the programed temperature when both are subjected to identical heat flow by separate heating coils. Thermocouples are placed close to the sample holder to ensure the uniform distribution of temperature. However, since the thermocouples should not be in direct contact with tested samples to avoid contamination, their sensitivity is compromised, which is also one of the cause of the low detection sensitivity of DTA measurement.

When the temperature difference, known as differential temperature is recorded against time or the programed temperature, we can obtain the DTA curve. It is conventional to represent the endothermic effect as a negative deflection and the exothermic effect by a positive deflection. The peak temperature is considered as the starting point of the transformation followed with a broad range till completion. There is theory and experimental results [2] claiming that although the peak shape can be affected by the sample weight, surface-to-volume ration, thermal conductivity, heating rate et al, the onset temperature remains the same. When the heating rate increases, the peak of the endothermic reaction will shift to higher temperature due to the change of activation energy under different heating rate.

To avoid the large errors in the peak temperature shift, calibration with known melting point (in this work, potassium chloride KCl) was used before the melting-point measurement of the melt-spun ribbons. In this experiment, DSC was applied to study the melting temperature of ribbons, so as to offer a reference in

choosing the proper heat treatment temperature. The detection temperature range in this work is from 20°C to 900°C, heating rate set as 10°C/min; Al_2O_3 ceramics boat was used as the reference as well as the container for ribbons, the whole measurement was completed with the Ar gas flow to exclude oxidation reaction.

c) RTA furnace

The diffusion process of this work was performed with the rapid thermal annealing (RTA) furnace. This equipment can offer a heating rate of ~50°C/s with a unique lamp arrangement of 6 quartz halogen lamps located surrounding the small-sized chamber with only 10 cm in diameter. The high heat ramp rate allows the minimum time exposed to the temperature other than the targeted temperature. In addition, the thermocouples buried in susceptors absorbing the lamp power and re-radiate a more uniform light over the silicon wafer in the meantime produce measurable voltage for accurate temperature control. These features ensure the good uniformity in the heating chamber and reproducibility of processing. The RTA furnace applied for heat-treatment in this research is equipped with a rotary pump and a diffusion pump, ensuring the vacuum level of 10^{-3} during the process.

2.3 Magnetic properties measurement devices

a) B-H tracer

The (static) magnetic properties measurement of the bulky samples in this research is carried out on the close-circuit B-H loop tracer, TM-BH30-C1. Figure 2 is a photo of the B-H tracer developed by Tamakawa (a) and the schematic drawing showing the test system (b). In the measurement of the hysteresis, the cubic-shaped sample is placed between the two pieces of an electromagnet with two yokes designed with high-permeability materials, e.x. Ni, FeNi. The effective magnetic field acting on the test samples is nearly the applied field because of the absence of demagnetizing field effect since B-coil is wound around the test sample. The strength of the magnetic field, *H*, and the flux density, *B*, are obtained by integration of the induced voltage in the H-coil and B-coil, respectively. In the B-H loop tracer used in this work, the maximum applied field is 3 T, the B-coil is 10 mm in diameter and 4 mm in thickness, the pole-piece gap can be changed from 0 to 120 mm. The calibration of the induction flux density is carried out with high-purity Ni sample in the size of 7×7×5.6 mm^3. The shift in phase and magnitude of the induced voltage from

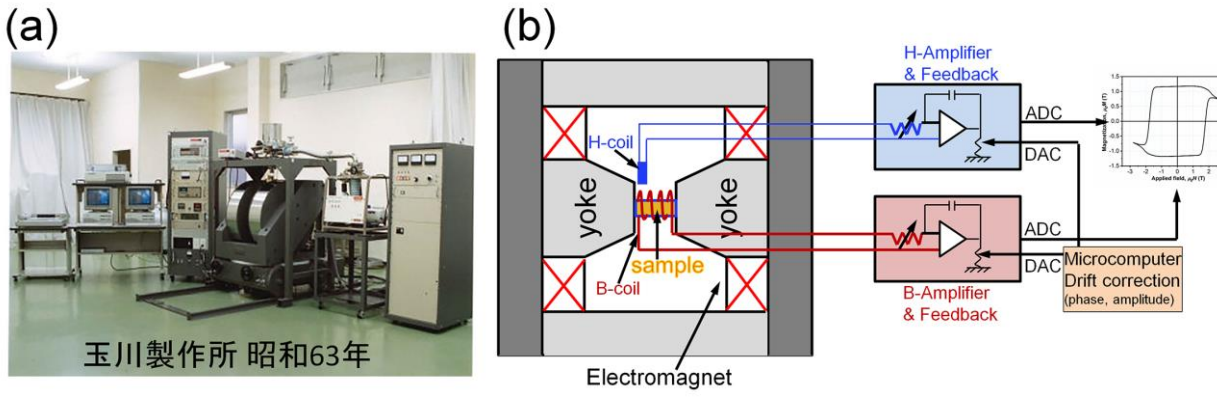

Fig. 2-1 (a) Photo of the B-H loop tracer, (b) schematic illustration of the test system.

the analogue to digital converter (ADC) and digital to analogue converter (CDA) is corrected by the feedback control system by the microcomputer [3]. Prior to the measurement of B-H curves, the cubic-shaped sample is magnetized with a 7T-pulse magnetic field.

b) Superconducting quantum interface devices (SQUIDs)

The SQUID system used in this research is manufactured by Quantum Design (MPMS 3). It measures the longitudinal magnetic moment of a specimen, i.e. along the direction of the applied magnetic field. The magnetic field that can be set over the sample space is in the range of -7 T$\leq \mu_0 H \leq$ 7 T. The sample space is located within two "pick-up" coils surrounded by the superconducting magnet. In the measurement in the mode of vibrating scanning magnetometer, the sample is moved vertically through the detection coil, the magnetic moment of the sample will induce an electric current in the detection coils, which in turn produces the corresponding variations in the SQUID output voltage. The conversion constant represents the coupling between the sample and the detection coils and it is independent on the sample geometry.

The SQUID magnetometer is a very sensitive instrument with the minimum detection magnetic moment of ~10^{-7} emu. However, since the some of the flux lines of a small sample will close inside the oils, thus not being detected, the change in sample geometry will produce a different dependence of magnetic flux against position. This "moment artifact" caused by the shape effect of the test specimen and also be affected by the vibrating amplitude set in the measurement sequence. The multiplicative factor for calibration of the magnetic moment is given by Quantum Design [4] using standard Pd sample in cylinder shape under different peak vibration amplitudes from 0.5 mm to 8.0 mm. Despite the calibration covers various dimensions of Pd samples, the real specimen used for the magnetic properties measurement is usually in prism configuration with varied dimensions. In this work, the magnetic moment of each execution for accurate estimation of magnetization value is calibrated with high-purity Ni standard sample which is fabricated with exactly same dimension as the real specimen. The magnetization employed for calibration is 54.27 emu/g [5]. Consider the density of Ni reported in literature varies a lot from each other, the calibration is better not to be based on the magnetization value which corresponds to magnetic moment per volume.

2.4 Microstructure characterization instruments and techniques

In this research, different characterization methods with different resolutions were used to study macro scale to micro scale microstructure of Nd-Fe-B permanent magnets to understand the effect of intergranular phase as well as the interface between the $Nd_2Fe_{14}B$ phase and the intergranular phase on the magnetic properties especially coercivity. For the purpose of analysis to different scales, focus ion beam was employed to prepare TEM and atom probe samples, as well as to get a smooth and clean surface of hot-deformed Nd-Fe-B magnets for scanning electron microscope (SEM) observation. To understand the structure and chemistry of intergranular phase as well as the interface between $Nd_2Fe_{14}B$ phase of hot-deformed Nd-Fe-B magnets. STEM imaging with HAADF detector and locally built laser assisted 3D atom probe was used. This part will be comprised with the introduction of different analysis instruments and

techniques and a brief explanation of the preparation of TEM and atom probe samples at the end of this chapter.

2.4.1 Focus ion beam

The conventional focused ion beam system consists of a vacuum system and chamber, a liquid metal ion source, and ion column, a sample stage, detectors, gas delivery system, and a computer to sun the complete system. In the FIB system, focused ion beam of ions are used for milling the sample surface as well as imaging. There are different sources of liquid metal ions, in this research, Ga was used as the metal source in the Helios NanoLab™ 650 (Figure 1(a)). Helios Nanolab 650 features FEI's highly engineered advances in field emission SEM (FESEM) and focused ion beam (FIB) technologies and their combined use. It is designed to access the world of extreme high resolution (XHR) 2D and 3D characterization, high-quality sample preparation. Robust, precise FIB slicing, combined with a high precision (150 x 150 µm) piezo stage and superb SEM performance, allows automated software for unattended sample preparation or 3D characterization and analysis ("Slice and View"). It is equipped with an OmniProbe micromanipulator for TEM sample preparation. The instrument has superb imaging capabilities, providing sub-nanometer resolution across the whole 1-30 kV range. Its through-the-lens detector sets collection efficiency of both secondary electrons (SE) and on-axis backscattered electrons (BSE), and is complemented by two multi-segment solid state detectors, a detector for backscattered electron (BSE) imaging able to detect low kV BSE and a third detector dedicated to FIB-SE and FIB-SI (secondary ion) imaging.

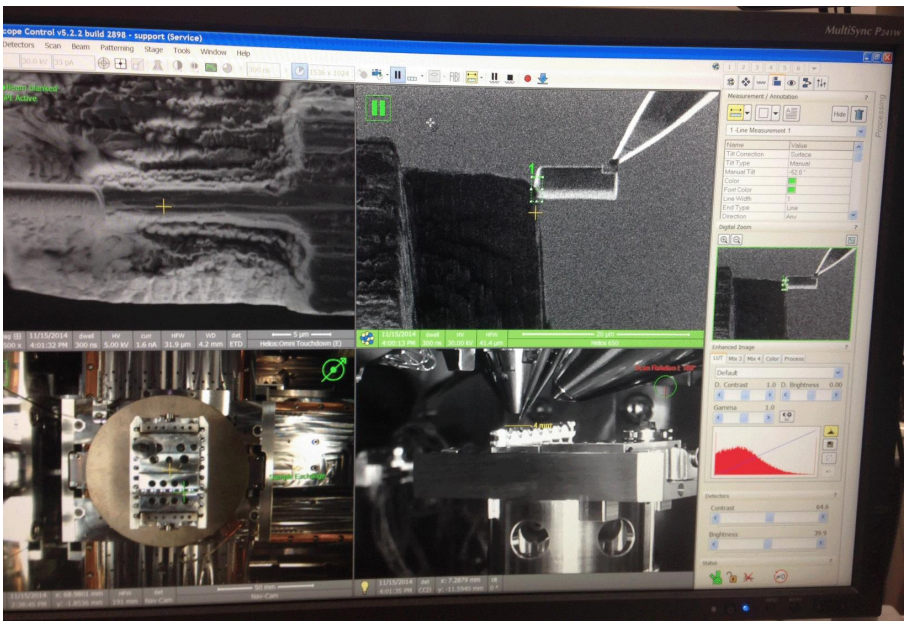

Fig. 2-2 (a) FIB instrument (FEI Helios NanoLab 650) used in this work, (b) an example of operation interface during TEM sample preparation.

OmnipProbe (a sharp W needle) can be used for lifting out a desirable part of sample. The focused ion beam system in Helios NanoLab features excellent FIB imaging, outstanding low kV operation down to 500 V, and up to 65 nA beam current. The increased sensitivity allows the system to operate at much lower beam currents or low accelerating voltage, which reduces the risk of sample damage.

In this work, a focused ion beam instrument (FEI Helios NanoLab ™ 650) was used for sample preparation for transmission electron microscopy (TEM) and 3D atom probe tomography studies.

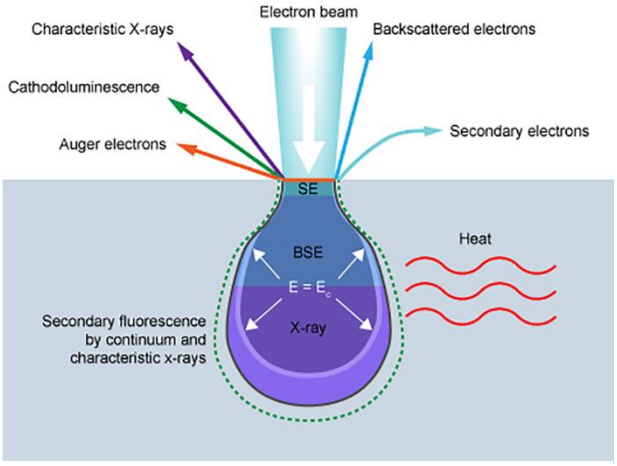

Fig. 2-3 The electron-matter interaction volume involving elastic and inelastic scattering.

2.4.2 Scanning electron microscope (SEM)

Scanning electron microscope is a characterization instrument in which a beam of electrons is employed to get information mainly related with surface or near surface morphology. A SEM machine consists of an electron gun, condenser lenses, a vacuum system and different equipped detectors for various applications. The SEM machine used in this research possesses a field emission gun (FEG) for providing electron beams. The electrons can be accelerated with energy usually between 1 keV to 30 keV. Using condenser lenses, the beam of electrons are magnified as it heats the specimen with a diameter between 2 to 10 nm. The specimen's region into which the electrons penetrate is known as the interaction volume; the various radiations are generated as a result of inelastic scattering which is shown in Figure 3.

The main reflected signals are secondary electrons, backscattered electrons, X-rays and cathodoluminescene. After interactions with the specimen, different radiations will be produced from specific depths of sample. The reflected signals will be used for different imaging purposes in SEM. Secondary electrons and backscattered electrons are used to study different parts of sample since the signals come from different depths of surface of sample. Secondary electrons are used to provide the information closer to the surface of sample, so they can be used for the study of sample surface tomography. However, backscattered electron images can be produced using backscattered electrons that come from deeper depths of sample; they can be used for the study of different phases in the microstructure. Moreover, the contrast of the backscattered images depends on the atomic number of elements in specific phases. Thus the phase containing heavier elements will show brighter contrast and the phase containing lighter elements will show darker contrast in the backscattered images. X-rays are used primarily for chemical analysis using energy dispersive spectroscope detector. With lower voltage analysis, we can avoid taking deep effective volume, so as to increase the accuracy in surface morphology characterization. In this research, Carl ZEISS CrossBeam 1540EsB instrument was used for SEM observations and surface of samples was cleaned using FIB before SEM observation.

2.4.3 Transmission electron microscopy (TEM) imaging

Transmission electron microscope is a type of electron microscope. In this microscope, a series of magnetic lenses are employed to focus an accelerated electron beam on the thin sample in vacuum. The TEM instrument used in this research is FEI Titan G2 80-200 (as shown in Figure 4). Different imaging techniques used in this work are explained as below:

a) Conventional TEM imaging (BF and DF)

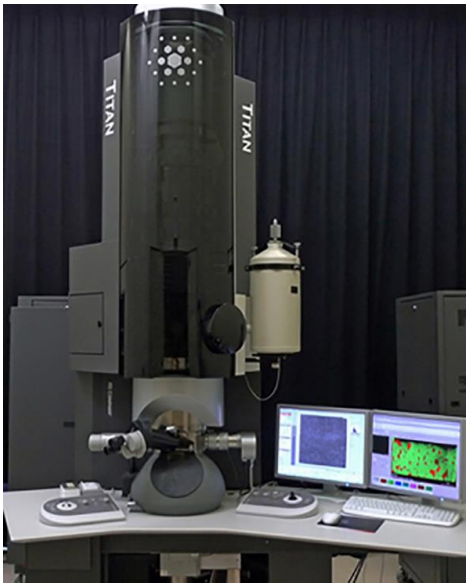

Fig. 2-4 Cs-corrector equipped FEI Titan G2 80-200.

Bright field (BF) and dark field (DF) TEM are the simplest and very useful TEM techniques. In these techniques, with use of an objective aperture, undiffracted or diffracted electrons can be selected to form a bright field (BF) or a dark field (DF) images, respectively. A bright field (BF) image, formed by the central direct beam, normally gives information about how the materials structure looks like, especially the grain structure and interfacial phases. However, dark field (DF) image, gives information regarding to the diffracted electrons. This information sometimes cannot be obtained from bight field (BF) images. One useful application of DF image is showing a particular phase or precipitate. With selecting the diffracted electrons which correspond to specific secondary phase or precipitates, we can get information from imaging of the related precipitates or secondary phase with selecting diffracted spot using objective aperture. By using selected area diffraction (SAD), the phases in the microstructure can be identified by analyzing the diffraction pattern. If the phases are too small, micro or nano beam diffraction pattern can help. With the use of BF imaging, DF imaging and SAD pattern, further study of the sample microstructure can be developed.

b) STEM imaging with HAADF detector

In a STEM mode, we can have more flexibility than in a TEM mode because, by varying the camera length L, we can change the collection angle of the detector and create, in effect, a variable objective aperture. This means we can have more control over which electrons would contribute to the image contrast. Low angle scattered electrons are elastically scattered electrons, for example, Bragg electrons, these electrons will always give the diffraction contrast and phase contrast.

The technique of HAADF-STEM imaging technique is also termed as Z-contrast microscopy. It only collects high-angle scattered electrons, i.e. Rutherford scattering with scattered intensity proportional to Z^2, to form an image which provides an incoherent image of crystals at atomic resolution. There are no phases in an incoherent image, therefore, no phase problem for structure determination. Location of atom column positions in an image is greatly simplified. In addition, the resolution is a factor of two higher than in a coherent image, the formation is more localized, the intensity of atom columns directly reflects their mean

square atomic number (Z), and there are no contrast reversals with crystal thickness. It is also the only means to achieve spectroscopy from individual atomic columns.

Unlike the conventional TEM, Z-contrast imaging is free of thickness limitation. However, it is more sensitive to surface damage or amorphous layers produced during the specimen preparation for example by ion milling process, ion re-deposition, et al. In practice, such layers scatter the beam randomly, resulting in the fluctuations in the intensity from otherwise identical columns which appear like image noise.

Contrast reversal can occur due to multiple elastic scattering, independent of the channeling conditions. A high-Z material is a more efficient scatterer. In thin specimens, it scatters the most to the high angle detector, and is seen brightest in the image. With increasing thickness it remains the most efficient scatterer, so will be the first to scatter to angles greater than the outer than a material of lower Z, both on and off a zone axis.

c) TEM sample preparation

Proper sample thickness is necessary for TEM observation with good resolution as well as the interpretation of TEM images. Optimum sample thickness is dependent on the technique of sample preparation. In this research, the TEM sample preparation was carried out in Helios NanoLab 650. A block with 12 μm length, 3 μm width and 5μm height was fabricated and lifted out from the bulk sample using Omniprobe that equipped in the FIB system of Helios NanoLab. The TEM sample is prepared by pasting the block to a Mo grid with Pt deposition and following with milling by Ga ions to reduce its thickness to around 50 nm. Delicate fabrication of TEM sample was realized by the utilization of the ion beam in FIB system with different voltages and current levels, ranging from 30 kV to 500 V for voltage and 64 nA to 16 pA for current. The preparation of TEM samples was ended with the cleaning by “ion-beam shower” at low voltage, weak current of 2 kV, 25 pA to remove the FIB damaged layer on the surface and to make the specimen thinner.

2.4.4 Three dimensional atom probe tomography

Three dimensional atom probe (3DAP) is a strong instrument for the study of the chemistry and structure of materials in nano-scale. High spatial resolution of this technique makes it superior to other characterization techniques in the aspect of ultra-high resolution. Using 3DAP, the distribution of different elements can be constructed in three dimensions. Atom probe is the only analytical technique that is capable of analyzing light elements such as H and Li quantitatively in the nano scale dimension. The progress in atom probe field ion microscopy (APFIM) and its application to nanoscale microstructural studies of metallic materials was explained in previous studies. In this thesis, a locally built laser assisted atom probe (LA3DAP) was used. It consists of three UHV chambers, air lock, specimen storage, and analysis chamber. The machine and the laser system are shown in Figure 7. Specimens can be kept in the specimen storage through the air lock chamber. The specimens for the atom probe experiment should be needle shape samples with the apex diameter of less than 100 nm. The procedure of the atom probe sample preparation will be explained in the next part. During the analysis, the sample is kept in the analysis chamber in an ultra -high vacuum and a low

temperature. A DC voltage is applied on the sample during analysis and using a femto second pulse laser; the atoms on the apex of the sample are ionized and fly to a delay line detector. Thereafter, according to the time of flight of each individual ionized atoms, using the position sensitive detector (PSD), two dimensional atomic distribution can be identified according to the ionization of each layer of atoms from the atom probe tip. With continuing the atom probe analysis and ionization of atoms layer by layer, three dimensional elemental maps can be constructed. The mechanism of the ionization of atoms with the help of femto second pulse laser is shown schematically in Figure 8. The acquired data were analyzed using the PoSAP analysis software (Oxford nanoscience version 1.70). Using this software, the atomic distribution of different elements and chemical composition in nano-scale for different phases even in nano-size can be determined from the acquired data.

2.4.5 Atom probe sample preparation

Preparation of atom probe tip is the most difficult part of atom probe experiment. The atom probe tip should have an apex diameter of less than 100 nm. Also, the desire region for the atom probe tomography should exist in a region less than 150 nm far from the top of the tip. In this study, the atom probe tip was prepared from Nd-Fe-B hot-deformed magnets. The specimen for atom probe was prepared by a FIB system in Helios NanoLab 650 and the liftout method that is similar with TEM sample preparation. The fabrication of a preliminary atom probe sample can be made by lifting out one block from the bulk sample using lift-out metho and pasted on the tip of a sharpened W needle. The final preparation of the specimen was made using a precise FIB/SEM system (Carl ZEISS CrossBeam 1540 EsB). The atom probe samples were milled using Ga ions. Thereafter, the diameter of the sample was decreased by finer milling to around 300 nm using annular milling.

References

[1] V. I. Tkatch, A. I. Limanovskii, S. N. Denisenko, and S. G. Rassolov, "The effect of the melt-spinning processing parameters on the rate of cooling," *Mater. Sci. Eng. A*, vol. 323, no. 1-2, pp. 91-96, Jan. 2002.

[2] H. E. Kissinger, "Variation of peak temperature with hearing rate in differential thermal analysis," *J. Re. Natl. Stand. Sec C*, vol. 57, no. 4, Oct. 1956.

[3] S. Kusui, M. Kosukegawa, and M. Inoue, "DC B-H curve tracer with error correction and constant measuring and drawing speed using microcomputer," *Electron. Lett.*, vol. 26, no. 13, pp. 902-903, Apr. 1990.

[4] Quantum design, "Accuracy of the reported moment: sample shape effects," *Appl. Note* 1500-015, Rev. A0, Oct. 2010.

[5] ASTM Test Method C 527-63T. "Saturation magnetization or saturation induction of nonmetallic magnetic materials."

3 Chapter 3 Coercivity enhancement of hot-deformed Nd-Fe-B magnets by the eutectic grain boundary diffusion process using various eutectic alloys

3.1 Introduction

The hot-deformed Nd-Fe-B permanent magnets, which are fabricated from melt-spun isotropic nanocrystalline powders, followed by hot-pressing and hot-deformation, have distinguishable feature in terms of grain size that is typically ~100 nm in thickness and 300~400 in width [1,2]. The platelet-shaped $Nd_2Fe_{14}B$ grains exhibit in the strong (001) texture which is developed during the hot-deformation or upsetting process [3, 4]. The underlying mechanism could be considered to be due to the orientation dependent grain growth of tetragonal $Nd_2Fe_{14}B$ phase [4-7] or the anisotropy of its elastic properties [8]. The coercivity of anisotropic hot-deformed Nd-Fe-B magnets is relatively larger than that of sintered magnets; moreover, the temperature dependence of coercivity is also improved due to the reduced stray field as a result of the ultrafine grain size that is comparable to the single domain size. With proper hot-deformation process, the hot-deformed magnets can retain the remanent magnetization $\mu_0 M_r$ of 1.4 T which is comparable to that of commercial Nd-Fe-B sintered magnets [9, 10]. Thus this indicates us the anisotropic hot-deformed magnets can attain competitive room temperature magnetic properties as sintered magnets. And with the merit of better thermal stability, the hot-deformed magnets should have the potential for realizing high-performance at elevated temperature. Blending DyF_3 and DyCu alloys with melt-spun Nd-Fe-B ribbons followed by hot-pressing and hot-deformation were found to be capable of improving coercivity by formation of the thin $(Nd,Dy)_2Fe_{14}B$ layer [11,12]. However, even with Dy addition, the highest coercivity so far reported for the anisotropic hot-deformed magnets was limited to around 2.0 T.

The low coercivity of HRE-free anisotropic hot-deformed magnets has been explained by Lewis et al. [13-15] as the exchange coupling between $Nd_2Fe_{14}B$ grains through a ferromagnetic intergranular phase that shows highly enrichment of Fe and Co. From their previous investigation, anisotropic distribution behavior of the intergranular phase was also revealed, as the preferential formation on the flat surface of the platelet-shaped grains [16]. Liu et al [10] in the recent report about the study of hot-deformed Nd-Fe-B magnets prepared from melt-spun ribbons with different Nd contents also established a close correlation between Nd concentration in the grain boundary and the coercivity. They also pointed out that the improvement in coercivity can be achieved through modification of the grain boundary phase to be non-ferromagnetic.

The eutectic grain boundary diffusion process (GBDP) was first introduced by Sepehri-Amin et al. [17], applied to hydrogen-disproportionation-decomposition-recombination processed Nd-Fe-B magnet powder using the low melting temperature $Nd_{70}Cu_{30}$ eutectic alloy. This process was later on applied to hot-deformed magnets with 1 mm thickness [18]. These practices have demonstrated drastic coercivity enhancement can be achieved by the eutectic GBDP with infiltration of $Nd_{70}Cu_{30}$ alloy. The mechanism of coercivity enhancement has been addressed as the formation of Nd-rich intergranular phase during the solidification

process. More efforts were put in extending the Nd-Cu eutectic GBDP to bulk hot-deformed magnets while applying the expansion constraint along the easy-axis direction. A balanced combination of coercivity (1.9 T) and remanence (1.35 T) was attained from this attempt [19]. However, a higher level of coercivity of 2.5 T is required for automotive traction motor applications.

From the existing phase diagrams, it can be found neodymium has eutectic reactions with various types of Nd_xM_y compounds, where M includes Al, Cu, Ga, Zn, Mn, Co, Ni and Fe. However, by now only a few eutectic systems, Nd-Cu and Pr-Cu, were explored for the eutectic grain boundary diffusion process [18, 20]. Previous studies [21, 22] suggested that the addition of Al and Ga improve the wettability between $Nd_2Fe_{14}B$ and intergranular phases, which may smoothen the intergranular phase for better separation of $Nd_2Fe_{14}B$ grains. With partial substitution of Al for Fe [23], $Nd_2Fe_{14-x}Al_xB$ compounds are known to exhibit higher anisotropy field accompanied by the reduction in magnetization.

In order to explore for the most ideal diffusion source among various Nd-M systems that is capable of giving the most effective coercivity enhancement, we employed various eutectic alloys as the diffusion source for the eutectic grain boundary diffusion process to hot-deformed Nd-Fe-B magnets. The mechanism of the coercivity enhancement of hot-deformed magnets is discussed on the basis of detailed microstructure characterizations by scanning electron microscopy (SEM) and transmission electron microscopy (TEM).

3.2 Experimental

Hot-deformed magnets in 4×4×2 mm^3 size, 2 mm is the easy axis direction, with the composition of $Nd_{13.2}Fe_{76}Co_{5.6}B_{4.7}Ga_{0.5}$ (at.%) were used as the starting materials. The hot-deformation process was carried out at 780^oC. The diffusion sources were prepared by the Cu single-roller melt-spinning technique as the type of melt-spun ribbons of various Nd-rich eutectic alloys. In this work, the Nd-TM alloys were chosen as $Nd_{90}Al_{10}$, $Nd_{82}Al_{18}$, $Nd_{80}Ga_{20}$, $Nd_{70}Cu_{30}$, $Nd_{75}Zn_{25}$, $Nd_{50}Pr_{20}Cu_{30}$ and $Nd_{60}Al_{30}Cu_{10}$ alloys. The diffusion process was carried out by wrapping the hot-deformed magnets together with eutectic alloy ribbons in Nb foils, followed by annealing at proper temperatures for 1h under vacuum in 10^{-3} Pa. The heat treatment temperature was designed with referring to eutectic transition point in the binary phase diagrams. In order to investigate the upper limit of the coercivity enhancement through the diffusion process, giant amount of diffusion sources was applied in this work, *i.e.*, no consideration was made for the loss of remanence.

Magnetic property measurement was performed with the superconducting quantum interface device vibrating sample magnetometer (SQUID-VSM) to the hot-deformed and the diffusion processed magnets. To attain the estimation of the overall or average magnetic properties of the diffusion-processed magnets, the specimen used for SQUID-VSM measurement was sliced along easy axis crossing sample surface and center. Demagnetization factor correction was made based on the equation of $H_{eff} = H_{ext} - N_dM$, where H_{eff} denotes as effective field, H_{ext} refers to external field, while N_d is the demagnetization factor which was calculated for the prism specimen configuration described in ref [24]. N_d falls into the range of 0~1; when the specimen approaches more to needle shape, N_d will be more close to 0. The microstructure characterization was carried out using Carl ZEISS CrossBeam 1540EsB with sample surfaces freshly polished with the built-in Focused

Ion Beam (FIB) prior to SEM observation. Scanning transmission electron microscopy energy-dispersive x-ray spectroscopy (STEM EDS) maps were constructed using Nd-L_α, Dy-M_α, Fe-K_α, Co-K_α and Cu-K_α spectrum. The TEM specimens were prepared with the lift-out method using a focused ion beam on FEI Nanolab Helios 650.

3.3 Results

Demagnetization curves of the initial hot-deformed and diffusion-processed magnets using various diffusion sources are displayed in Fig. 3-1(a). These are the second quadrant deduced from the hysteresis measurement. Remarkable coercivity ($\mu_0 H_c$) enhancement was observed by the diffusion process using $Nd_{90}Al_{10}$, $Nd_{82}Al_{18}$, $Nd_{80}Ga_{20}$, $Nd_{70}Cu_{30}$, $Nd_{75}Zn_{25}$, $Nd_{50}Pr_{20}Cu_{30}$ and $Nd_{60}Al_{30}Cu_{10}$ alloys as the diffusion sources. When the diffusion process was conducted under750°C for $Nd_{75}Mn_{25}$ and $Nd_{82}Al_{18}$ alloys, coercivity shows the degradation from the initial hot-deformed magnet because of grain coarsening. In all cases of the diffusion process, there existed a decrease of remanence ($\mu_0 M_r$) which is considered to be originated from the introduction Nd-rich intergranular phases into the magnet. The detailed discussion will be made in the coming sections.

The summarized magnetic properties by plotting the remanence and the coercivity of the diffusion-processed samples are shown in Fig. 3-1(b). This indicated the most effective coercivity enhancement was attained by the diffusion process using $Nd_{90}Al_{10}$ as diffusion source. After the diffusion process at 700°C for 1 h using $Nd_{90}Al_{10}$, coercivity increased from 1.3 T to 2.5 T, with the remanence decreases from 1.51 T to 1.21 T. On the other hand, $Nd_{70}Cu_{30}$ diffusion-processed magnet obtained the $\mu_0 H_c$ of 2.3 T by the diffusion process performed at 600°C. This low processing temperature for $Nd_{70}Cu_{30}$ compared to other alloys is due to the low Nd/NdCu eutectic temperature of 520°C.

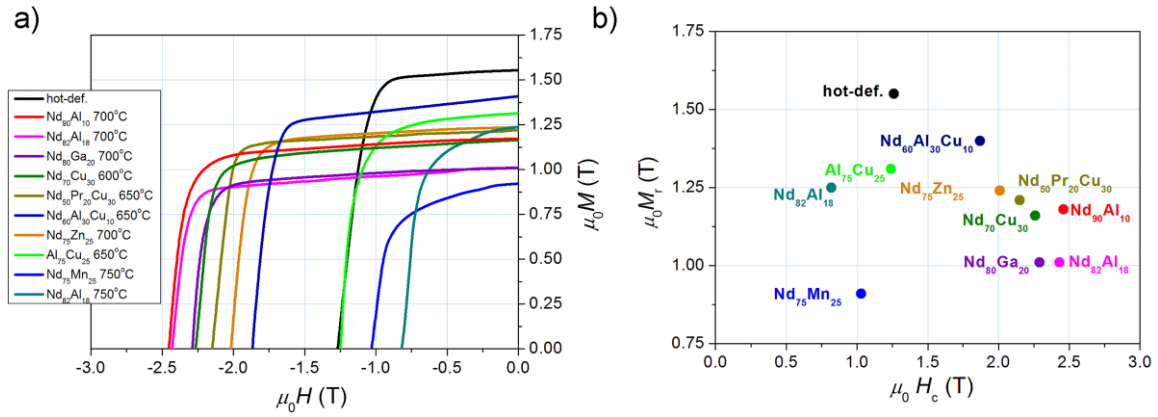

Fig. 3-1 (a) Demagnetization curves of the hot-deformed and diffusion-processed samples by various eutectic alloys, (b) remanence vs coercivity plot of the hot-deformed and the diffusion-processed samples.

The detailed comparison was taken between $Nd_{90}Al_{10}$ and $Nd_{70}Cu_{30}$ diffusion processed magnets. Fig. 3-2(a) presents the temperature dependence of the coercivities of the samples diffusion-processed with $Nd_{90}Al_{10}$ and $Nd_{70}Cu_{30}$. The $Nd_{90}Al_{10}$ diffusion-processed sample exhibits faster degradation in coercivity with increasing temperature compared to that of $Nd_{70}Cu_{30}$ diffusion-processed sample; as a result, $Nd_{90}Al_{10}$

diffusion-processed sample possesses lower coercivity of 0.6 T than that of the $Nd_{70}Cu_{30}$ diffusion-processed sample, 0.7 T, at 200°C. If the temperature dependent coercivity is simulated with the phenomenological micromagnetic equation, $H_c(T) = \alpha H_A(T) - N_{eff} M_s(T)$, as shown in Figure 3-2 (b), where $H_c(T)$ is experimentally measured temperature dependent coercivity, and $M_s(T)$ and $H_a(T)$ are the temperature dependent magnetization and anisotropy field for $Nd_2Fe_{14}B$ taken from ref [25]. $H_c(T)/M_s(T)$ shows a near linear correlation against $H_A(T)/M_s(T)$ with α as the slope, N_{eff} as the intercept with the longitudinal axes. From previous study, the structural parameter α is used as the indicator of defect regions at grain boundaries as well as grain misalignment. On the other hand, N_{eff}, known as effective demagnetization factor reflects local demagnetizing filed which is related with the grain size, geometry as well as grain size distribution [25]. With a linear fit of H_c/M_s vs. H_A/M_s plot, one can derive α values for $Nd_{90}Al_{10}$ and $Nd_{70}Cu_{30}$ diffusion processed samples as 0.79 and 0.61, respectively, which shows an obvious increment from 0.34 of the hot-deformed magnet. This can be the indication of reduced defect regions with the formation of Nd-rich intergranular phases. However, N_{eff} values increase from 0.79 to 1.47 and 0.94 for $Nd_{90}Al_{10}$ and $Nd_{70}Cu_{30}$ diffusion-processed samples, respectively. The larger N_{eff} for the $Nd_{90}Al_{10}$ diffusion processed sample is due the larger grain size because the processing temperature for $Nd_{90}Al_{10}$ is 100°C higher than that for $Nd_{70}Cu_{30}$.

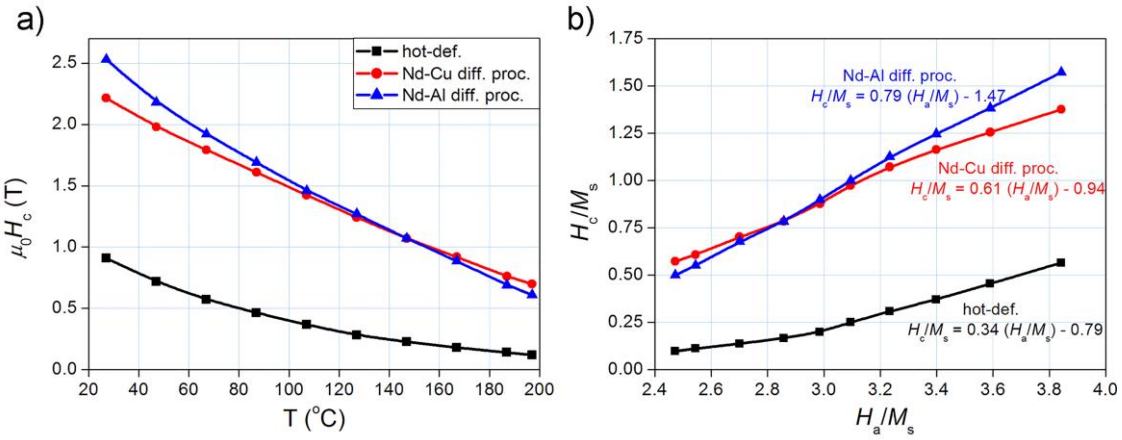

Fig. 3-2 (a) Temperature dependence of coercivity of the hot-deformed, Nd-Al and Nd-Cu diffusion-processed samples, (b) dependence of H_c/M_s on H_a/M_s of the hot-deformed, Nd-Al and Nd-Cu diffusion-processed samples. Micromagnetic parameters α and N_{eff} are calculated from the slope and intercept of the linear fit of these plots, respectively.

The backscattered electron (BSE) SEM observations have been carried out for the hot-deformed and $Nd_{90}Al_{10}$ diffusion-processed magnets from the transverse cross-sections (Fig. 3 (a, b)) and the top surfaces with c-axis out-of-plane (Fig. 3(d, e)). The images show the formation of Nd-rich intergranular phase between $Nd_2Fe_{14}B$ grains in the $Nd_{90}Al_{10}$ diffusion-processed magnet. The calculated areal fraction based on the different contrast of the intergranular phase from the matrix phase, increased from 3 % of the initial hot-deformed sample to 27 % of the diffusion processed sample. The formation of Nd-rich intergranular phase shows a preferential distribution along the flat surfaces of $Nd_2Fe_{14}B$ grains rather than side surfaces, which also provides the explanation of the observed significant uniaxial expansion of the diffusion processed magnets along the easy axis. While along other directions, the change in dimensions is almost negligible.

With this large volume fraction of Nd-rich intergranular phase, the $Nd_2Fe_{14}B$ grains are expected to be well magnetically isolated. We can also note there are two types of contrasts in the intergranular phase; one with a relatively bright contrast and the other has a dim contrast, suggesting non-uniform distributions of Co and Ga for which will be described later. The average grain size of the hot-deformed magnet is evaluated to be ~282±94 nm in width and ~72±22 nm in thickness. The grain size increased to ~299±138 and ~100±66nm respectively for the $Nd_{90}Al_{10}$ diffusion-processed sample. We can see the $Nd_{90}Al_{10}$ diffusion-processed sample demonstrated a comparable mean grain size as the initial hot-deformed sample, while the large standard deviation was seen for $Nd_{90}Al_{10}$ infiltrated sample. This implies a much larger grain size which is caused by the high annealing temperature, in this case, 700^{o}C, of the $Nd_{90}Al_{10}$ diffusion-process. The observation of abnormally grown grains in the $Nd_{90}Al_{10}$ diffusion-processed sample could also been directly confirmed from the BSE SEM images (as those grains indicated by the red arrows in Fig.3b and d). This was not reported in the $Nd_{70}Cu_{30}$ diffusion-processed sample [18].

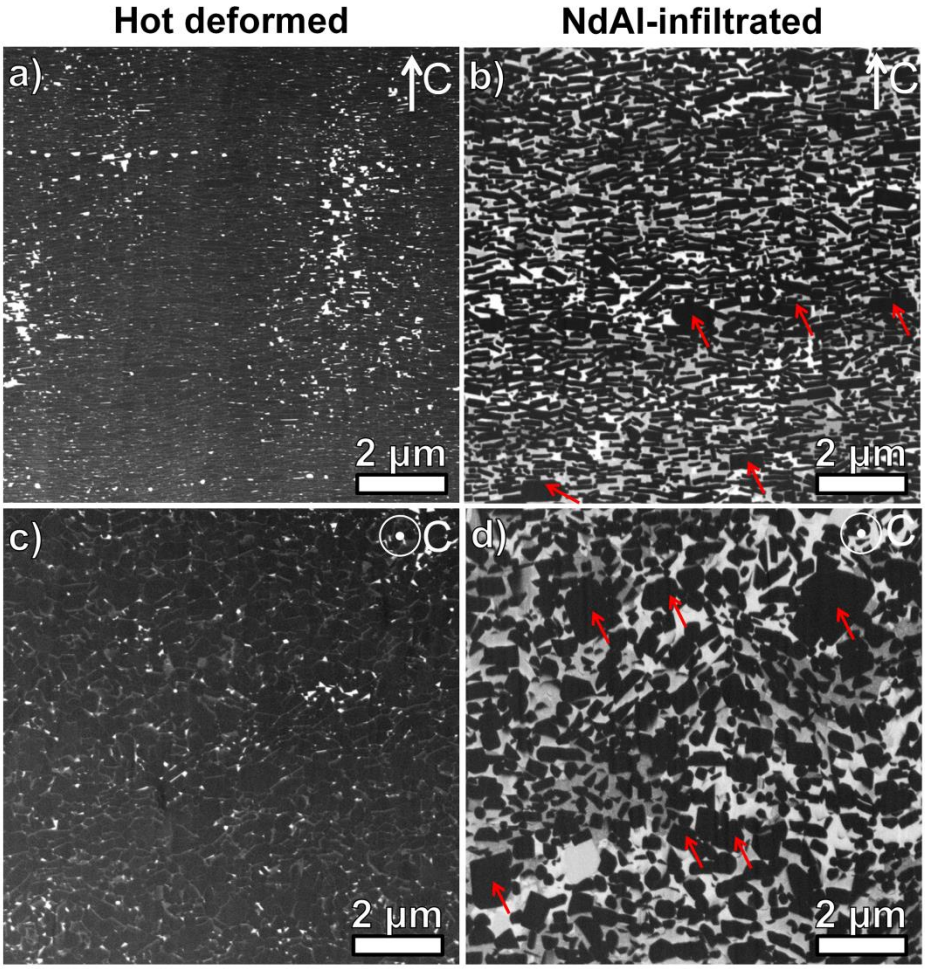

Fig. 3-3 BSE-SEM images of the hot-deformed (a,c) and the $Nd_{90}Al_{10}$ diffusion-processed (b,d) samples. The observation direction is along the easy-axis lying in-plane (a,b) and out-of-plane in (c,d).

Bright field (BF) transmission microscopy (TEM) and Lorentz TEM images of the hot-deformed and $Nd_{90}Al_{10}$ diffusion-processed samples are shown in Fig. 3-4. Large amount of wavy-patterned strain-induced fringes are observed in the $Nd_{90}Al_{10}$ diffusion-processed sample (Fig. 3-4(b)), which are not evident in the initial hot-deformed sample. This is believed to originate from the lattice mismatch between the main phase and the crystalline Nd-rich intergranular phase. The over-focused Lorentz-TEM images show domain walls in bright and dark contrasts. The domain wall appears to be continuous across the grain boundaries parallel to the broad surface of the platelet-like grains in the initial hot-deformed sample (Fig. 3-4(c)). On the other hand, the domain walls are interrupted in the intergranular phase in the $Nd_{90}Al_{10}$ diffusion-processed sample (Fig. 3-4(d)), suggesting the grain boundary phase is non-ferromagnetic after the diffusion process. In spite of the exchange decoupling of the grains, the domain walls lie linearly because of the magnetostatic interaction among the grains.

STEM-EDS maps of the hot-deformed and $Nd_{90}Al_{10}$ diffusion-processed samples are shown in Fig. 3-5(a) and (b), respectively, with c-axis in-plane. In the initial hot-deformed sample, Nd-rich intergranular phase is not clearly visible. In most cases, $Nd_2Fe_{14}B$ grains are in direct contact with each other; Co shows uniform

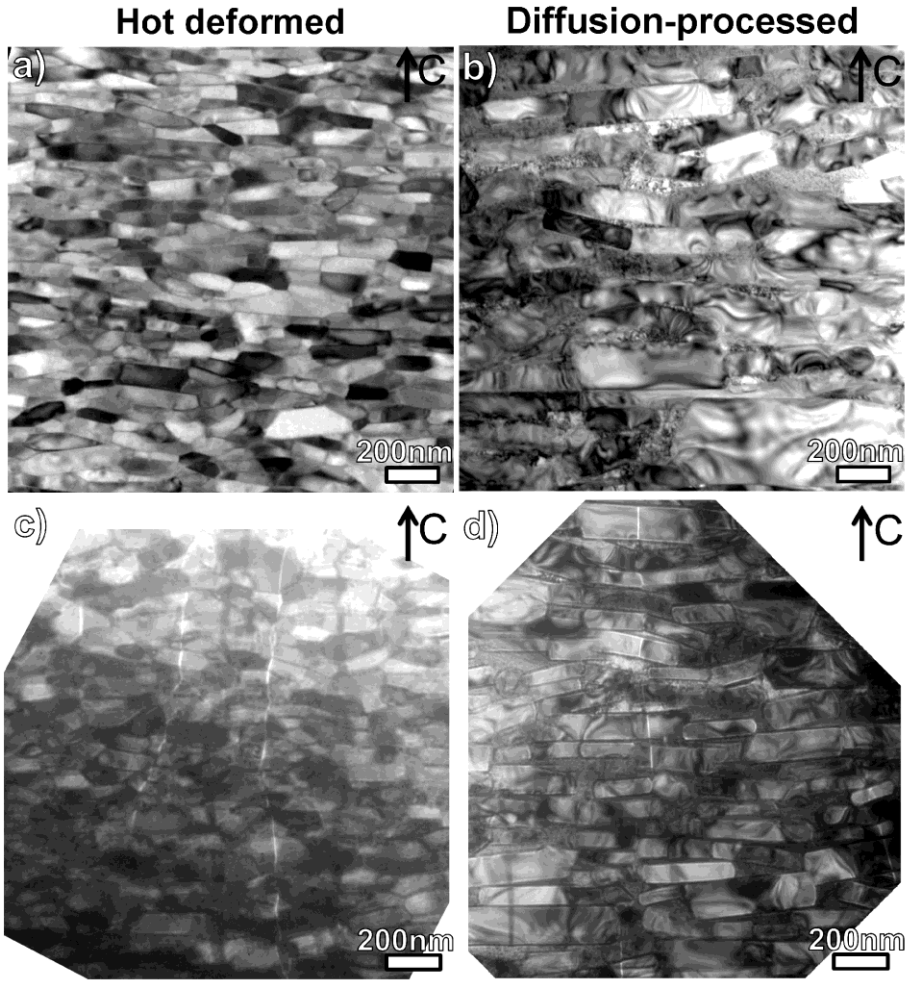

Fig. 3-4 BF-TEM images and Lorentz TEM images of the hot-deformed (a,c) and the $Nd_{90}Al_{10}$ diffusion-processed (b,d) samples. The observation direction is along the easy-axis lying in-plane.

distribution while Ga appears to be enriched in the intergranular phase. In the $Nd_{90}Al_{10}$ diffusion processed sample, Fig. 3-5(b), thick Nd-rich intergranular phase forms parallel to the flat surface of the platelet-shaped $Nd_2Fe_{14}B$ grains. Thinner Nd-rich intergranular phase is observed at the side boundaries; however, many platelet grains appear to be interconnected in the longitudinal direction. Two types of contrasts are observed in the Co, Ga and Al maps, indicating the Nd-rich intergranular phase is separated into two phases, i.e., (Nd,Co)-rich and Nd(Ga,Al)-rich phases.

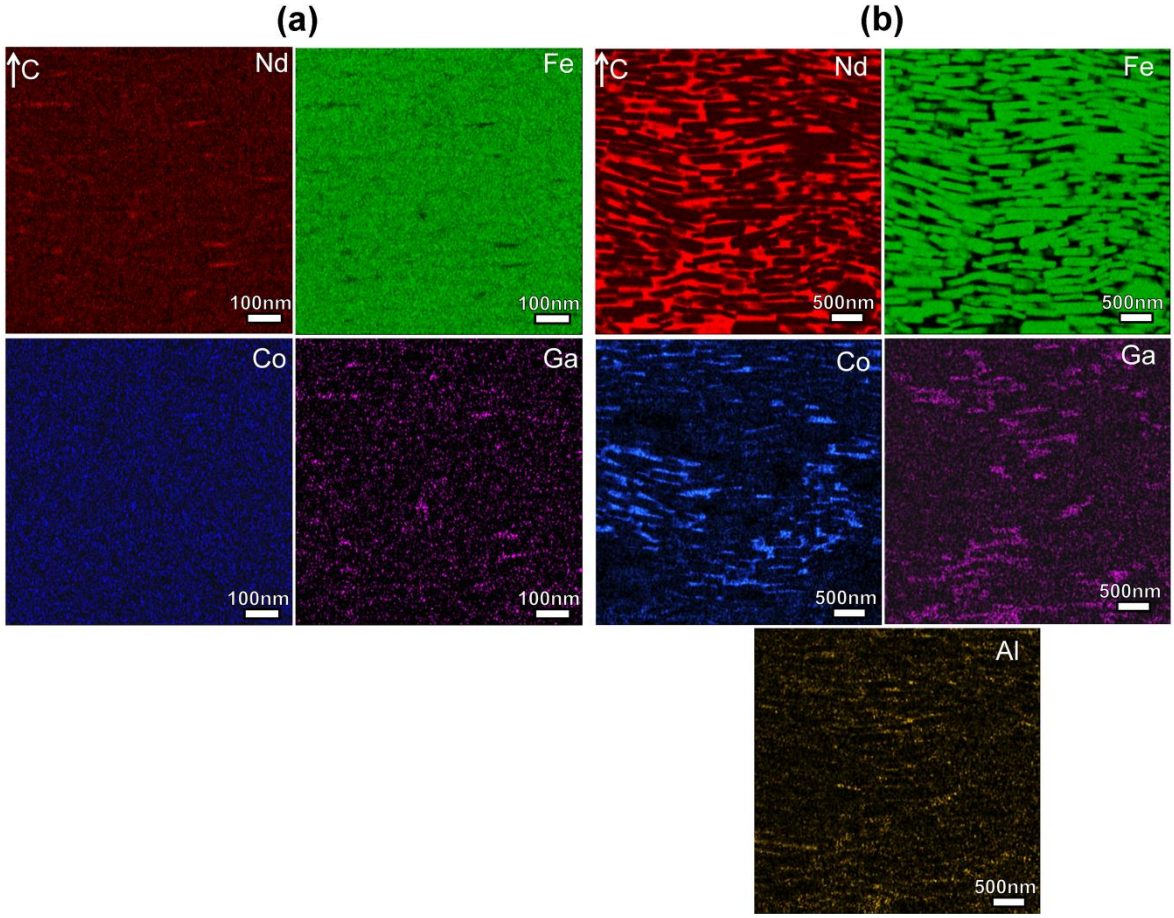

Fig. 3-5 TEM-EDS elemental mapping images of the hot-deformed (a) and the NdAl-infiltrated (b) samples with c-axis in-plane upward. The selected analysis peaks for the elemental maps are Nd *Lα*, Fe *Kα*, Co *Kα*, Ga *Kα* and Al *Kα*.

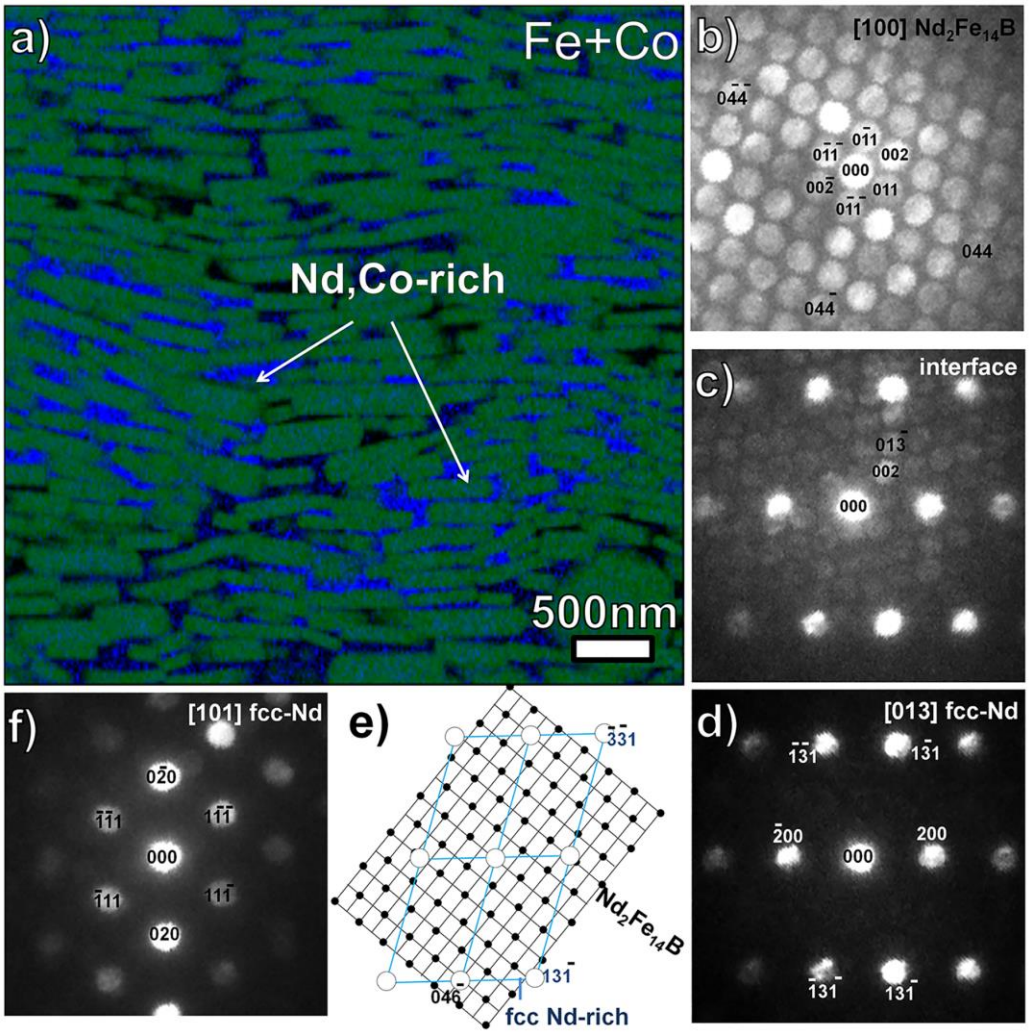

Fig. 3-6 (a) STEM-EDS elemental mapping images of Fe overlapped with Co maps of NdAl-infiltrated sample. The selected analysis peaks for the elemental maps are Fe *Kα*, and Co *Kα*. (b-d) NBED patterns taken from $Nd_2Fe_{14}B$ phase, interface and intergranular Nd-rich regions, respectively; (e) schematic models of the crystallographic ORs between $Nd_2Fe_{14}B$ phase and the Nd-rich phase; (f) NBED pattern taken from another intergranular Nd-rich grain.

The chemical composition and the crystal structure of these two different types of Nd-rich phases were examined by localized STEM-EDS quantification and nanobeam electron diffraction (NBED). Fig. 3-6(a) shows a superimposed elemental map of Nd and Co for visualizing the distribution of the (Nd,Co)-rich phase. The diffraction pattern shown in Fig. 3-6(b) is taken from the $Nd_2Fe_{14}B$ grain in the [100] zone axis. Fig. 6(d) shows the NBED pattern taken from the Nd-rich phase, which can be indexed as an fcc structure in the [013] zone axis. The lattice constant of this type of Nd-rich phase was calculated to be ~0.54 nm, which is consistent with the fcc Nd-rich phase reported in sintered Nd-Fe-B magnets [26, 27]. From the NBED pattern taken from the interface region of $Nd_2Fe_{14}B$ phase and the Nd-rich intergranular region, the crystallographic orientation relationship (OR) can be identified to be $[100]Nd_2Fe_{14}B//[013]$fcc-Nd, $(0\bar{4}6)Nd_2Fe_{14}B//(1\bar{3}1)$fcc-Nd. The localized EDS quantification suggests that the composition of the Nd-rich intergranular phase is ~$Nd_{79}Co_{14}Fe_6Al_1$ (at.%).

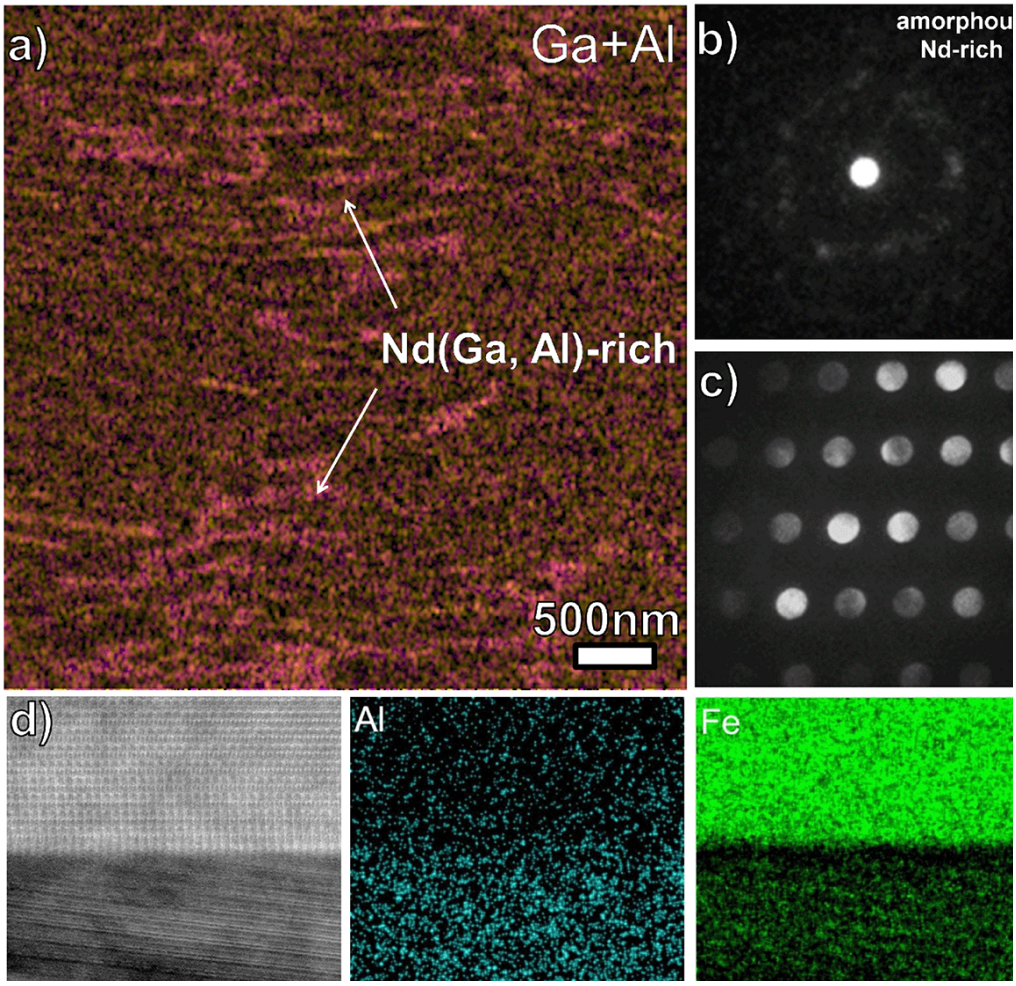

Fig. 3-7 (a) STEM-EDS elemental mapping images of Ga overlapped with Al maps of NdAl-infiltrated sample. The selected analysis peaks for the elemental maps are Fe *Kα*, and Co *Kα*. (b,c) NBED patterns taken from amorphous and $Nd(Fe,Al)_2$ intergranular Nd-rich regions, respectively; (d) STEM-HAADF image and EDS maps taken from the $Nd(Fe,Al)_2$ phase.

The chemical composition of Nd(Ga,Al)-rich regions shown in Fig. 3-7(a) shows the chemical composition is about ~$Nd_{62}Co_{22}Fe_8Al_8$ (at.%) with the amorphous structure (Fig. 3-7(b)). A layered contrast is seen in the HAADF-STEM image (Fig.3-7(d)), which comes from the periodical atomic layer stacking of the newly-formed phase, which has the composition of close to $Nd(Fe,Al)_2$ and the diffraction pattern of this phase is shown in Fig. 3-7(b). The lattice fringe shows a periodicity of 1.2 nm and calculated d-spacings are 3.4 nm and 4.2 nm, respectively. Fidler et al. [28-30] referred this phase as al2 or δ phase that was first found in Al_2O_3-doped sintered magnets and they pointed out that this phase has a complex tetragonal structure. They also suggested that the al2 phase has a large anisotropy field and good wettability with $Nd_2Fe_{14}B$ grains, which was attributed to the high coercivity of Al-doped or Al_2O_3-doped sintered magnets.

As side grain boundary also plays vital role in magnetic isolation, we took a close characterization for side grain boundary, as shown in Fig. 3-8. Similar enrichment of Nd, Ga, and Al were observed in the intergranular phase that located on a/b plane grain boundary when two facets are most reaching to each other. At the interface between the grain boundary phase and the $Nd_2Fe_{14}B$ phase, segregation of Al with the

concentration of around 7.5 at.% can be observed. Take a quantification analysis to the inner region of the main phase, pronounced Al peak at the Al K_α spectrum is detected, indicating the diffusion of Al into the matrix phase at the heat treatment at 700°C. The Nd concentration of the intergranular phase is close to 80 at. % with less than 10 at.% Fe, suggesting the intergranular region is non-ferromagnetic.

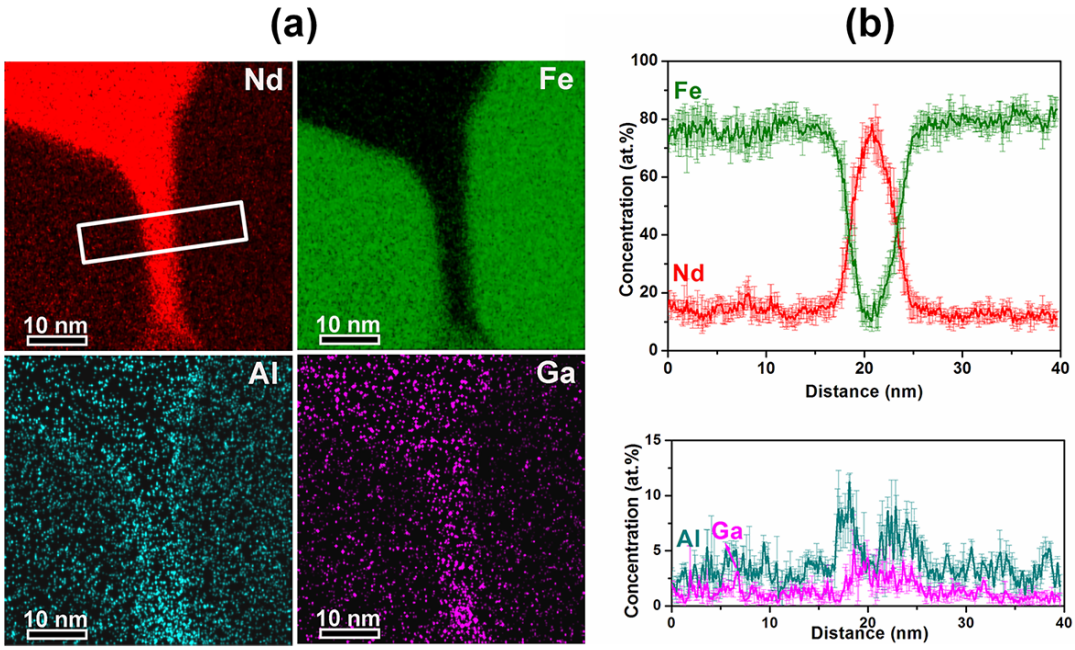

Fig. 3-8 (a) STEM-EDS elemental mapping images and (b) line-scan profile of the Nd-rich intergranular phase perpendicular to the flat surface of the $Nd_2Fe_{14}B$ grains.

3.4 Discussion

This work has shown that the coercivity of hot-deformed magnets can be substantially enhanced by the grain boundary diffusion process using various RE-TM eutectic alloys as diffusion sources. Note that the coercivity of hot-deformed magnets is degraded if the diffusion-process is applied above the temperature for the hot-deformation process. In fact, the hot-deformed magnets processed at 750°C using $Nd_{75}Mn_{25}$ and $Nd_{82}Al_{18}$ alloys did not show any improvement in coercivity because of abnormal grain growth at this high processing temperature.

The enhancement of the coercivity is mainly attributed to the exchange decoupling of the $Nd_2Fe_{14}B$ grains as a result of the formation of Nd-rich intergranular phase by the infiltration of eutectic melts. This is evidenced from the microstructural characterizations by SEM and TEM. The concentration of Fe in the intergranular phase is much decreased after the diffusion process, indicating that the ferromagnetism in the grain boundary phase is diluted by the infiltration of the RE-TM eutectic alloy. Nearly complete magnetic isolation has been realized by the diffusion process when $Nd_{90}Al_{10}$ alloy is used as the diffusion source. The micromagnetic parameters α in $H_c(T) = \alpha H_A(T) - N_{eff}M_s(T)$ was improved for $Nd_{90}Al_{10}$ and $Nd_{70}Cu_{30}$ diffusion-processed samples. Improved α suggests that the defect density at the interface that cause reduction of anisotropy field is reduced by diffusion of Nd-Cu and Nd-Al alloys. The $Nd_{90}Al_{10}$ diffusion processed

sample has a slightly larger α value than that of $Nd_{70}Cu_{30}$ diffusion processed sample. This can originate from segregation of Al at the interface of Nd-rich phases/$Nd_2Fe_{14}B$ grains as shown in Fig. 3-8 that may recover the reduced local anisotropy field at the surface of $Nd_2Fe_{14}B$ grains. Also, the Al substitution for Fe atoms is expected to increase anisotropy field of the $Nd_2Fe_{14}B$ phase [23]. The formation of the al2 phase in the grain boundary may also have a similar effect. These factors could contribute to the high coercivity of $Nd_{90}Al_{10}$ diffusion-processed sample at room temperature.

The larger N_{eff} value of $Nd_{90}Al_{10}$ diffusion-processed sample is considered to be due to the dispersed grain size distribution after the high processing temperature required for the $Nd_{90}Al_{10}$ infiltration. Non-uniform grain size distribution leads to poorer thermal stability as a result of the non-uniform nucleation of reversed magnetic domains due to the larger stray field from those abnormally grown grains [31]. In addition, enrichment of 3 at.% Al in the $Nd_2Fe_{14}B$ phase can reduces the Curie temperature of $Nd_2Fe_{14}B$ phase which can be an additional reason for the poorer thermal stability of coercivity in $Nd_{90}Al_{10}$ diffusion-processed sample compared with that of $Nd_{70}Cu_{30}$ diffusion-processed sample.

The coercivity of $Nd_{70}Cu_{30}$ diffusion-processed sample at 200°C (typical operation temperature of traction motors of hybrid vehicles) is 0.7 T, which is close to 0.8 T of the currently used $(Nd_{0.7}Dy_{0.3})_2Fe_{14}B$ sintered magnets. With the development of cooling technique in traction motors, the application of the Nd-Cu diffusion-processed magnets may become practical in the near future.

The remaining issue of the eutectic diffusion process is the optimization of the thickness of the intergranular phase, especially those located parallel to the broad surface of the platelet-shaped $Nd_2Fe_{14}B$ grains. As seen in Fig. 3-1, large coercivity enhancement was achieved at the expense of remanence because of the large volume fraction of non-ferromagnetic intergranular phase. In order to keep the remanence high, a smaller amount of diffusion source should be infiltrated. For this purpose, the usage of diffusion sources with higher diffusivity with lower melting-point may be effective. The diffusion process using lower melting temperature alloys will also be beneficial in optimizing the grain size distribution of the diffusion-processed magnets since grain coarsening during the eutectic diffusion process is detrimental for the thermal stability of the hot-deformed magnets.

3.5 Conclusion

This chapter studied the coercivity enhancement of hot-deformed Nd-Fe-B magnets by the eutectic GBDP using various eutectic alloys. The detailed investigation was carried out on Nd-Al diffusion-processed sample in comparison with Nd-Cu diffusion-processed sample in previous report [18].

The major conclusions of this chapter are listed as below,

(1) Coercivity improvement has been realized for hot-deformed Nd-Fe-B magnets using Nd-Al, Nd-Cu, Nd-Zn, Nd-Ga, Nd-Cu-Al and Nd-Pr-Cu eutectic alloys as diffusion sources.

(2) At room temperature, the sample diffusion processed at 700°C using $Nd_{90}Al_{10}$ shows the highest coercivity of 2.5 T. However, it exhibits pronounced degradation of coercivity with increasing temperature compared to the sample diffusion-processed with $Nd_{70}Cu_{30}$. Thus, at 200°C, $Nd_{70}Cu_{30}$ diffusion-processed

sample possesses the highest coercivity of 0.7 T, indicating that Nd-Cu alloy is still the most promising diffusion source for the eutectic grain boundary diffusion process.

(3) Co-enriched Nd-rich phase was determined to be an fcc phase which has a good crystallographic match with the $Nd_2Fe_{14}B$ phase. An Al-containing phase (al2) was observed in the $Nd_{90}Al_{10}$ diffusion-processed sample with the composition of $Nd(Fe,Al)_2$ and a tetragonal structure.

(4) The champion magnetic property was realized with $Nd_{90}Al_{10}$ as diffusion source which shows higher melting-point than that of $Nd_{70}Cu_{30}$ alloy based on the binary phase diagram. This indeed indicates us searching for the most ideal diffusion source is not simply the journey of seeking for the low melt-point compound. Changes of wettability of the intergranular phases can be expected, sometimes only with very little variation in the composition or their crystal structures.

References

[1] R. W. Lee, "Hot-pressed neodymium-iron-boron magnets," *Appl. Phys. Lett.*, vol. 46, no. 8, pp. 790-791, Apr. 1985.

[2] R. K. Mishra, T. Y. Chu, and L. K. Rabenberg, "The development of the microstructure of die-upset Nd-Fe-B magnets," *J. Magn. Magn. Mater.*, vol. 84, no. 1, pp. 88-94, Feb. 1990.

[3] W. Grünberger, D. Hinz, A. Kirchner, and K.-H. Müller, L. Schultz, "Hot deformation of nanocrystalline Nd-Fe-B alloys," *IEEE Trans. Magn.*, vol. 257, no. 1-2, pp. 293-301, Jul. 1997.

[4] R. W. Lee, E. G. Brewer, and N. A. Schaffel, "Processing of neodymium-iron-boron melt-spun ribbons to fully dense magnets," *IEEE Trans. Magn.*, vol. 21, no. 5, pp. 1958-1963. Sep. 1985.

[5] R. K. Mishra, and R. W. Lee, "Microstructure, domain walls, and magnetization reversal in hot-pressed Nd-Fe-B magnets," *Appl. Phys. Lett.*, vol. 48, no. 11, pp. 733-735, Mar. 1986.

[6] P. Tenaud, A. Chamberod, and F. Vanoni, "Texture in Nd-Fe-B magnets analysed on the basis of the determination of $Nd_2Fe_{14}B$ single crystals easy growth axis," *Solid State Commun.*, vol. 63, no. 4, pp. 303-305, Jul. 1987.

[7] M. Leonowicz, and H. A. Davies, "Effect of Nd content on induced anisotropy in hot deformed Fe-Nd-B magnets," *Mat. Lett.*, vol. 19, no. 5-6, pp. 275-279, May. 1994.

[8] L. Li, D. E. Luzzi, and C. D. Graham, "High-resolution electron microscope study of the grain boundary phase in rapidly quenched Nd-Fe-B permanent magnet alloys," *J. Matter. Eng. Perform.*, vol. 1, no. 2, pp. 205-209, Mar. 1992.

[9] W. F. Li, T. Ohkubo, K. Hono, "Effect of post-sinter annealing on the coercivity and microstructure of Nd-Fe-B permanent magnets," *Acta Mater.*, vol. 57, no. 5, pp. 1337-1346, Mar. 2009.

[10] J. Liu, H. Sepehri-Amin, T. Ohkubo, K. Hioki, A. Hattori, T. Schrefl, and K. Hono, "Effect of Nd content on the microstructure and coercivity of hot-deformed Nd-Fe-B permanent magnets," *Acta Mater.*, vol. 61, no. 14, pp. 5387-5399, Aug. 2013.

[11] S. Sawatzki, I. Dirba, H. wendrock, L. Schultz, and O. Gutfleisch, "Diffusion processes in hot-deformed Nd-Fe-B magnets with DyF_3 additions," *J. Magn. Magn. Mat.*, vol. 358-359, pp. 163-169, may. 2014.

[12] N. Watanabe, M. Itakura, M. Nishida, "Microstructure of high coercivity Nd-Fe-Co-Ga-B hot-deformed magnet improved by the Dy diffusion treatment," *J. Alloy. Compd.*, vol. 557, pp. 1-4, Apr. 2013.

[13] L. H. Lewis, Y. Zhu, and D. O. Welch, "Evidence for reversal by nucleation in RE-Fe-B die-upset magnets," *J. Appl. Phys.*, vo. 76, no. 10, pp. 6235-6237, Nov. 1994.

[14] L. H. Lewis, Y. M. Zhu, and D. O. Welch, "Ferromagnetic grain boundary signature in die-upset RE-Fe-B magnets," *Scipta Metall. Mater.*, vol. 33, no. 10, pp. 1775-1780, Dec. 1995.

[15] T. D. Nguyen, K. M. Krishnan, L. H. Lewis, Y. Zhu, and D. O. Welch, "Microstructure and composition in rapidly quenched Nd-Fe-B hard magnet alloys," *J. Appl. Phys.*, vol. 79, no. 8, pp. 4848-4850, Apr. 1996.

[16] L. H. Lewis, T. R. Thurston, V. Panchanathan, U. Wildgruber, and D. O. Welch, "Spatial texture distribution in thermodynamically deformed 2-14-1-based magnets," *J. Appl. Phys.*, vol. 82, no. 7, pp. 3430-3441, Oct. 1997.

[17] H. Sepehri-Amin, T. Ohkubo, T. Nishiuchi, S. Hirosawa, and K. Hono, "Coercivity emhancement of hydrogenation-disproportionation-desorption-recombination processed Nd-Fe-B powders by the diffusion of Nd-Cu eutectic alloys," *Scripta Mater.*, vol. 63, no. 11, pp. 1124-1127, Nov. 2010.

[18] H. Sepehri-Amin, T. Ohkubo, S. Nagashima, M. Yano, T. Shoji, A. Kato, T. Schrefl, and K. Hono, "High-coercivity ultrafine-grained anisotropic Nd-Fe-B magnets processed by hot deformation and the Nd-Cu grain boundary diffusion process," *Acta Mater.*, vol. 61, no. 17, pp. 6622-6634, Oct. 2013.

[19] T. Akiya, J. Liu, H. Sepehri-Amin, T. Ohkubo, K. Hioki, A. Hattori, and K. Hono, "High-coercivity hot-deformed Nd-FeB permanent magnets processed by Nd-Cu eutectic diffusion under expansion constraint," *Scripta Mater.*, vol. 81, pp. 48-51, Jun. 2014.

[20] H.Sepehri-Amin, Lihua Liu, T. Ohkubo, M. Yano, T. Shoji, A. Kato, T. Schrefl, and K. Hono, "Microstructure and temperature dependent of coerciivty of hot-deformed Nd-Fe-B magnets diffusion processed with Pr-Cu alloy," *Acta Mater.*, vol. 99, pp. 297-306, Oct. 2015.

[21] K. G. Knoch, B. Grieb, E.-Th. Henig, H. Kronmüller, and G. Petzow, "Upgraded Nd-Fe-B-AD (AD = Al, Ga) magnets: wettability and microstructure," *IEEE Trans. Magn.*, vol. 26, no. 5, pp. 1951-1953, Sep. 1990.

[22] K. G. Knoch, E.-Th. Henig, and J. Fidler, "Correlation between Al addition and microstructural changes in Nd-Fe-B magnets," *J. Magn. Magn. Mater.*, vol. 83, no. 1, pp. 209-210, jan. 1990.

[23] W. Rodewald, and W. Fernengel, “Properties of sintered Nd-Fe-TM-B magnets,” *IEEE Trans. Magn.*, vol. 24, no. 2, pp. 1638-1643, Mar. 1988.

[24] A. Aharoni, “Demagnetization factors for rectangular ferromagnetic prisms,” *J. Appl. Phys.*, vol. 83, no. 6, pp. 3432-3434, Mar. 1998.

[25] H. Kronmüller, R. Fischer, M. Seeger, and A. Zern, “Mciromagnetism and microstructure of hard magnetic materials,” *J. Phys. D: Appl. Phys.*, vol. 29, no. 9, pp. 2274-2283, 1996.

[26]Y. Shinba, T. J. Konno, K. Ishikawa, K. Hiraga, and M. Sagawa, “Transmission electron microscopy study on Nd-rich phase and grain boundary structure of Nd-Fe-B sintered magnets,” *J. Appl. Phys.*, vol. 97, no. 5, pp. 053504, Feb. 2005.

[27] Q. Liu, F. Xu, J. Wang, X. Dong, L. Zhang, and J. Yang, “An investigation of the microstructure in the grain boundary region of Nd-Fe-B sintered magnet during post-sintering annealing,” *Scripta Mater.*, vo. 68, no. 9, pp. 687-690, May 2013.

[28] B. Grieb, E.–Th. Henig, G. Martinek, H. H. Stadelmaier, and G. Petzow, “Phase relations and magnetic properties of new phases in the Fe-Nd-Al and Fe-Nd-C systems and their influence on magnets,” *IEEE Trans. Magn.*, vol. 26, no. 5, pp. 1367-1369, Sep. 1990.

[29] J. Fidler, K. G. Knoch, H. Kronmüller, and G. Schneider, “Analytical TEM study of Al-doped, “two-phase” Nd-Fe-B sintered magnets,” *J. Mater. Res.*, vol. 4, no. 4, pp. 806-814, Aug. 1989.

[30] B. Grieb, K. G. Knoch, E. –Th. Henig, and G. Petzow, “Influence of Al-based additions on coercivity and microstructure in Fe-Nd-B magnets,” J. Magn. Magn. Mater., vol. 80, no. 1, pp. 75-79, Aug. 1989.

[31] H. Sepehri-Amin, T. Ohkubo, M. Gruber, T. Schrefl, and K. Hono, “Micromagnetic simulations on the grain size dependence of coercivity in anisotropic Nd-Fe-B sintered magnets,” Scripta Mater., vol. 89, pp. 29-32, Oct. 2014.

4 Chapter 4 Coercivity enhancement of hot-deformed Nd-Fe-B permanent magnets by the eutectic grain boundary diffusion process using Nd-Fe-Ga-Cu and Nd-Ga-Cu alloys as diffusion sources

4.1 Introduction

The coercivity enhancement of Nd-Fe-B hot-deformed magnets has been realized by the eutectic grain boundary diffusion process (GBDP) using various types of Nd_xM_y eutectic alloys as diffusion sources, where M includes Al, Cu, Ga, Zn, Mn, Co, Ni and Fe [1-3]. Formation of non-ferromagnetic Nd-rich intergranular phases in the infiltrated magnets leads to a remarkable enhancement in coercivity while also causes a large reduction in remanent magnetization. Figure 4-1 is a summarized magnetic property map comprised with remanent magnetization and coercivities of hot-deformed magnets diffusion-processed with various diffusion sources.

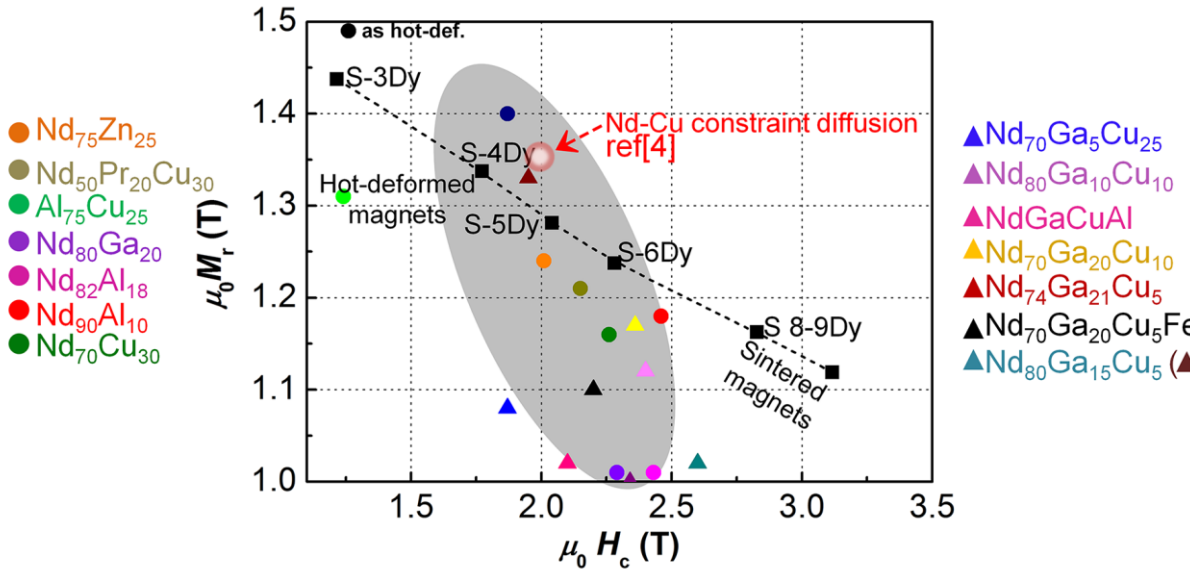

Fig. 4-1 Magnetic property map of the summarized data of hot-deformed magnets diffusion processed with various-types of diffusion sources. The dashed line is a plot of commercial sintered magnets with different Dy contents (manufactured with two-alloy method).

Akiya *et al*. [4] reported that one reason for the large remanence reduction is the degradation of [001] texture of $Nd_2Fe_{14}B$ grains, and proposed a way to overcome the issue by applying a constraint against volume expansion along the easy axis during the infiltration. However, the coercivity was limited below 2 T because of incomplete magnetic isolation with the Fe-rich intergranular phases that form along the side surface of the platelet-like grains.

We have been exploring for most ideal diffusion sources in order to achieve high coercivity without sacrificing remanence. Recently, Nakajima and Yamazaki reported a large coercivity enhancement in Ga-doped Nd-Fe-B sintered magnets from 1.0 T to 1.8 T by post-sinter annealing above 480°C [5], which is

significantly larger than that commonly observed in standard sintered magnets. Sasaki *et al*. [6] reported that the grains in the Ga-doped magnets are magnetically isolated by the non-ferromagnetic Nd-rich intergranular phase, whose rare earth (Nd and Pr) composition is about 90%. These investigations motivated us to explore the Nd-Ga-Cu based alloys as diffusion sources for the eutectic diffusion process on hot-deformed magnets.

4.2 Experimental procedure

Hot-deformed magnets with the nominal composition of $Nd_{13.2}Fe_{76}Co_{5.6}B_{4.7}Ga_{0.5}$ (at. %) in 5×5×4 mm^3 were used as starting samples. The direction along 4 mm was the easy axis. $Nd_{80}Ga_{15}Cu_5$ and $Nd_{62}Fe_{14}Ga_{20}Cu_4$ ribbons were prepared by the melt-spinning technique. The chemical composition of these alloys were selected based on STEM-EDS characterization results of the Ga-doped Nd-Fe-B sintered magnet [6].The hot-deformed magnets coated with Nd-Ga-Cu and Nd-Fe-Ga-Cu flakes respectively, were heat-treat at 600^{o}C for 3 h. Unlike the previous work, the eutectic diffusion process was applied without expansion constraint.

Hysteresis loops were measured with a super conducting quantum interface device vibrating sample magnetometer (SQUID-VSM). SEM observations were conducted using Carl ZEISS CrossBeam 1540EsB with surfaces polished by the built-in focused ion beam (FIB). Detailed characterizations were carried out by scanning transmission electron microscopy (STEM), with a probe aberration corrector, Titan 80-200. Scanning transmission electron microscopy energy-dispersive spectroscopy (STEM-EDS) maps were constructed using Nd-Lα, Fe-Kα, Co-Kα, Cu-Kα and Ga-Kα spectrum. TEM specimens were prepared by the lift-out technique on FEI Helios Nanolab 650.

4.3 Results

4.3.1 The fabrication of $Nd_{62}Fe_{14}Ga_{20}Cu_4$ alloy

a) Composition design

The composition of $Nd_{62}Fe_{14}Ga_{20}Cu_4$ at.% is calculated based on the nominal composition of the Ga-doped Nd-Fe-B sintered magnets in ref [6], which is $Fe_{77.1}Nd_{11.6}Pr_{3.7}B_{5.1}Cu_{0.1}Co_{1.0}Al_{0.9}Ga_{0.5}$ in at.%. Supposing Al and Co only exist in the $Nd_2Fe_{14}B$ phase, it is done by subtracting 88.6 % of matrix phase and 1.5 % of NdO_x (the percentage denotes the areal fraction of each phase based on SEM observations) from the nominal composition.

b) $Nd_{62}Fe_{14}Ga_{20}Cu_4$ ingot

The $Nd_{62}Fe_{14}Ga_{20}Cu_4$ ingot was prepared by induction-melting of the raw metals followed by casting into the plate-shaped steel mold. The chamber pressure is in ~10^{-4} Pa, on melting, the inert Ar pressure is 0.05 atmosphere pressure. The designed composition of the mother materials is $Nd_{65}Fe_{14}Ga_{20}Cu_4$ at.%. It is excessive in Nd by about 5 % to accommodate the loss in neodymium as a result of vaporization. Casting to the steel plate-shaped mold is for achieving relatively homogeneous elemental distribution with the help of rapid cooling on the steel mold. The BSE-SEM image and acquired EDS elemental maps of Nd, Fe and Cu from the same region of the as-cast ingot are shown in Figure 4-2. It shows a typical feature of solidification

geometry when the molten metal is cast into a cold metal mould. Such growth behavior is the selective growth as heat extracted from the mould as solute is partitioned into the liquid ahead of the solidification front.

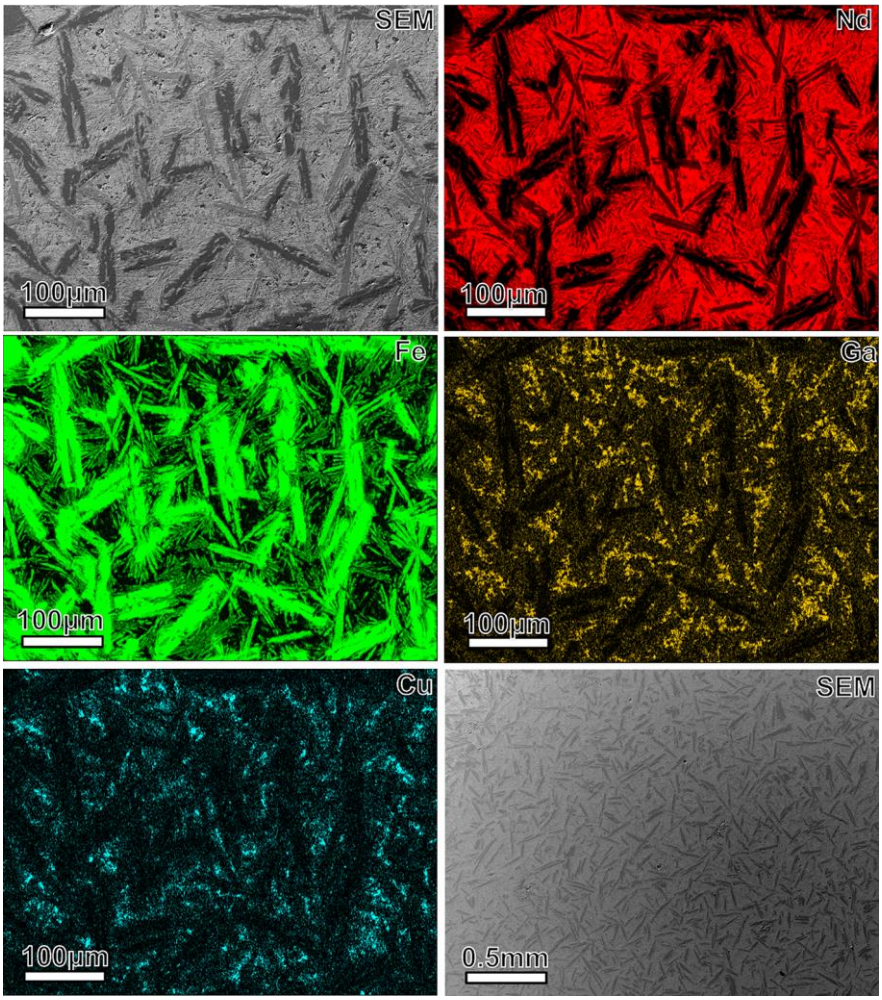

Fig. 4-2 BSE-SEM image and EDS elemental maps of Nd, Fe, Ga and Cu from the same region in the as-cast $Nd_{62}Fe_{14}Ga_{20}Cu_4$ ingot prepared by induction-melting with steel plate-mould.

c) Identification of phase

Further analysis of the as-cast Nd-Fe-Ga-Cu ingot was carried out by higher magnification EDS mapping, DTA and X-ray diffraction (XRD) in order to study the phase formed in this alloy system (as shown in Figure 4-3). As indicated by the superimposed EDS map showing the compositional analysis of the dendrites, the composition along the longitudinal direction of the dendrites is about 100 at.% Fe. The composition connected with the main branches of the dendrites is close to $Nd_6Fe_{13}Ga$ at.% which can also be confirmed from the XRD pattern (Figure 4-3(d)). Over the feather-like morphology bulky entities possessing rough peripheries have the composition of $Nd_{70}Cu_{30}$, Nd, and $Nd_{67}Ga_{28}Cu_5$, respectively. From the heating curve of DTA, four endothermic peaks can be observed at 475°C, 560°C, 640°C and 740°C.

At this stage of this work, it remains unclear the specific phase corresponding to each phase transition point. It is believed that the $Nd_{62}Fe_{14}Ga_{20}Cu_5$ applied as the diffusion source in this work is an alloy system instead of a simple compound.

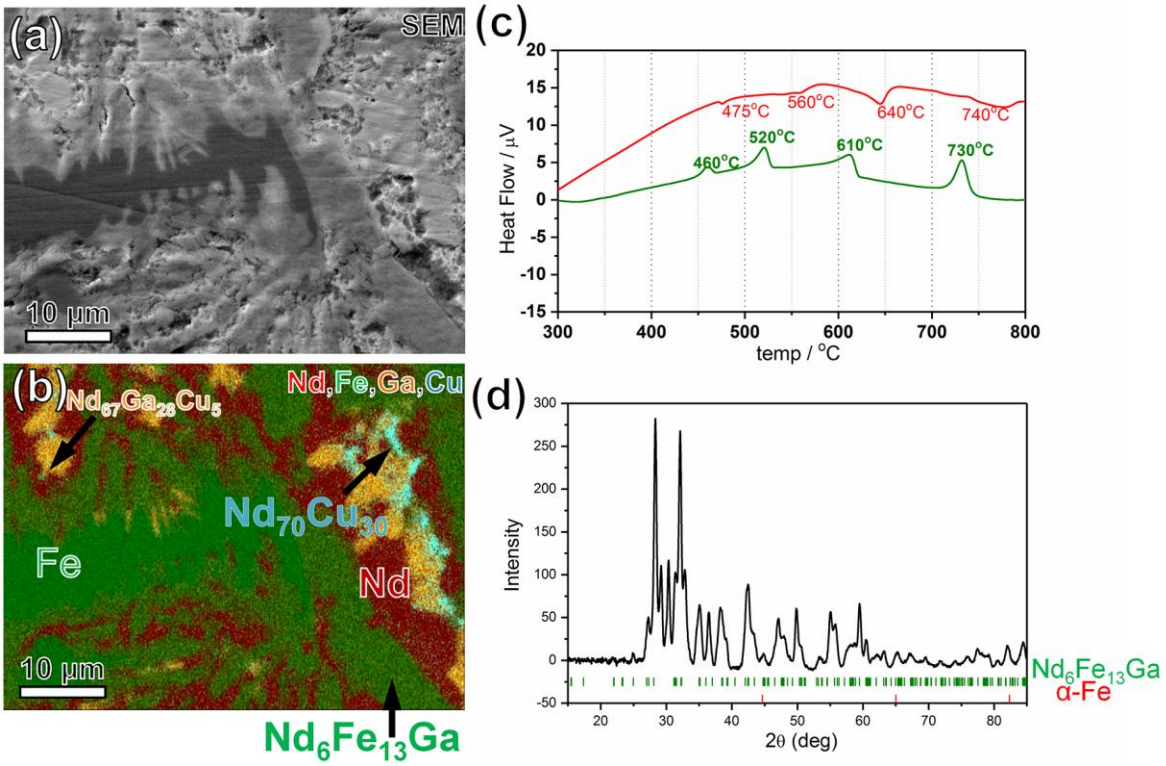

Fig. 4-3 (a) BSE-SEM image and (b) the superimposed EDS elemental maps of Nd, Fe, Ga and Cu from the same region in $Nd_{62}Fe_{14}Ga_{20}Cu_4$ ingot; (c) DTA heating (in red) and cooling (in green) curves and (d) XRD 2θ scan profile of $Nd_{62}Fe_{14}Ga_{20}Cu_4$ ingot.

4.3.2 Melting point of $Nd_{80}Ga_{15}Cu_5$ alloy

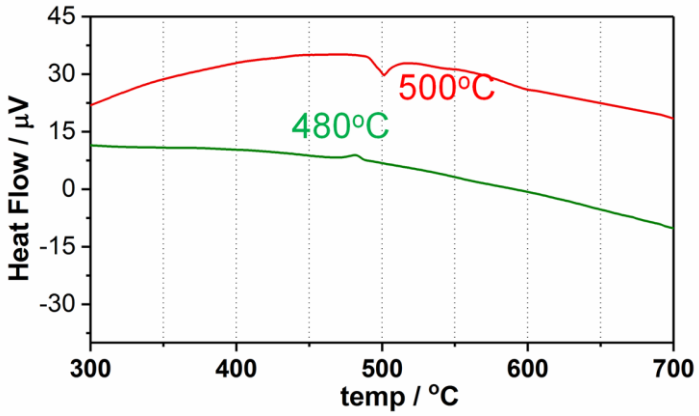

Fig. 4-4 DTA profile of $Nd_{80}Ga_{15}Cu_5$ alloy; heating curve is displayed in red and cooling curve in green.

The melting point of $Nd_{80}Ga_{15}Cu_5$ alloy detected by DTA is close to 500°C. In contrast, as talked in previous section, $Nd_{62}Fe_{14}Ga_{20}Cu_5$ alloy system shows four phase transition points where two peaks are under the heat-treatment temperature of the diffusion process.

4.3.3 Magnetic properties of Nd-Fe-Ga-Cu and Nd-Ga-Cu diffusion-processed magnets

Hysteresis loops of the hot-deformed, $Nd_{80}Ga_{15}Cu_5$ and $Nd_{62}Fe_{14}Ga_{20}Cu_4$ processed magnets are shown in Fig. 4-5(a). The infiltrated samples show nearly the same coercivity ($\mu_0 H_c$) of about 2.2 T, while the Nd-Fe-Ga-Cu diffusion-processed magnet exhibited smaller deterioration of remanent magnetization ($\mu_0 M_r$) from the initial magnet, which was from 1.50 T to 1.30 T. However, the Nd-Ga-Cu diffusion-processed magnet shows the remanence drop to 1.08 T. The values of M_r/M_s which is a direct indicator of the easy-axis alignment [7] are 0.94(6), 0.91(7) and 0.93(4) for the hot-deformed, Nd-Ga-Cu and Nd-Fe-Ga-Cu diffusion-processed magnets respectively.

The S-shaped initial magnetization curves reveal typical feature of domain wall pinning dominant magnetization process [8]. It starts from being highly susceptible with applied field corresponding to the domain wall displacement within the multi-domain grains, then enters a lower-susceptibility region when domain walls got pinned by the intergranular phases and followed by the magnetization rotation process reaching saturation [9].

Fig. 4-5(b) depicts the (volume) susceptibility derived from the initial magnetization curve in Figure 1(a). It first decreases as increasing the applied field, then increases reaching the peak value followed by a decrease to near 0 again. This could be another way of showing the S-shaped magnetization behavior of the pinning dominant magnetization process. The field at the peak of the susceptibility increment shoulder corresponds to the depinning-field of the magnet. It shows 0.72 T, 1.91 T and 2.16 T for the hot-deformed, Nd-Ga-Cu and Nd-Fe-Ga-Cu diffusion-processed magnets, respectively, which shows good correlations with their coercivity.

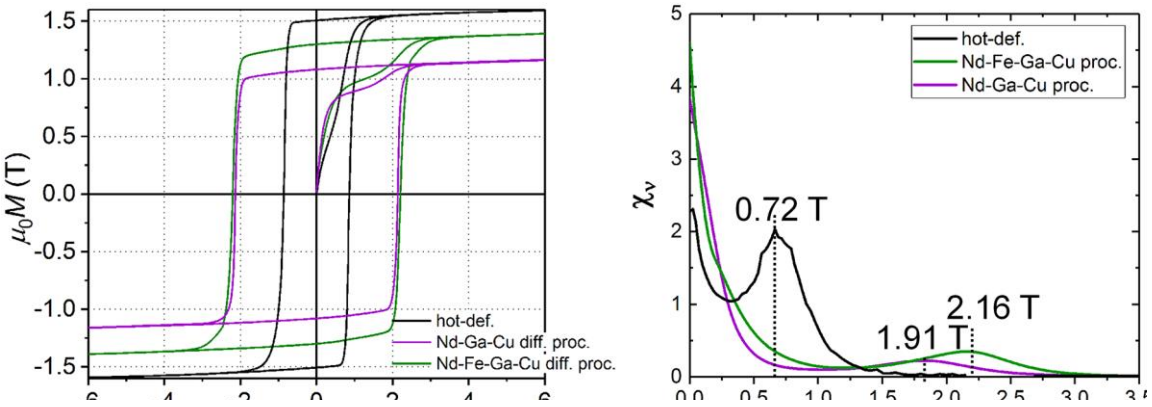

Fig. 4-5 (a) Hysteresis loops, (b) susceptibility of the magnetization curves of the hot-deformed, Nd-Ga-Cu and Nd-Fe-Ga-Cu diffusion-processed magnets.

Fig. 4-6(a) shows temperature dependence of coercivity of initial hot-deformed, Nd-Ga-Cu and Nd-Fe-Ga-Cu diffusion-processed magnets, the temperature coefficient of coercivity (β) were calculated to be -0.478, -0.427 and -0.433%°C^{-1}, respectively. The temperature-dependent coercivity can be described using the phenomenological micromagnetic equation of H_c (T) =αH_A (T)-$N_{eff}M_s$ (T) [10]. α and N_{eff} can be derived by taking a linear fit for the plot of H_c(T)/M_s(T) versus H_a(T)/M_s(T) as shown in Fig. 4-6(b). α showed an increase from 0.34, that of initial sample, to 0.64 and 0.68 for Nd-Ga-Cu and Nd-Fe-Ga-Cu diffusion-processed samples, suggesting the reduction of defect regions after the diffusion process [11]. The Nd-Fe-Ga-Cu diffusion-processed sample has slightly larger N_{eff} than Nd-Ga-Cu diffusion-processed sample. This is considered to be due to the higher degree of easy-axis alignment in the Nd-Fe-Ga-Cu diffusion-processed magnet [12] which in turn results in a larger localized demagnetizing field experienced by individual domains. This caused a slightly inferior thermal stability of the sample processed with Nd-Fe-Ga-Cu.

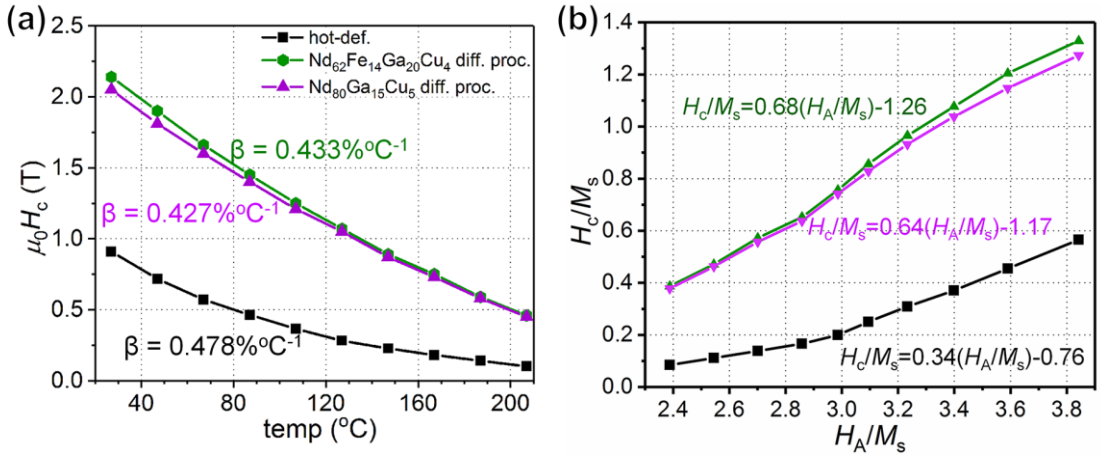

Fig. 4-6 (a) Temperature dependence of coercivity, (b) H_c/M_s (T) vs H_A/M_s (T) plot of the hot-deformed, Nd-Ga-Cu and Nd-Fe-Ga-Cu diffusion-processed magnets.

Fig. 4-7 shows magnetic properties of Nd-Fe-Ga-Cu and Nd-Ga-Cu diffusion-processed samples with different infiltrated amount of diffusion sources, as given by the numbers beside the data points which is the weight gain ratio over initial samples. Compared with Nd-Ga-Cu processed samples, smaller remanence reduction is seen in Nd-Fe-Ga-Cu processed samples. When the comparison is made with other Nd-rich eutectic alloys reported in Ref. [2], Nd-Fe-Ga-Cu alloy also shows unique merit as realizing coercivity improvement with smaller remanence deterioration. The inset figure shows the change of coercivity increment with increasing infiltration amount to initial magnets. It implies that Nd-Fe-Ga-Cu alloy can reduce the amount of applied diffusion sources to achieve the same level of coercivity

4.3.4 Microstructure of Nd-Ga-Cu and Nd-Fe-Ga-Cu diffusion-processed magnets

Fig. 4-8 compares BSE SEM images obtained for initial hot-deformed (Fig. 2(a)), surface and center regions of Nd-Ga-Cu (Figs. 2(b), (c)) and Nd-Fe-Ga-Cu (Figs. 2(d), (e)) diffusion-processed samples, observed from the transverse direction. The observations indicate thick Nd-rich intergranular phase(s) formed predominately on the flat facets (c plane) of $Nd_2Fe_{14}B$ grains. Almost same amount of Nd-rich intergranular phase was observed in surface and center regions of the Nd- Fe-Ga-Cu diffusion processed

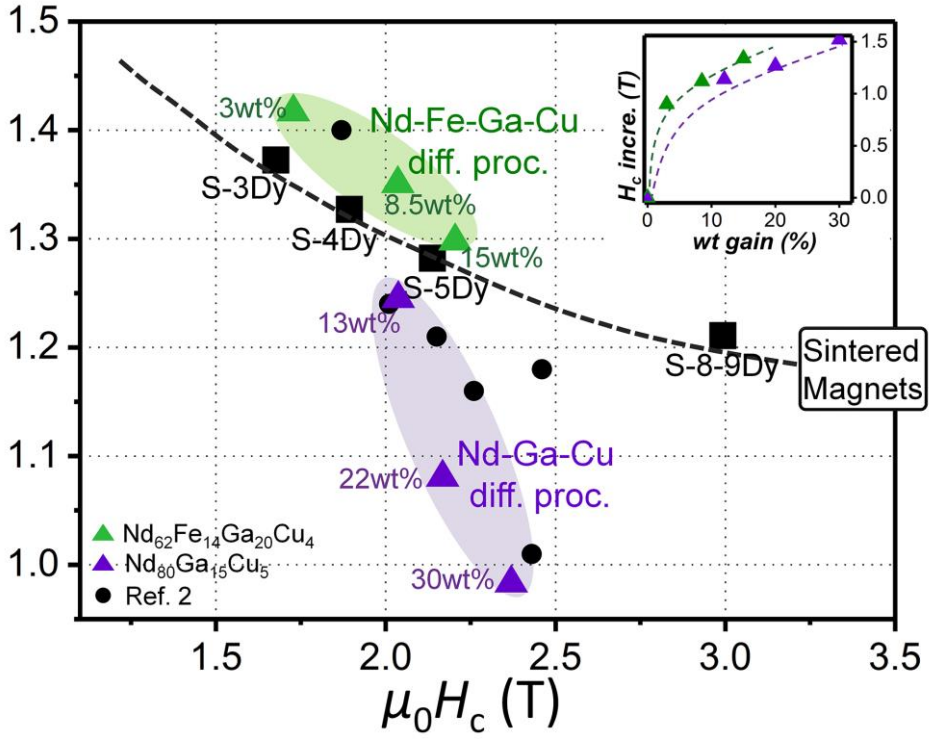

Fig. 4-7 Magnetic properties of sintered magnets with different amount of Dy addition and the hot-deformed magnets infiltrated with various diffusion sources, the inset figure shows the coercivity enhancement with weight increment of $Nd_{80}Ga_{15}Cu_5$ and $Nd_{62}Fe_{14}Ga_{20}Cu_4$ diffusion-processed samples.

sample, indeed its areal fraction varies from 14% to 13%. However it shows an apparent decrease from 24% to 13% in the Nd-Ga-Cu diffusion-processed sample. This indicates more efficient infiltration of Nd-Fe-Ga-Cu alloy upon melting. Moreover, unlike the degraded crystallographic texture in Nd-Ga-Cu diffusion-processed sample, most of the $Nd_2Fe_{14}B$ grains are well aligned in Nd-Fe-Ga-Cu diffusion-processed sample.

Manifest abnormal growth can be observed in Nd-Ga-Cu diffusion-processed sample, especially in the surface regions. It can also be seen that aggregation of Nd-rich intergranular phases, usually gathers in triple junctions happens along with the abnormal grain growth. The abnormal grain growth can also be directly seen from the grain size statistics if we take the aspect ratio as an indicator. The aspect ratio of $Nd_2Fe_{14}B$ grains of the hot-deformed, Nd-Ga-Cu and Nd-Fe-Ga-Cu diffusion-processed magnets is 3.92, 3.27 and 3.73 respectively. The abrupt change in aspect ratio of Nd-Ga-Cu diffusion-processed sample also implies the more severe abnormal grain growth compared to Nd-Fe-Ga-Cu diffusion-processed sample despite they exhibit very similar average grain size both in length and width.

To figure out the mechanism of coercivity enhancement as well as the texture evolution, careful compositional investigation on the diffusion-processed samples was carried out. For fare comparison, the TEM specimens were lift out from regions with the same depth (~200μm from the c-plane) for the two samples. Figure 4-9 is the comparison of the HAADF-STEM image and the EDS-maps of Nd-Ga-Cu (a) and Nd-Fe-Ga-Cu (b) diffusion-processed magnets. The HAADF images of the two samples again confirmed a

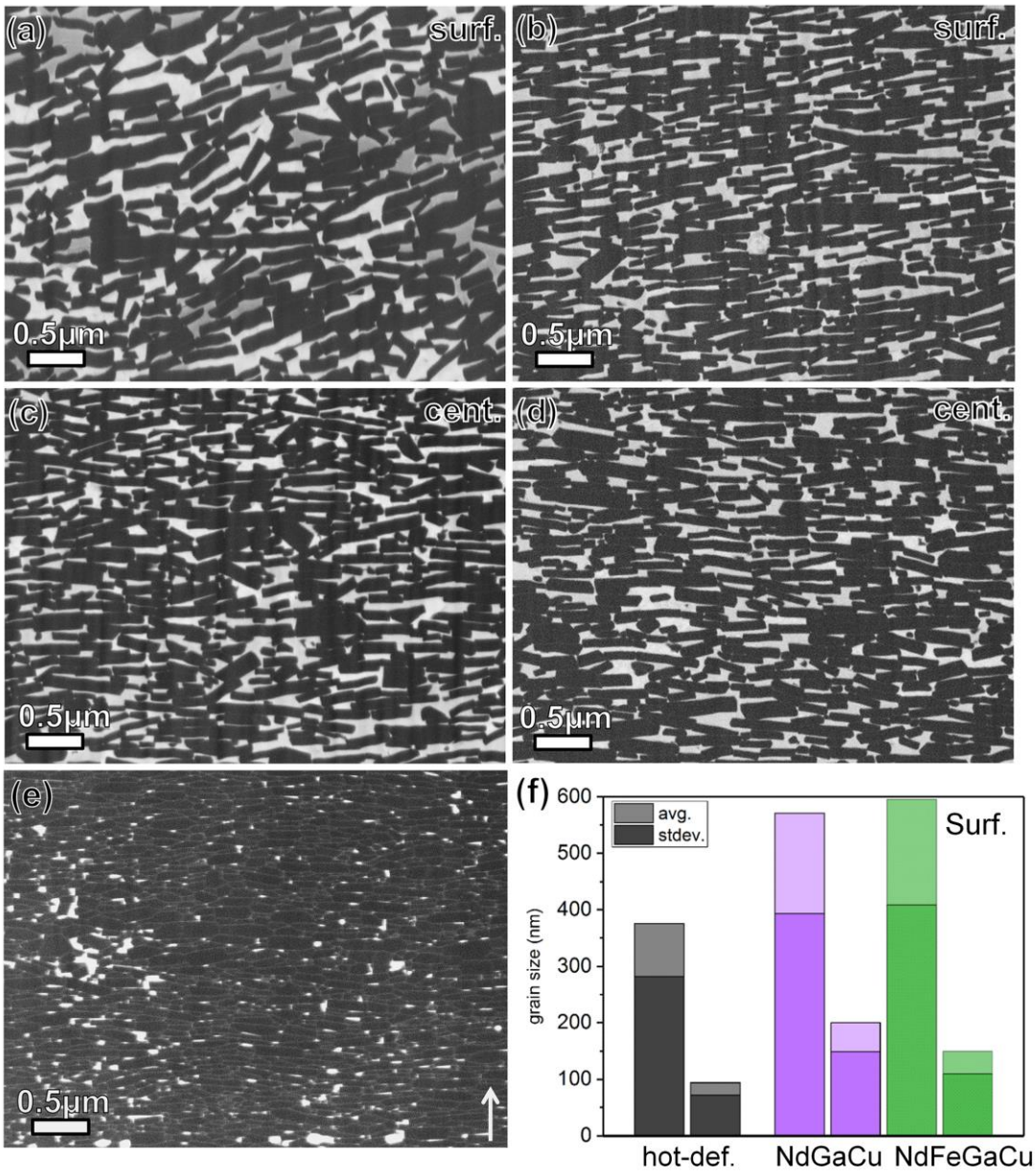

Fig. 4-8 BSE SEM images of (a) surface and (c) center regions of $Nd_{80}Ga_{15}Cu_5$ diffusion-processed, (b) surface and (d) center regions of $Nd_{62}Fe_{14}Ga_{20}Cu_4$ diffusion-processed magnets. (e) hot-deformed magnets; (f) Grain size statistics of surface regions of the hot-deformed, Nd-Ga-Cu and Nd-Fe-Ga-Cu diffusion-processed magnets.

higher degree of easy-axis alignment of $Nd_2Fe_{14}B$ grains of Nd-Fe-Ga-Cu diffusion-processed sample, despite the limited sampling size by TEM characterization. The compositional image of Nd which is colored in red revealed the fact of the inhomogeneous formation of Nd-rich intergranular phase during the solidification process. It shows preferential distribution along the flat surface parallel to the basal plane of the matrix phase, whereas the existence neighboring to the side surfaces or higher-index planes was quite irregular. This is commonly observed for both Nd-Ga-Cu and Nd-Fe-Ga-Cu diffusion-processed samples. However, the irregularity was not only seen in the distribution in terms of the difference in thickness and the emergence site, non-uniform enrichment of other alloy elements could also be found. We can see at least two kinds of contrast existed in the compositional images of Cu, Ga as well as Co. Ga and Cu are showing similar enrichment tendency while different from that of Co. We note the obvious partitioning of Co in the intergranular phase in both diffusion-processed samples, which demonstrated a uniform distribution across the matrix phase and the grain boundaries in the initial as hot-deformed sample (refer to Chapter 3.3). The effect of improving T_c via Co doping in $Nd_2Fe_{14}B$ phase indeed diminished or got weakened after the diffusion process. Nevertheless, the diffusion-processed magnets exhibited a better thermal stability in comparison with the initial as hot-deformed magnet as a result of the formation of Nd-rich intergranular phase. The heterogeneous distribution of Ga and Cu is most likely a product of the phase decomposition on solidification due to the different formation energy of the different types of intergranular phases. Even though some difference can be seen in terms of the thickness of the intergranular phases, no propounding information could be derived explanation for the different penetration depths between Nd-Ga-Cu and Nd-Fe-Ga-Cu alloys, also for the different behavior of the texture evolve of them. We believe the minor change in the chemical composition or the crystal structure of the intergranular phases will have a sounding influence on the mobility of the grain boundary as well as the wettability with $Nd_2Fe_{14}B$ phase. To confirm this point, we carried out further careful analysis for the intergranular phases and the interface features.

Fig. 4-10 (a) shows the superimposed elemental map taken from Nd-Ga-Cu diffusion-processed sample with Nd displayed in red, Fe in green and Ga in cyan. Not shown is Cu and Co. The enrichment of Nd and Ga and the depletion of Fe are observed in the intergranular phase. Two types of intergranular phases are observed: one is highly enriched in Ga (hereafter denoted as Nd-rich phase 1) another contains higher amount of Nd (Nd-rich phase 2). Nd-rich phase 1 with the composition of $Fe_{6.3}Nd_{60.9}Ga_{17.1}Co_{8.1}Cu_{7.6}$ at. % determined from the line-scan profile (Fig. 3(c)) was identified to be fcc structure with a = 5.534 Å [13]. The interface between the Nd-rich phase and the $Nd_2Fe_{14}B$ phase is indicated as the dashed line in the line-scan profile. Fig. 4-10 (b) shows the HAADF-STEM image of a Nd-rich phase 1 /$Nd_2Fe_{14}B$ interface taken with the electron beam along the <-110> zone-axis of the $Nd_2Fe_{14}B$ phase. $Nd_2Fe_{14}B$ phase is imaged with atomic resolution on zone axis whereas Nd-rich phase 1 shows amorphous-like feature suggesting it has no crystallographic orientation correlation with the matrix phase. Fig. 4-10 (e) shows a Nd-rich phase 2/$Nd_2Fe_{14}B$ interface with the (002) plane of $Nd_2Fe_{14}B$ phase as the termination layer. Nd-rich phase 2 has the composition of $Fe_{4.0}Nd_{79.3}Ga_{1.1}Co_{12.0}Cu_{3.6}$ and its structure is indexed as $I\bar{a}3$ type with a = 1.052 nm [14]. Despite the high concentration of Nd (known as heavy scatter with large atom number *Z*), Nd-rich phase 2 in

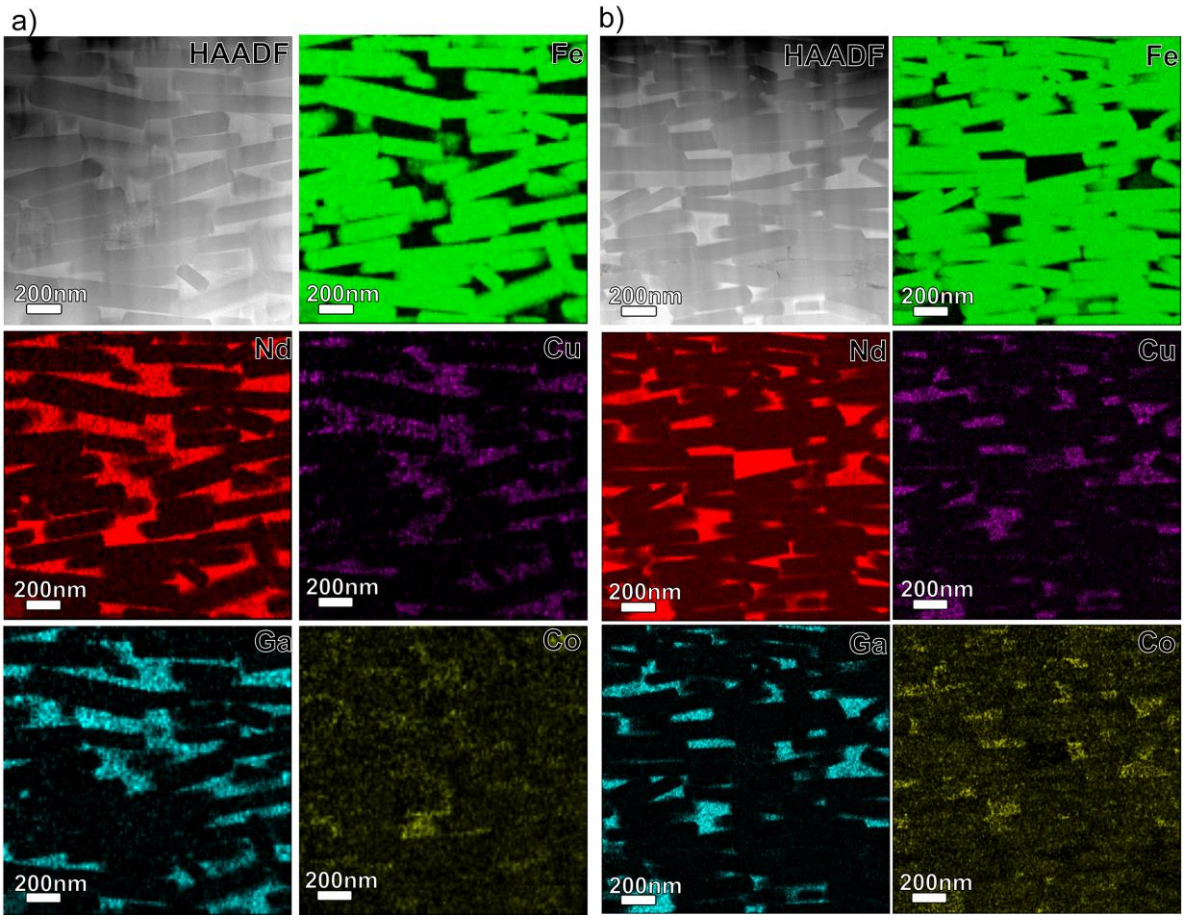

Fig. 4-9 HAADF-STEM image and EDS element mapping for Fe, Nd, Ga, Cu, Co elements of Nd-Ga-Cu (a) and Nd-Fe-Ga-Cu (b) diffusion-processed magnets..

this case is showing darker contrast in comparison with $Nd_2Fe_{14}B$ phase. This is known as the "channeling" effect when the probing electrons travel down a low-order zone-axis which will cause frequent and strong interaction with atoms in the crystal as a result of Coulomb force [15]. Near the interface, segregation of Ga, Cu and Co was found by taking the quantitative analysis through line-scan across the Nd-rich phase 2 /$Nd_2Fe_{14}B$ interface. Co shows around 27 at.% segregation at the interface.

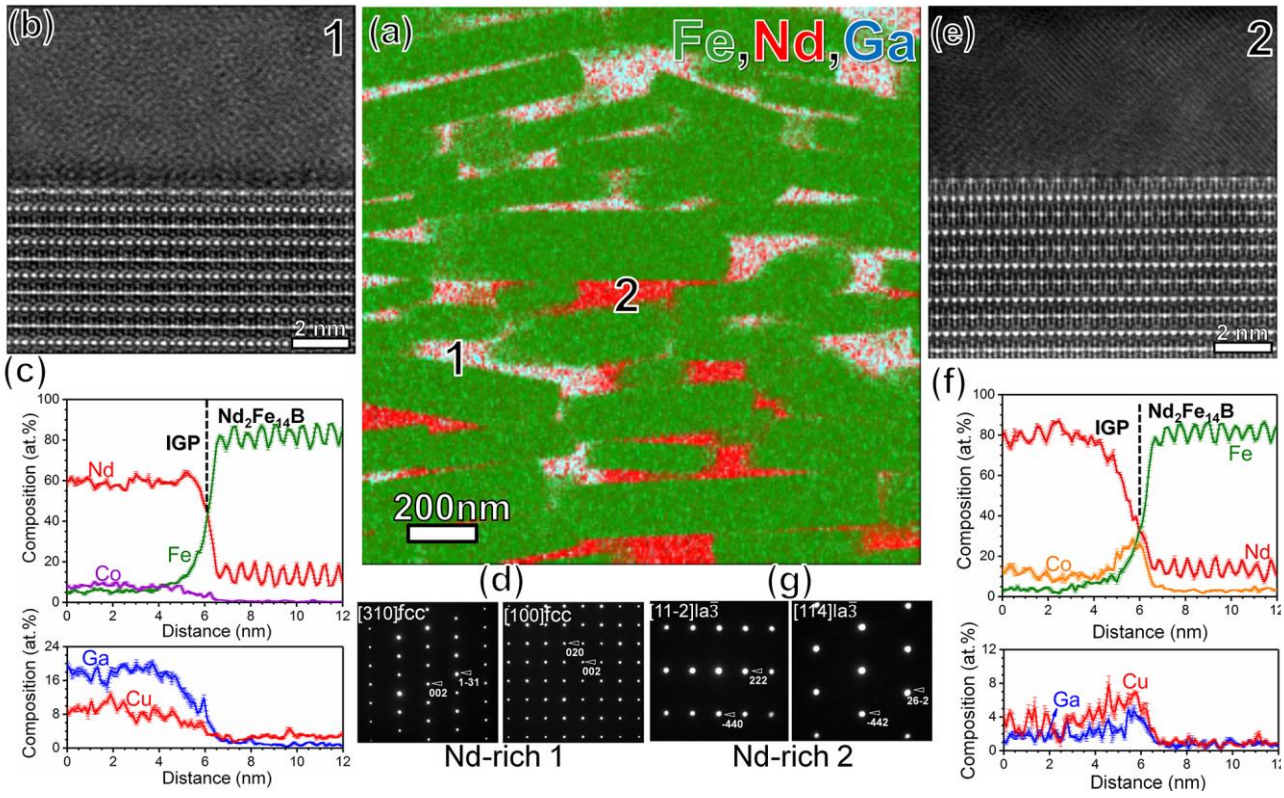

Fig. 4-10 (a) Superimposed EDS elemental map of Fe, Nd and Ga, (b) Nd-rich phase 1/ $Nd_2Fe_{14}B$ interface, (c) line-scan profile across the interface shown in b, (d) NBED of Nd-rich phase 1, (e) Nd-rich phase 2/ $Nd_2Fe_{14}B$ interface, (f) line-scan profile across the interface shown in e, (g) NBED of Nd-rich phase 2 from $Nd_{80}Ga_{15}Cu_5$ diffusion-processed sample.

Fig. 4-11 (a) is a superimposed elemental map of the Nd-Fe-Ga-Cu diffusion-processed sample. Two types of intergranular phases are observed, one is containing more Ga (Nd-rich phase A) and the other is more enriched with Nd (Nd-rich phase B). The interface between Nd-rich phase A and $Nd_2Fe_{14}B$ phase shown in Fig. 4-11 (b) displays a bilayer lattices, composed with Nd and Fe atoms which could be seen from the shoulder feature in the Nd and Fe line-scan profiles (Fig. 4(c)). The line-scan analysis gives the composition of Nd-rich phase A as $Fe_{8.4}Nd_{57.5}Ga_{15.8}Co_{9.3}Cu_{9.0}$ and it was determined as the hcp structure, with a= 6.878 Å, c= 5.397 Å. On the other hand, Nd-rich phase B has the composition of $Fe_{3.4}Nd_{92.6}Ga_{0.6}Co_{3.0}Cu_{0.3}$ corresponding to the $Ia\bar{3}$ phase with a = 1.052 nm. Nd-rich phase B/ $Nd_2Fe_{14}B$ interface does not show lattice fringes of a single crystal. In fact, if we perform tilt experiment to the Nd-rich phase B, we found it formed in nanocrystalline with varied crystallographic orientations as shown in Fig. 4(e). When we tilt the beam to be oriented with the zone-axis of region I to make it atomically resolved then region II could only be resolved as 1D-lattice fringe, region III appearing to be free of any lattice fringes turning into amorphous-like feature. This also suggests that the Nd-rich intergranular phase doesn't hold a preferential crystallographic relationship with the matrix phase.

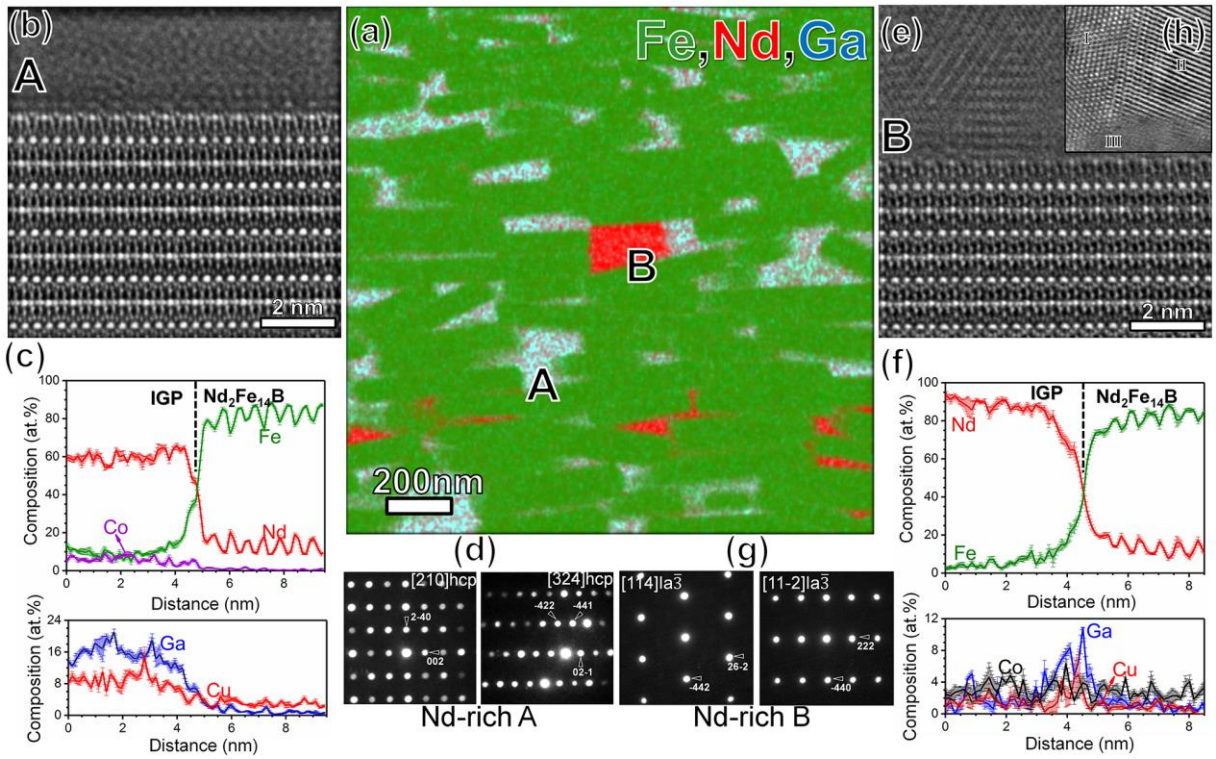

Fig. 4-11 (a) Superimposed EDS elemental map of Fe, Nd and Ga, (b) Nd-rich phase A/ $Nd_2Fe_{14}B$ interface, (c) line-scan profile across the interface shown in b, (d) NBED of Nd-rich phase 1, (e) Nd-rich phase B/ $Nd_2Fe_{14}B$ interface, (f) line-scan profile across the interface shown in e, (g) NBED of Nd-rich phase B (h) microstructure of Nd-rich phase B with electron beam oriented along the zone-axis of region I, taken from $Nd_{62}Fe_{14}Ga_{20}Cu_4$ diffusion-processed sample.

4.4 Discussion

In this work, based on the inspiration from the Ga-doped sintered magnets exhibit a significantly large enhancement in coercivity with post-sinter annealing in contrast with conventional sintered magnets [xx], the Ga-based alloys were investigated as the diffusion sources for the eutectic grain boundary diffusion process. Since phase diagram and the information on the Ga-based ternary or even quaternary alloys are obviously missing in this blind optimization journey, the composition design in this work is done by the try-error experiment. In fact, near 20 types of Nd-Ga-Cu alloys were examined by testing their melting point and applying to the diffusion process. Figure 4-1 gives the summarization of the magnetic properties of partial diffusion-processed magnets. $Nd_{80}Ga_{15}Cu_5$ is the champion alloy in terms of the effect of coercivity enhancement (saturation coercivity is 2.60T with applying infinite amount of diffusion sources) among all the ternary alloys we've tried including $Nd_{80}Ga_{10}Cu_{10}$, $Nd_{70}Ga_{20}Cu_{10}$, $Nd_{70}Ga_{10}Cu_{20}$, $Nd_{70}Ga_{25}Cu_5$, $Nd_{70}Ga_5Cu_{25}$ etc.

$Nd_{62}Fe_{14}Ga_{20}Cu_4$ was prepared by the subtraction of $Nd_2Fe_{14}B$ phase from the nominal composition of the Ga-doped sintered magnet. From our characterization, $Nd_{62}Fe_{14}Ga_{20}Cu_4$ "compound" is actually a mixture of several alloys. Even so, when $Nd_{62}Fe_{14}Ga_{20}Cu_4$ and $Nd_{80}Ga_{15}Cu_5$ diffusion-processed magnets show nearly the same coercivity of 2.2 T, smaller degradation of remanence was realized in the Nd-Fe-Ga-

Cu diffusion-processed magnet, from 1.50 T to 1.30 T. On the other hand, a substantial deterioration to 1.08 T was observed in the Nd-Ga-Cu diffusion-processed magnet. The further experiment by varying the amount of applied diffusion sources for the two alloys also revealed the capability of $Nd_{62}Fe_{14}Ga_{20}Cu_4$ to achieve a same level of coercivity with smaller weight gain of the magnet, which will enable us realize the coercivity enhancement with less sacrifice of the remanent magnetization from the initial hot-deformed magnets.

We found that along with the formation of thick Nd-rich intergranular phases, abnormal grain growth of $Nd_2Fe_{14}B$ phase also occurred. This is more manifest for surface regions of the diffusion-processed magnets. In this work, more agglomeration of Nd-rich intergranular phases and abnormal grain growth was observed in the surface region of $Nd_{80}Ga_{15}Cu_5$ diffusion-processed magnet.

Characterizations by STEM and NBED have provided detailed information on the microstructure of Nd-rich intergranular phases of Nd-Ga-Cu and Nd-Fe-Ga-Cu diffusion-processed magnets. These Nd-rich phases are believed to be non-ferromagnetic based on the low Fe concentration [16], which would provide an exchange decoupling between $Nd_2Fe_{14}B$ grains. However, since the texture development is affected by the coupling effect of grain boundary curvature [17] and grain growth behavior [18], to figure out the mechanism of texture evolution, a molecular dynamic simulation separating different mechanisms is necessary.

We have demonstrated Nd-Fe-Ga-Cu processed magnet retains high remanence due to efficient infiltration and less-distorted texture. However, poor control over texture establishing limits the potential of this eutectic grain boundary diffusion process. Recent report on the fabrication of highly anisotropic nanocomposites by a multi-field coupling deformation process [19, 20] showed great progress on the controllable synthesis of hybrid nanostructures. It also shed a light on our research journey on seeking for the possibility of restoring the texture of the diffusion-processed magnets.

4.5 Conclusion

In this chapter, further optimization was done to seek for an optimal diffusion sources among Ga-based alloys. The detailed comparison was taken between $Nd_{80}Ga_{15}Cu_5$ and $Nd_{62}Fe_{14}Ga_{20}Cu_4$ diffusion-processed magnets. Major conclusions from the work of this chapter are listed as below,

(1) As diffusion sources, $Nd_{62}Fe_{14}Ga_{20}Cu_4$ shows merit in terms of realizing the coercivity improvement with less sacrificing of remanent magnetization as a result of more efficient penetration and less distorted easy axis alignment;

(2) TEM observations confirmed the Nd-rich intergranular phase(s) formed in $Nd_{62}Fe_{14}Ga_{20}Cu_4$ diffusion-processed magnet has the $I\bar{a}3$ and hcp structure, while those in the $Nd_{80}Ga_{15}Cu_5$ diffusion-processed magnet have the $I\bar{a}3$ and fcc structures. However, the dominant factor of the texture evolution remains unveiled;

(3) $Nd_{62}Fe_{14}Ga_{20}Cu_4$ diffusion-processed magnet exhibits superior magnetic properties to that achieved by Nd-Cu diffusion-process under expansion constraint [4]. This is great progress in our research journey in pursuing the most ideal diffusion source.

References

[1] H. Sepehri-Amin, T. Ohkubo, T. Nishiuchi, S. Hirosawa, and K. Hono,"Coercivity enhancement of hydrogenation-disproportionation-desorption-recombination processed Nd-Fe-B powders by the diffusion of Nd-Cu alloys," *Scripta Mater.*, vol. 63, no. 11, pp. 1124-1127, Nov.2010.

[2] L. Liu, H. Sepehri-Amin, T. Ohkubo, M. Yano, A. Kato, T. Shoji, and K. Hono, "Coercivity enhancement of hot-deformed Nd-Fe-B magnets by the eutectic grain boundary diffusion process," *J. Alloy. Compd.*, vol. 666, pp. 432-439, May. 2016.

[3] U. M. R. Seelam, L. Liu, T. Akiya, H. Sepehri-Amin, T. Ohkubo, N. Sakuma, M. Yano, A. Kato, and K. Hono, "Coercivity of the Nd-Fe-B hot-deformed magnets diffusion-processed with low melting temperature glass forming alloys," *J. Magn. Magn. Mater.*, vol. 412, pp. 234-242, Aug. 2016.

[4] T, Akiya, J. Liu, H. Sepehri-Amin, T. Ohkubo, K. Hioki, A. Hattori, and K. Hono, "High-coercivity hot-deformed Nd-Fe-B permanent magnets processed by Nd-Cu eutectic diffusion under expansion constraint," *Scripta Mater.*, vol. 81, pp. 48-51, Jun. 2014.

[5] K. Nakajima, T, Yamazaki, "R-T-B rare-earth permanent magnets, motors, automotives, electricity generator, wind turbine generators," *JPN Patent*, 5767788, issued June 29, 2015.

[6] T. T. Sasaki, T. Ohkubo, Y. Takada, T. Sato, A. Kato, Y. Kaneko, and K. Hono, "Formation of non-ferromagnetic grain boundary phase in a Ga-doped Nd-rich Nd-Fe-B sintered magnet," *Scripta Mater.*, vol. 113, pp. 218-221, Mar.2013.

[7] S. Hirosawa, A. Hanaki, H. Tomizawa, and A. Hamamura, "Current status of Nd-Fe-B permanent magnet materials,"*Phys. B*, vol. 164, no. 1-2, pp.117-123, Jun. 1990.

[8] F. E. Pinkerton, and C. D. Fuerst, "Coercivity of die upset Nd-Fe-B magnets: A strong pinning model," *J. Magn. Magn. Mater.*, vol. 89, no. 1-2, pp. 139-142, Sep. 1990.

[9] D. I. Paul, "General theory of the coercive force due to domain wall pinning,"*J. Appl. Phys.*, vol. 53, no. 3, pp. 1649-1654, Mar. 1982.

[10] H. Kronmüller, K.-D. Durst, and M .Sagawa, "Analysis of the magnetic hardening mechanism in RE-FeB permanent magnets," *J. Magn. Magn. Mater.*, vol. 74, no. 3, pp. 291-302, May. 1988.

[11] H. Sepehri-Amin, T. Ohkubo, M. Gruber, T. Schrefl, and K. Hono, "Micromagnetic simulations on the grain size dependence of coercivity in anisotropic Nd-Fe-B sintered magnets," *Scripta Mater.*, vol. 89, pp. 29-32, Oct. 2014.

[12] D. C. Crew, L. H. Lewis, and V. Panchanathan, "The effect of evolving grain shape and alignment on the coercivity in thermomechanically deformed $Nd_{13.9}(Fe_{0.92}Co_{0.88})_{80.3}B_{5.3}Ga_{0.5}$ permanent magnets," *J. Magn. Magn. Mater.*, vol. 223, no. 3, pp. 261-266, Feb. 2001.

[13] W. Mo, L. Zhang, Q. Liu, A. Shan, J. Wu, and M. Komuro, "Dependence of the crystal structure of the Nd-rich phase on oxygen content in an Nd-Fe-B sintered magnet," *Scripta Mater.*, vol. 59, no. 2, pp. 179-182, Jul. 2008.

[14] Y. Shinba, T. J. Konno, K. Ishikawa, K. Hiraga, and M. Sagawa, "Transmission electron microscopy study on Nd-rich phase and grain boundary structure of Nd-Fe-b sintered magnets," *J. Appl. Phys.*, Vol. 97, no. 3, pp. 053504, Feb. 2005.

[15] A. J. D'Alfonso, B. Freitag, D. Klenov, and L. J. Allen, "Atomic-resolution chemical mapping using energy-dispersive x-ray spectroscopy," *Phys. Rev. B.*, vol. 81, no. 10, pp. 100101, Mar. 2010.

[16] A. Sakuma, T. Suzuki, T. Furuuchi, T. Shima, and K. Hono, "Magnetism of Nd-Fe films as a model of grain boundary phase in Nd-Fe-B permanent magnets," *Appl. Phys. Express*, vol. 9, no.1, pp. 013002 Dec. 2015.

[17] V. Yamakov, D. Moldovan, K. Rastogi, and D. Wolf, "Relation between grain growth and grain-boundary diffusion in a pure material by molecular dynamics simulations," *Acta Mater.*, vol. 54, no. 15, pp. 4053-4061, Sep. 2006.

[18] Paul. A. Beck, Philip R. Sperry, and Hsun Hu, "The orientation dependence of the rate of grain boundary migration," *J. Appl. Phys.*, vol. 21, no. 5, pp. 420-425, May. 1950.

[19] X. Li, L. Lou, W. Song, Q. Zhang, G. Huang, Y. Hua, H.- T. Zhang, J. Xiao, B. Wen, and X. Zhang, "Controllably manipulating three-dimensional hybrid nanostructures for bulk nanocomposites with large energy products," *Nano Lett.* , vol. 17, no. 5, pp. 2985-2993, May. 2017.

[20] X. Li, W. Song, G. Huang, F. Hou, Q. Zhang, H. –T. Zhang, J. Xiao, B. Wen, and X. Zhang, "Novel bimorphological anisotropic bulk nanocomposite materials with high energy products," *Adv. Mater.*, vol. 29, no. 16, pp. 1606430 Apr. 2017.

5 Chapter 5 Coercivity enhancement of the hot-deformed Nd-Fe-B magnets by the eutectic grain boundary diffusion process using Nd-Dy-Al and Nd-Tb-Cu alloys

5.1 Introduction

Nd-Fe-B based sintered magnets exhibit excellent magnetic properties and are widely used in industry as essential components of energy applications such as the application in traction motors in hybrid or electric vehicles (HVs or EVs). However, the temperature stability of the HRE-free sintered magnets is rather poor. Since the application environment causes temperature under demagnetization fields, not only high remanence but also high coercivity at elevated temperature is required. In order to attain the coercivity around 0.8 T at the operation temperature of 200^{o}C, around 10 wt.% Dy is alloyed in the commercial Nd-Fe-B sintered magnets as the partial substitution of Nd with Dy, which increases the anisotropy field of $(Nd_{1-x}Dy_x)_2Fe_{14}B$ [1]. As a drawback, the magnetic moment of Dy is antiferromagnetically coupled with Fe atom in the $Nd_2Fe_{14}B$ compound, leading to a deterioration of magnetization M_s as well as the energy product $(BH)_{max}$ as coercivity increases. To overcome this problem, in 2000, the heavy rare earth elements (HRREs) grain boundary diffusion process (GBDP) was proposed by Park et al [2], where Dy metal was deposited by sputtering on the surface of the magnets followed by a heat-treatment. The idea is to introduce Dy only at the periphery of $Nd_2Fe_{14}B$ grains where nucleation and propagation of magnetic reversal gets initiated. The HREEs diffusion process has received a lot of attention and achieved great progress since this method will also save the use of HREEs to a large content which has been the critical issue when it comes to the utilization of HREEs in the commercial production of Nd-Fe-B permanent magnets. This is because the very high cost of HREEs associated with their monopolistic supply market and the geological reserve amount.

Rare earth grain boundary diffusion process was developed for enhancing the coercivity of sintered magnets with the grain size of about 5 μm using various types of diffusion sources, including Dy-vapor, Dy and Tb oxides, Dy and Tb fluorides and thin film deposition [2-5]. Unlike the eutectic diffusion process, this method cannot be employed in hot-deformed Nd-Fe-B magnets since the high temperature annealing results in catastrophic grain growth in fine-grained hot-deformed Nd-Fe-B magnets. Recently, Sepehri-Amin reported that Dy-rich interface can be developed without any grain growth in Nd-Fe-B hot-deformed magnet using $Nd_{60}Dy_{20}Cu_{30}$ powder as a diffusion source followed by annealing at low temperature of 650 ^{o}C [6]. By applying this method, a high coercivity of 2.6 T was demonstrated in 1-mm thick hot-deformed Nd-Fe-B magnet. Exploring how high coercivity can be obtained with a small addition of Dy to a low melting temperature eutectic alloys while keeping relatively high remanence value of at least 1.3 T is important for developing practical Dy-saving high coercivity alloy.

The aim of the work in this chapter is to enhance the coercivity of the hot-deformed Nd-Fe-B with a thickness of 2 mm by the diffusion of Nd-Dy-Al and Nd-Tb-Cu alloys. The composition of the Nd-Dy-Al is

designed as $Nd_{62}Dy_{20}Al_{18}$ at.%, which is decided based on the work in Chapter 1 where $Nd_{90}Al_{10}$ alloy is found to be the champion diffusion source in the aspect of coercivity enhancement at room temperature. On the other hand, the composition of Nd-Tb-Cu alloys was designed as $Nd_{60}Tb_{10}Cu_{30}$ and $Nd_{60}Tb_{20}Cu_{20}$ at.%. We expect an improved thermal stability through the formation of Tb-rich shell structure and the formation of Nd-rich intergranular phase.

5.2 Experimental

The eutectic grain boundary diffusion process was applied to the hot-deformed magnets in 4×4×2 mm^3 with the nominal composition of $Nd_{13.2}Fe_{76}Co_{5.6}B_{4.7}Ga_{0.5}$ (at.%). The height reduction of the hot-deformation was 75 % at 780 ^oC. $Nd_{62}Dy_{20}Al_{18}$, $Nd_{60}Tb_{10}Cu_{30}$ and $Nd_{60}Tb_{20}Cu_{20}$ ribbons were prepared by the melt-spinning technique. The hot-deformed Nd-Fe-B magnets in contact with ribbons were heat treat at 650^oC (for $Nd_{60}Tb_{10}Cu_{30}$ diffusion process) and 700 ^oC (for $Nd_{62}Dy_{20}Al_{18}$ and $Nd_{60}Tb_{20}Cu_{20}$ alloys) for 1 h. In the comparison Dy-vapor diffusion experiment, Dy-vapor diffusion process was applied to the hot-deformed magnets with the same composition and size at 900 ^oC for 4h. After the process, about 0.27 wt% Dy was introduced in the sample.

Magnetic measurements were carried out using a super conducting quantum interface device vibrating sample magnetometer (SQUID-VSM) for the platelet-shaped specimen sliced crossing sample surface and center with a maximum applied field of 7 T. Overall microstructural characterization was conducted using Carl ZEISS CrossBeam 1540EsB and the surfaces of samples were cleaned using focused ion beam (FIB) before SEM observation. Scanning transmission electron microscopy energy-dispersive spectroscopy (STEM EDS) maps were constructed using Nd-*L*α, Dy-*M*α, Fe-*K*α, Co-*K*α and Cu-*K*α spectrum. The specimen of TEM characterization was prepared with the lift-out method by a focused ion beam on FEI Nanolab Helios 650.

5.3 Coercivity enhancement of hot-deformed Nd-Fe-B magnets by the eutectic GBDP using $Nd_{62}Dy_{20}Al_{18}$ alloy

5.3.1 Magnetic properties

Fig. 5-1 (a) shows the hysteresis loops of the Nd-Dy-Al eutectic diffusion and Dy-vapor diffusion-processed hot-deformed magnets. The coercivity ($\mu_0 H_c$) of the hot-deformed magnet was enhanced from around 1.3 T to about 2.8 T by the $Nd_{62}Dy_{20}Al_{18}$ grain boundary diffusion process, while the remanence drop from 1.50 T to 1.30 T. Maximum magnetic product, $(BH)_{max}$ of the hot-deformed and Nd-Dy-Al diffusion-processed samples was evaluated to be 459 and 339 kJm^{-3}, respectively. In contrast, hot-deformed magnet treated by Dy vapor diffusion process at 900 ^oC for 4 h exhibited a deterioration of coercivity to 1.0 T without much change in remanence ($\mu_0 M_r$). The S-shaped initial magnetization curve of the hot-deformed magnet has a high-susceptibility region up to around 0.9 T, followed by a lower susceptibility part then increases again reaching saturation. This kind of behavior indicates the magnetization process takes place by the domain wall displacement in the multi-domain grains, then the domain walls are pinned at the

intergranular phase, then got depinned to reach saturation [7]. The depinning field increases substantially in the sample diffusion processed with $Nd_{62}Dy_{20}Al_{18}$. On the other hand, the Dy-vapor diffusion processed sample is magnetized in one stage, suggesting the pinning sites disappear and essentially all grains are multi-domain particles.

Fig. 5-1(b) shows temperature dependence of coercivity of the hot-deformed magnets and those for the samples diffusion processed with $Nd_{70}Cu_{30}$, $Nd_{90}Al_{10}$ and $Nd_{62}Dy_{20}Al_{18}$. Temperature coefficient of coercivity (β) for the hot-deformed, and the Nd-Cu, Nd-Al, Nd-Dy-Al diffusion-processed samples was calculated to be -0.47, -0.40, -0.43 and -0.39%$^{o}C^{-1}$, respectively. This indicates that the temperature coefficient can be improved by the grain boundary diffusion process. The typical β value for commercial sintered magnets is around -0.5~-0.6%$^{o}C^{-1}$. The Nd-Cu diffusion-processed magnet shows $\mu_0 H_c$ of 0.67 T at 200 ^{o}C while Nd-Al diffusion-processed magnet exhibits only 0.6 T at 200 ^{o}C while its room temperature coercivity is higher than that of Nd-Cu diffusion-processed sample [8]. This is because Al is dissolved in the $Nd_2Fe_{14}B$ phase to form $Nd_2(Fe,Al)_{14}B$ phase, by which the Curie temperature decreases while the anisotropy field is increased due to the reduction of M_s [9]. $Nd_{62}Dy_{20}Al_{18}$ diffusion-processed sample shows the highest coercivity of 2.8 T at room temperature, and the coercivity at 200 ^{o}C is also the highest, 0.75 T.

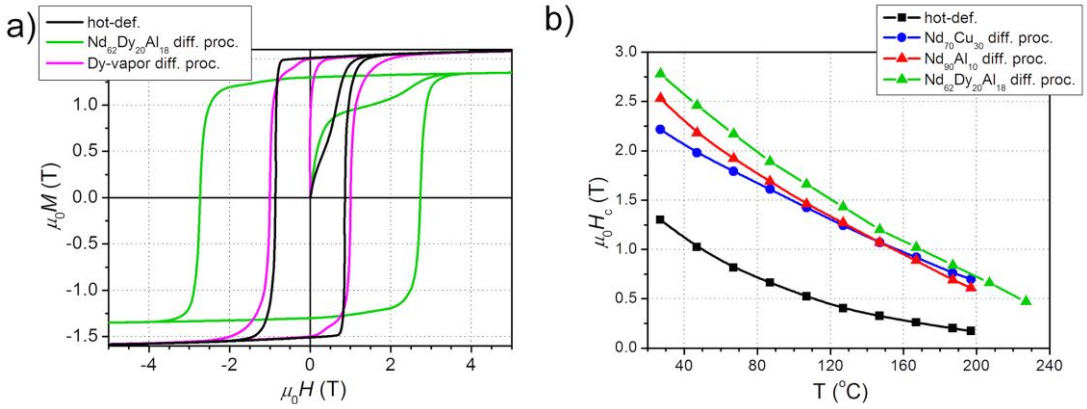

Fig. 5-1 (a) Hysteresis loops of the hot-deformed, $Nd_{62}Dy_{20}Al_{18}$ and Dy-vapor diffusion-processed samples; (b) Temperature dependence of coercivity of the hot-deformed, $Nd_{70}Cu_{30}$, $Nd_{90}Al_{10}$ and $Nd_{62}Dy_{20}Al_{18}$ diffusion-processed samples.

5.3.2 Microstructure of the diffusion-processed magnets

Figure 5-2 is the backscattered electron (BSE) SEM images of the hot-deformed sample (a), $Nd_{62}Dy_{20}Al_{18}$ diffusion-processed and Dy-vapor diffusion-processed samples (c), respectively, observed with the c-axis in-plane in upward direction. The as hot-deformed sample has the grain size of 282±94 nm in width, 72±21 nm in height, and brightly imaged Nd-rich phases are mainly at triple junctions. Grain boundaries are observed with faintly bright contrast, suggesting the Nd concentration along the grain boundaries is not so high in the as hot-deformed condition. The $Nd_{62}Dy_{20}Al_{18}$ diffusion-processed sample has the grains with 295±138 nm in width and 100±38 nm in height. We see there is no obvious grain growth in

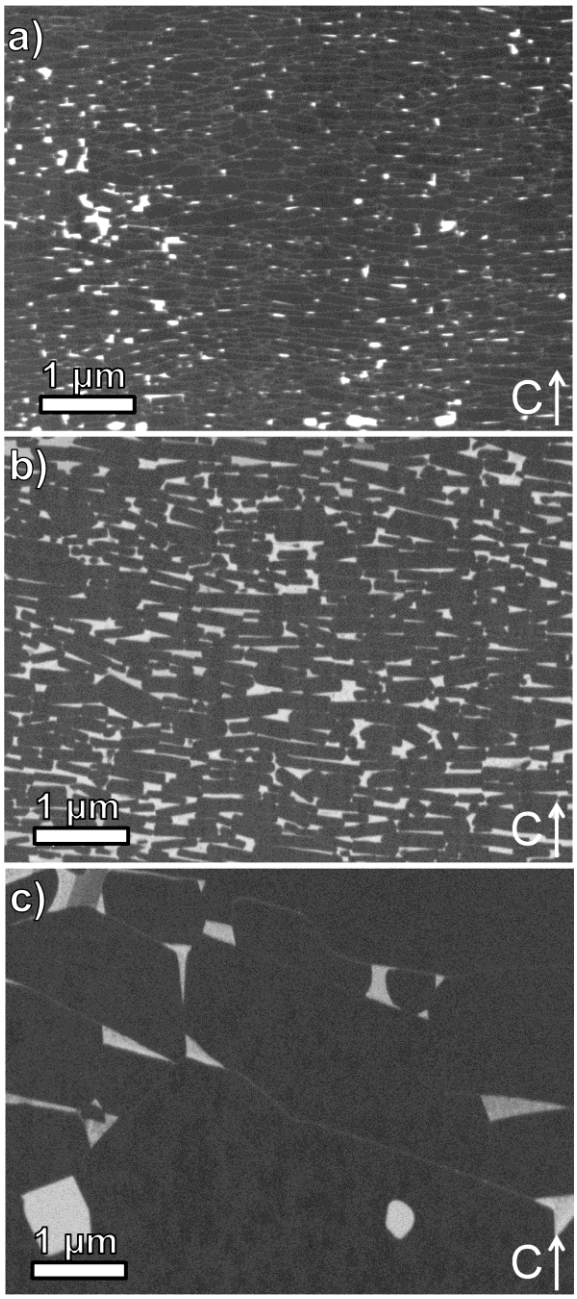

Fig. 5-2 BSE SEM images of the hot-deformed a), $Nd_{62}Dy_{20}Al_{18}$ diffusion b) and Dy-vapor diffusion-processed magnets c), with c-axis in-plane.

the diffusion-processed magnet. Larger particles of brightly imaged phase are linearly aligned, which is the boundaries of former particles. Other than that, platelet grains are uniformly distributed surrounded by brightly imaging intergranular phase. Darkly imaging particles are $Nd_2Fe_{14}B$ grains, and their particle size appears to be bimodal because of the presence of abnormal grown grains (indicated by the arrows in Fig. 5-2(b) induced by the high heat treatment temperature. The presence of abnormally grown grains explains the appearance of the higher susceptibility region in the initial magnetization curve in Fig. 5-1. Fig. 5-2 (c) shows the BSE-SEM image of the Dy-vapor diffusion-processed magnet. It exhibits distinct difference with substantially coarsened grain structure after the Dy vapor diffusion process at 900 ^{o}C which is the required

temperature of the conventional Dy-vapor diffusion process [4]. This result shows that the conventional Dy-vapor diffusion process is not applicable to the hot-deformed magnets. Therefore, the eutectic diffusion process is the only method that can be applied to hot-deformed magnets for enhancing the coercivity.

Fig. 5-3 shows the STEM EDS mapping results observed from the $Nd_{62}Dy_{20}Al_{18}$ diffusion-processed sample, with in the c-axis in-plane upward direction. The selected peaks for the EDS mapping are Nd *L*α, Fe *K*α, Co *K*α Al *K*α and Dy *M*α. Depletion of Fe and enrichment of Nd, Dy as well as Co and Al can be observed in the intergranular phase. Dy is mainly partitioned in the intergranular phase, but the area where Dy substitute part of Nd of the $Nd_2Fe_{14}B$ phase can be seen in the superimposed image of Dy and Nd mappings. The Dy-rich shell structure, which is invisible in SEM observation, can now be clearly observed. The Dy-rich shell does not envelop the $Nd_2Fe_{14}B$ grains but mainly forms at the side surfaces of the $Nd_2Fe_{14}B$ grains. No Dy-substituted region can be seen on the flat surface of the platelet $Nd_2Fe_{14}B$ grains. Note that the region selected for TEM characterization is near the center of the sample, indicating that this kind of microstructure is not limited to the surface region of the sample. This also suggests the diffusion depth of Nd-Dy-Al alloy has to be significantly larger than 1.0 mm, which is very remarkable for the annealing temperature of 700°C. Inhomogeneous distribution of Al indicates the eutectic decomposition of the grain boundary phase during cooling since the EDS profile quantification analysis (not shown) suggests Al-lean region is either metallic Nd or Nd_3Co phase and Al-rich region has the composition close to $Nd_{82}Al_{18}$ compound.

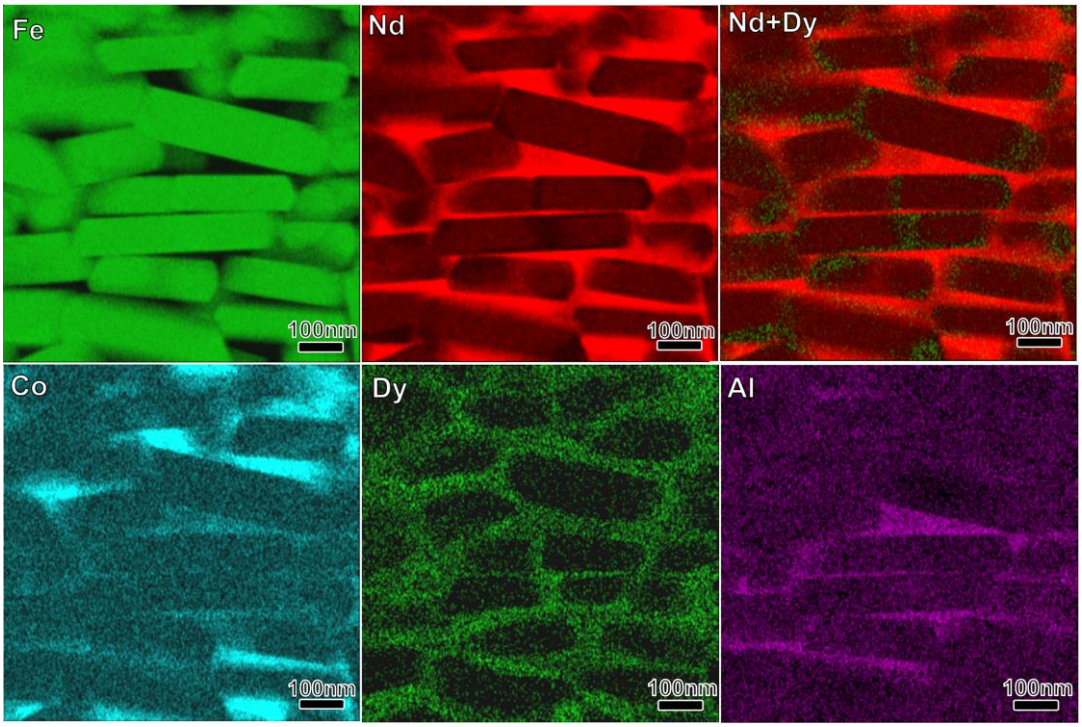

Fig. 5-3 BSE SEM images of the hot-deformed a), $Nd_{62}Dy_{20}Al_{18}$ diffusion b) and Dy-vapor diffusion-processed magnets c), with c-axis in-plane.

In order to examine the chemical composition of the intergranular phase as well as to detect the Dy concentration within the shell structure, detailed analysis was carried out for several types of interfaces with different features, as shown in Fig.5-4 (a). From the overlaid EDS map of Nd and Dy elemental distribution, Dy-rich shell structure can be observed on both side surfaces and c-plane of the $Nd_2Fe_{14}B$ grains (Fig. 5-4(b)), in which the rectangles are selected for later EDS line scan analysis, as shown in Fig. 5-4 (e) and (f). Fig. 5-4 (c) and (d) displays the magnified HAADF STEM image of side Dy-rich layer from region 1 and 2, respectively. The $Nd_2Fe_{14}B$ grain in Fig.5-4(c) is aligned in <100> zone-axis (inset image shows the

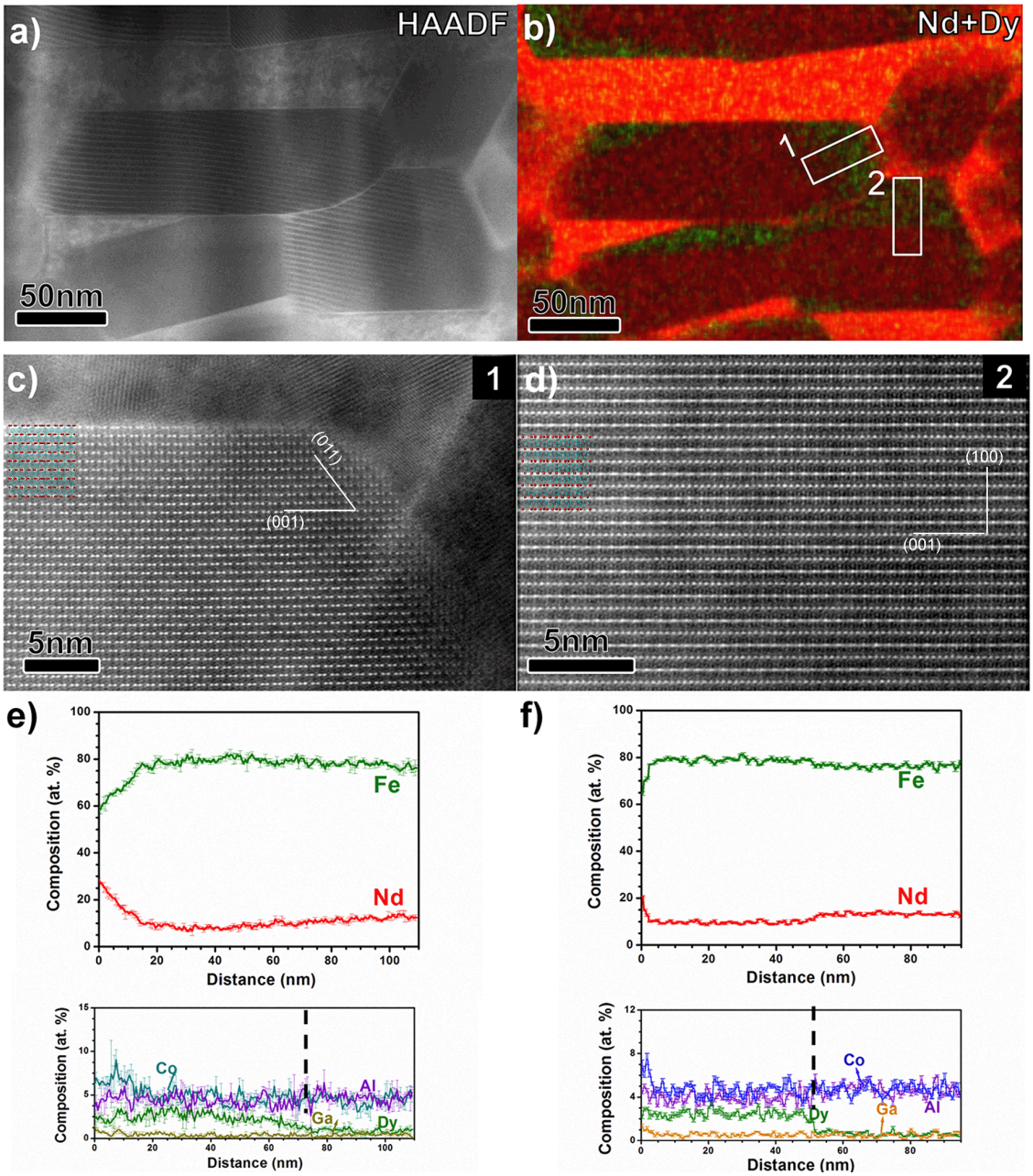

Fig. 5-4 HAADF-STEM image of Nd-Dy-Al diffusion-processed sample (a), superimposed EDS mapping image of Nd and Dy of with c-axis in-plane (b), magnified STEM image of side Dy-rich layer from region 1 (c) and Dy-rich shell on c-plane from region 2 (d), line-scan profile from selected region 1 and 2 (e),(f) in the Nd+Dy map.

schematic projection of $Nd_2Fe_{14}B$ grains in <100> direction). The HAADF STEM image here doesn't show directly the crystallographic position of Dy atoms. Fig. 5-4 (d) shows the HAADF-STEM image of $Nd_2Fe_{14}B$ grain from region 2 taken from <-110> zone-axis, indicating the core-shell interface here is faceted with (001) plane which is quite rare in this work.

In this case, we can resolve the core-shell interface from the HAADF STEM image directly; Dy-rich layer appears to be brighter in the top part of this image as Dy atoms are heavier scatters to the HAADF detector.

The EDS line-scan was carried out along the rectangle regions in Fig. 5-4 (b), the resulting elemental profiles are shown in Fig. 5-4 (e) and (f) where the dashed line in the lower profile indicated the Dy core-shell interface. In both line profiles, Co profile climbs higher at the interface between Nd-rich intergranular phase and $Nd_2Fe_{14}B$ phase then turns to be constant value in 2:14:1 phase, indicating Co tends to segregate at the interface. Dy profile shows uniform distribution crossing the interface between 2:14:1 phase and Nd-rich phase. Due to high diffusivity of Al atom in the 2:14:1 phase, Al appears to be homogeneously distributed ongoing to the inner side of $Nd_2Fe_{14}B$ grains. Dy profile exhibits two different patterns at the shell-core interface. It shows small gradient at the interface of side Dy-rich shell structure, however, a sharp drop at the interface of the c-plane Dy-rich shell structure. This implies two possible mechanisms of formation of Dy-rich shell structure with different faceting relationship with 2:14:1 phase. In most cases, where Dy atoms substitute Nd atoms on higher-index planes rather than (001) plane, diffusion of Dy atoms into the $Nd_2Fe_{14}B$ phase by substitution for Nd atoms is motivated by the gradient in Dy concentration, which induces a gradual change of Dy concentration crossing the core-shell interface. For those cases where Dy-rich shell appears on the c-plane of $Nd_2Fe_{14}B$ grains, as shown in rectangle 2 in Fig. 5-4(b), the sharp interface between $(Nd,Dy)_2Fe_{14}B$ phase and $Nd_2Fe_{14}B$ phase indicates the formation of Dy-rich shell is a second-order phase-transition process which would presents a discontinuity in the concentration change. And in this case, we would like to address the mechanism as the so-called reaction-diffusion process. EDS profiles suggest that the average Dy content in the shells is around 3 at.% and lower than 1 at.% in cores. Al shows around 4 at.% distribution in the $Nd_2Fe_{14}B$ phase.

5.3.3 Discussion

The work has shown that by $Nd_{62}Dy_{20}Al_{18}$ diffusion process, the intergranular phase has been modified to be Nd-rich and depleted in Fe and Co. Besides, the areal fraction and thickness of Nd-rich both increase after the diffusion process; Dy-rich layers also form on the surface of $Nd_2Fe_{14}B$ grains.

In this work, the eutectic grain boundary diffusion process using Dy-containing alloys has also been compared the conventional Dy-vapor diffusion process. The excessively high heat treatment temperature required to vaporize Dy that used in Dy-vapor diffusion process will lead to severe grain growth and extremely inhomogeneous grain size distribution which is detrimental to the coercivity of the hot-deformed Nd-Fe-B magnets.

Watanabe et al [10] reported the grain boundary diffusion process for hot-deformed magnet using eutectic $Dy_{70}Cu_{30}$ alloy. Instead, the diffusion process was done by blending powder of $Nd_2Fe_{14}B$ alloy and Dy-Cu alloy followed by hot-pressing and hot-deformation. Due to the segregation of ferromagnetic element in the intergranular phase, the coercivity in their work was limited to 2.0 T. Sepehri-Amin *et al*. [6] later introduced the eutectic grain boundary diffusion process by using $Nd_{60}Dy_{20}Cu_{30}$ alloy as the diffusion source, succeeding in modifying the intergranular phase to be non-ferromagnetic and introducing thin Dy-rich shell localized on the surface of $Nd_2Fe_{14}B$ grains. They could achieve the coercivity value of 2.6 T after diffusion process, though at the expanse of remanence drop from 1.4 T to 1.1 T. In this work, we can reach around 2.8 T for coercivity with remanence decrease from 1.50 T to 1.27 T. If we compare the magnetic properties of the Nd-Dy-Al diffusion-processed magnet in this work to other commercial sintered magnets containing different Dy contents (shown in Fig. 5-6 [11, 12]), it can be seen that while the remanence value is comparable to the sintered magnets that contain about 4 wt.% Dy, the coercivity achieved in this work is much higher than 2.3 T that can be reached in sintered magnets. In addition, the average Dy concentration in the Nd-Dy-Al diffusion-processed magnet, analyzed by ICP-OES is estimated to be 1.38 wt.%. This demonstrates the superiority in coercivity enhancement of the eutectic grain boundary diffusion process using Nd-Dy-Al alloys for hot-deformed magnet to conventional HRE grain boundary diffusion process.

The coercivity enhancement in this work can be attributed to the better magnetic isolation formed by the thicker non-ferromagnetic Nd-rich intergranular phase and the formation of localized Dy-rich shell structure at the surface of $Nd_2Fe_{14}B$ grains. The average Dy concentration in the shell of the Nd-Dy-Al diffusion-processed magnet is close to 3 at.%; it is higher than what has been reported concentration, 1.07 at.%, in Dy shells of the sintered magnets by Dy vapor diffusion process [13].

The Co segregation found at the interface between Nd-rich intergranular phase and the 2:14:1 phase was believed to be able to cause the distortion to the $Nd_2Fe_{14}B$ crystal, thus results in a reduction to the magnetocrystalline anisotropy field, especially to the very surface of the $Nd_2Fe_{14}B$ grains [14].

Around 4 at% Al can be detected in the $Nd_2Fe_{14}B$ phase of the Nd-Dy-Al diffusion-processed magnet. Previous study has calculated that Al segregation in the Nd-Fe-B structure has similar effect as that of Dy substitution for Nd [15]. Al substitutes for Fe and $Nd_2(Fe,Al)_{14}B$ shows smaller saturation magnetization than $Nd_2Fe_{14}B$ but a higher magnetocrystalline anisotropy. This is likely the reason why Nd-Dy-Al diffusion-processed magnet appears to have higher coercivity than Nd-Dy-Cu diffusion-processed magnet.

5.3.4 Conclusion on Nd-Dy-Al GBDP

By applying the eutectic grain boundary diffusion process using $Nd_{62}Dy_{20}Al_{18}$ alloy, the coercivity of hot-deformed Nd-Fe-B magnets was enhanced to 2.8 T at room temperature, with a remanence value of 1.30 T. The Nd-Dy-Al diffusion-processed magnet retains the coercivity of 0.75 T at 200 ^{o}C, which is very much close to the requirement for application in traction motors. On the other hand, Dy-vapor diffusion-processed Nd-Fe-B hot-deformed sample suffers significant grain growth, leading to a catastrophic degradation in coercivity. ICP analysis shows overall Dy concentration in the Nd-Dy-Al diffusion-processed sample is only

1.38 wt%. This eutectic grain boundary diffusion process using Nd-Dy-Al alloy is very promising for the development of Dy-free or Dy-saving Nd-Fe-B permanent magnet with high coercivity.

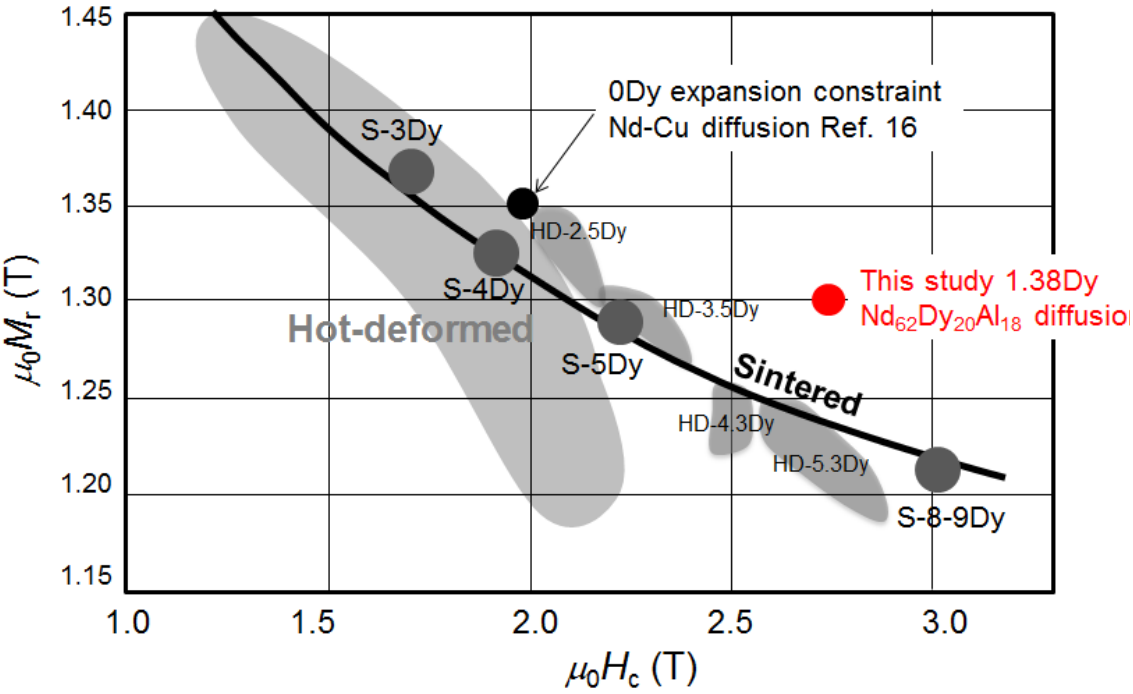

Fig. 5-5 Benchmarking of magnetic properties of the Nd-Dy-Al diffusion-processed hot-deformed magnet with commercial sintered magnets with different Dy contents (in weight percent).

5.4 Coercivity enhancement of hot-deformed Nd-Fe-B magnets by the eutectic GBDP using Nd-Tb-Cu alloys

5.4.1 Melting point comparison

The melting temperature of $Nd_{60}Tb_{10}Cu_{30}$ and $Nd_{60}Tb_{20}Cu_{20}$ ribbons were measured by DTA and for comparison, we also prepared the ternary $Tb_{70}Cu_{30}$ eutectic ribbons. The merged heating curves of the three alloys are shown in Figure 5-6. Considering the influence of heating rate, the melting temperature is decided from the onset of the peak as 524°C, 571°C and 740°C for $Nd_{60}Tb_{10}Cu_{30}$, $Nd_{60}Tb_{20}Cu_{20}$ and $Tb_{70}Cu_{30}$ ribbons, respectively. By alloying Tb in the low melting-point $Nd_{70}Cu_{30}$ eutectics, the ternary Nd-Tb-Cu eutectics exhibit much lower melting temperature, which makes them a proper diffusion source that can be applied to the eutectic GBDP on hot-deformed magnets. We can note the heating curve of $Nd_{60}Tb_{10}Cu_{30}$ is not very smooth. This comes from the fluctuation in Ar flow during the measurement.

5.4.2 Magnetic properties

Figure 5-7(a) shows the hysteresis loops of $Nd_{60}Tb_{10}Cu_{30}$ and $Nd_{60}Tb_{20}Cu_{20}$ diffusion-processed magnets. The designed weight gain of the magnets is 10%, however, this does not stand for the real weight increment after the diffusion process since the very surface of the diffusion-processed magnets is removed by ~50μm and part of the applied Nd-Tb-Cu ribbon loses as result of the diffusion into the molybdenum foil which was

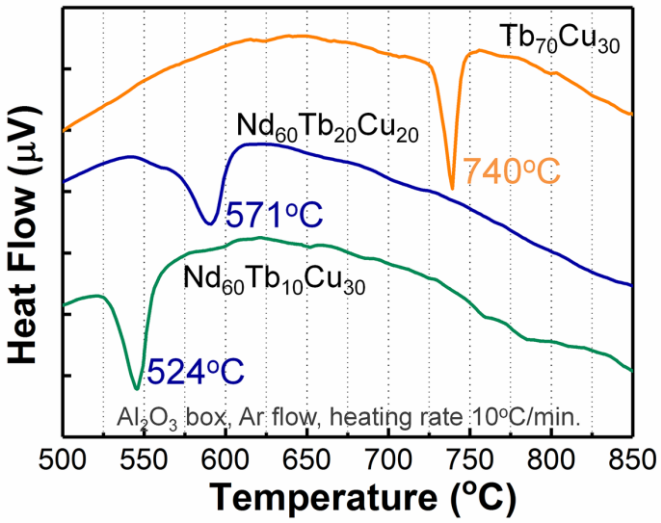

Fig. 5-6 Heating curves on DTA of $Nd_{60}Tb_{10}Cu_{30}$, $Nd_{60}Tb_{20}Cu_{20}$ and $Tb_{70}Cu_{30}$ ribbons.

used as the holder for heat-treatment. The coercivity ($\mu_0 H_c$) of the hot-deformed magnet was increased from 0.87 T to 2.36 T for $Nd_{60}Tb_{10}Cu_{30}$ diffusion-processed magnet, and 2.57 T for $Nd_{60}Tb_{20}Cu_{20}$ diffusion-processed magnet, while the remanent magnetization did not significantly degrade which was seen for Nd-Dy-Al diffusion process. The remanence dropped from 1.50 T to 1.44 T and 1.38 T, respectively. The two-step S-shaped initial magnetization curves of the diffusion-processed magnets are typical feature of the pinning-dominant magnetization process. The depinning field derived from the deviation of the initial magnetization curve indicates 0.72 T, 2.22 T and 2.46 T for the hot-deformed, $Nd_{60}Tb_{10}Cu_{30}$ and $Nd_{60}Tb_{20}Cu_{20}$ diffusion-processed magnets, respectively, which shows a good consistence with their coercivities.

Figure 5-7 (b) shows temperature dependence comparison between various diffusion-processed magnets. Temperature coefficient of coercivity (β) for the hot-deformed, and the $Nd_{60}Tb_{10}Cu_{30}$ and $Nd_{60}Tb_{20}Cu_{20}$ diffusion-processed samples was calculated to be -0.478, -0.379 and -0.315%$^{o}C^{-1}$, respectively. This indicates a significant improvement in the temperature coefficient of coercivity by the Nd-Tb-Cu diffusion process, especially with using $Nd_{60}Tb_{20}Cu_{20}$ as diffusion source. The $Nd_{60}Tb_{20}Cu_{20}$ diffusion-processed magnet shows $\mu_0 H_c$ of 1.43 T at 150 ^{o}C while $Nd_{60}Tb_{10}Cu_{30}$ diffusion-processed magnet exhibits only 1.06 T at 150 ^{o}C. Despite the Nd-Dy-Al diffusion-processed magnet shows a highest coercivity of 2.8 T at room temperature, temperature coefficient of its coercivity was -0.39%/$^{o}C^{-1}$ as described in Chapter 5.3.1. $Nd_{60}Tb_{10}Cu_{30}$ diffusion-processed magnet performs a slightly better thermal stability in comparison with Nd-Cu diffusion-processed magnet whereas $Nd_{60}Tb_{20}Cu_{20}$ diffusion-processed magnet displayed the superior temperature dependence over all other diffusion-processed magnets.

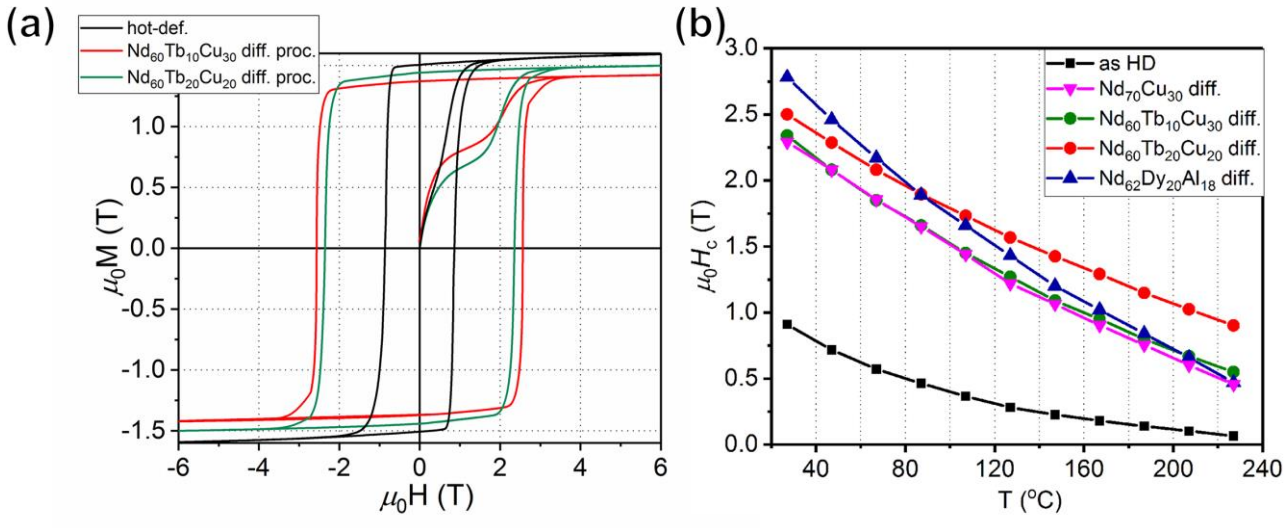

Fig. 5-7 (a) Hysteresis loops of the hot-deformed, $Nd_{60}Tb_{10}Cu_{30}$, and $Nd_{60}Tb_{20}Cu_{20}$ diffusion-processed magnets; (b) temperature dependence of coercivity of the hot-deformed, $Nd_{60}Tb_{10}Cu_{30}$, and $Nd_{60}Tb_{20}Cu_{20}$ diffusion-processed magnets, in comparison with Nd-Cu (Chapter 3) and Nd-Dy-Al (Chapter 5.3.1) diffusion-processed magnets.

5.4.3 Microstructures of Nd-Tb-Cu diffusion-processed magnets

a) Comparison of the overall microstructure of $Nd_{60}Tb_{10}Cu_{30}$, and $Nd_{60}Tb_{20}Cu_{20}$ diffusion-processed magnets

Figure 5-8 are the backscattered electron SEM images of surface and center regions of $Nd_{60}Tb_{10}Cu_{30}$ (a, c), and $Nd_{60}Tb_{20}Cu_{20}$ (b, d) diffusion-processed magnets. The observation was carried out to regions close to the sample surface with the c-axis in plane. The brightly-imaged region refers to the Nd-rich intergranular phase, which can be observed preferentially exist on the flat surface of the $Nd_2Fe_{14}B$ grains. Calculation of the areal fraction of the Nd-rich intergranular phase based on the difference in the image contrast shows a decrease from 18 % to 8 % going from surface to center regions for $Nd_{60}Tb_{10}Cu_{30}$ diffusion-processed sample. In the case of $Nd_{60}Tb_{20}Cu_{20}$ diffusion-processed sample, it changes from 14 % to 7 % from surface to center. It can be observed that most of the $Nd_2Fe_{14}B$ grains retain in alignment with c-axis parallel to the easy axis for both samples. At current magnification (50kX, with a pixel size of 14.7 nm) no core-shell structure can be confirmed.

b) Chemistry and microstructure of $Nd_{60}Tb_{10}Cu_{30}$ diffusion-processed sample analyzed by TEM

Fig. 5-9 (a) is the BF-TEM image of $Nd_{60}Tb_{10}Cu_{30}$ diffusion-processed sample. The different contrasts which vary from black to grey and to white come from the different orientations of the $Nd_2Fe_{14}B$ grains, known as phase contrast in bright-field mode of TEM. We can also note that most of the $Nd_2Fe_{14}B$ grains are free of strain contrast at the interface with Nd-rich intergranular phases. The highly-textured $Nd_2Fe_{14}B$ phase

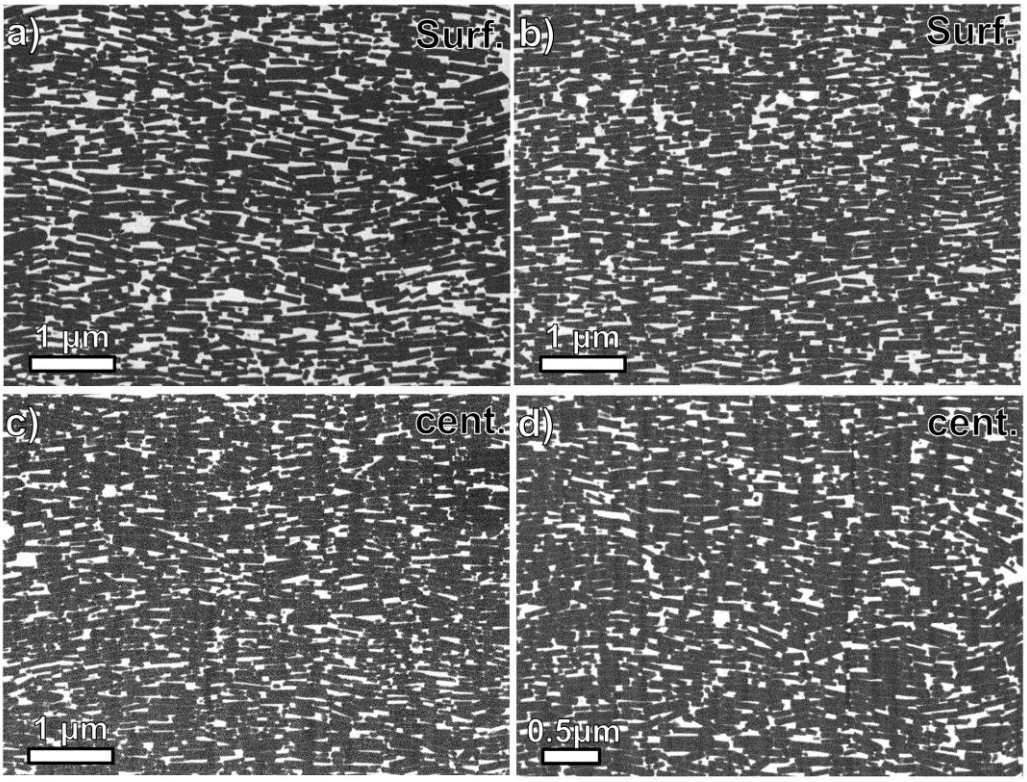

Fig. 5-8 BSE-SEM images of surface and center regions of $Nd_{60}Tb_{10}Cu_{30}$ (a, c), and $Nd_{60}Tb_{20}Cu_{20}$ (b, d) diffusion-processed magnets.

can again be observed which gives one of the reasons for the small deterioration in remanent magnetization from initial hot-deformed magnet. Figure 5-9 (d) displays the HAADF-STEM image and the elemental maps of Nd, Fe, Co, and Ga (b, c, e, f) taken from the same area. Figure 5-10 (b) is a superimposed image of Fe and Tb maps, with Fe displayed in sky-blue and Tb in red. Enrichment of Nd, Ga, Tb and depletion of Fe can be observed. Co shows almost uniform distribution over the whole area across the matrix phase and the intergranular phase. The HAADF-STEM image (Fig. 5-10 (d)) and the overlapped Fe and Tb mapping result are not showing pronounced core-shell structure. The Nd-rich intergranular phase has the thickness of some nanometers and in a few cases they formed with the thickness of about 30 nm. This is not quite consistent with that observed by SEM as aforementioned although both were from the surface region of the sample. It is considered because of the non-uniform distribution of the Nd-rich intergranular phase and the limited sampling size of TEM characterization. To quantitatively study the Nd and Tb distribution in the grain boundaries, detailed EDS and TEM investigations were performed. Figure 5-10 shows the results of EDS line-scan analysis performed across the interface between $Nd_2Fe_{14}B$ grains and the grain boundary phase. Region (a) and (b) compares different crystallographic planes on which the grain boundary phase is located. When the Nd-rich grain boundary phase forms on the flat surface perpendicular to c-axis of $Nd_2Fe_{14}B$ grain, the Nd concentration shows ~50 at.% in contrast to ~30 at.% for that locates on the side plane which is parallel to the c-axis.

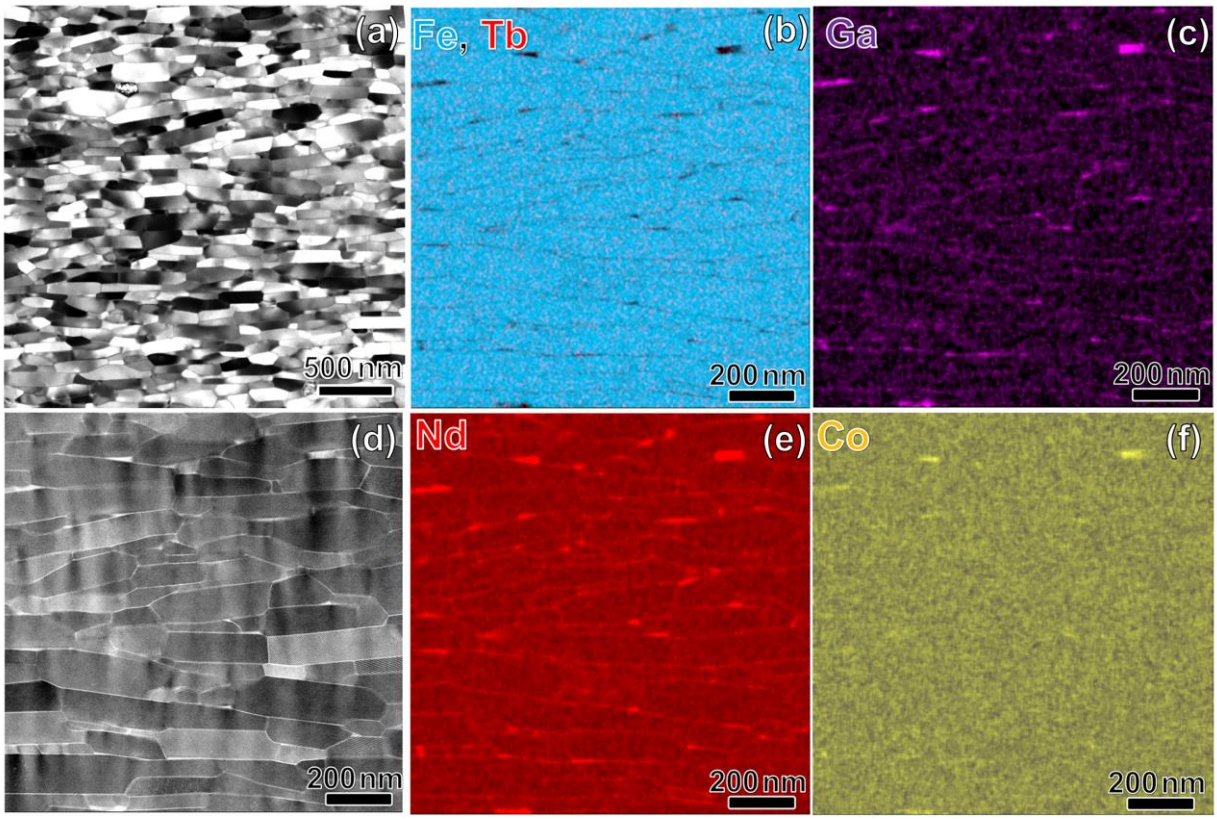

Fig. 5-9 BF-TEM image (a), HAADF-STEM image (d) and EDS elemental maps of Nd, Ga, Co maps from the same region in (d). (b) Shows the superimposed image of Fe and Tb elemental maps.

The Tb content also shows similar behavior. It has ~3 at.% enrichment in the grain boundary phase for region (a) while the concentration is within noise level for region (b). In region (c) where we have thicker grain boundary (in 3-5 nm), the Nd concentration shows close to 75 at.% and Tb content is similar with that observed for the grain boundary phase in region (a). It can also be noticed that Tb line-scan profile displays a broadened feature from the grain boundary to the interior of $Nd_2Fe_{14}B$ grains. This is due to the formation of the several atomic layers of Tb-rich shell which can also be directly observed from the corresponding HAADF-STEM. In fact, the substitution of Nd for Tb only happened at the (001)-plane Nd termination layer in region (a) and (c) and the (110) Nd termination layer in region (b). From the line-scan profile, we can also confirm that only trace amount of Tb exists in the inner region of $Nd_2Fe_{14}B$ grains. The localization of Tb at the very surface of the $Nd_2Fe_{14}B$ grains offers another microstructural evidence for the small deterioration in remanent magnetization of $Nd_{60}Tb_{10}Cu_{30}$ diffusion-processed sample.

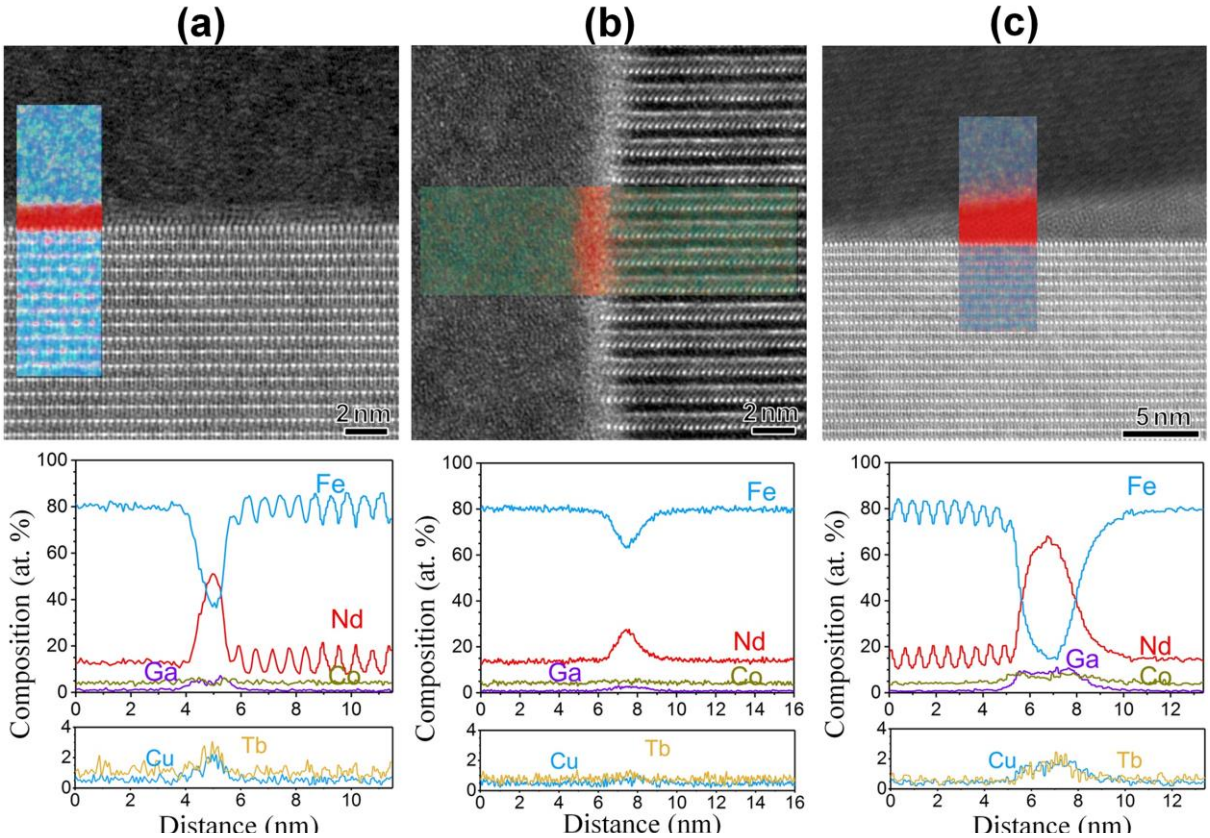

Fig. 5-10 EDS and STEM analysis for the grain boundary phase in $Nd_{60}Tb_{10}Cu_{30}$ diffusion-processed sample.

c) Chemistry and microstructure of $Nd_{60}Tb_{20}Cu_{20}$ diffusion-processed sample analyzed by TEM

The same characterization was also carried out to $Nd_{60}Tb_{20}Cu_{20}$ diffusion-processed sample. The BF-TEM image is showing clear feature of strain contrast within $Nd_2Fe_{14}B$ grains. This is believed to originate from the lattice misfit between the intergranular phase and matrix phase. We can also note that most of the $Nd_2Fe_{14}B$ grains stay with high-order alignment along the easy-axis of the magnet. Formation of thick Nd-rich intergranular phase which also shows enrichment of Tb can be observed with the STEM characterization from the EDS elemental maps. It can be noted the surface region especially at the side surface of $Nd_2Fe_{14}B$ grains shows Nd depletion and appear darker. Combined with the superimposed Tb and Nd maps, this is confirmed to come from the substitution for Tb. Instead of a total envelope around $Nd_2Fe_{14}B$ grains, Tb-rich shell can be observed preferentially at the side or high-index plane of $Nd_2Fe_{14}B$ grains. The thickness of shell is also showing a non-uniform distribution. At current magnification, shells with the thickness ranging from 20 to 50 nm could be resolved. Co is no long performing a homogeneous distribution as that was observed in $Nd_{60}Tb_{10}Cu_{30}$ diffusion-processed sample. Similar with Ga and Cu, at least two different contrasts can be distinguished from the EDS maps. Besides, the partition behavior of Ga, Cu and Co is different from each other which are considered as the product of phase decomposition during the solidification of the liquid intergranular phases.

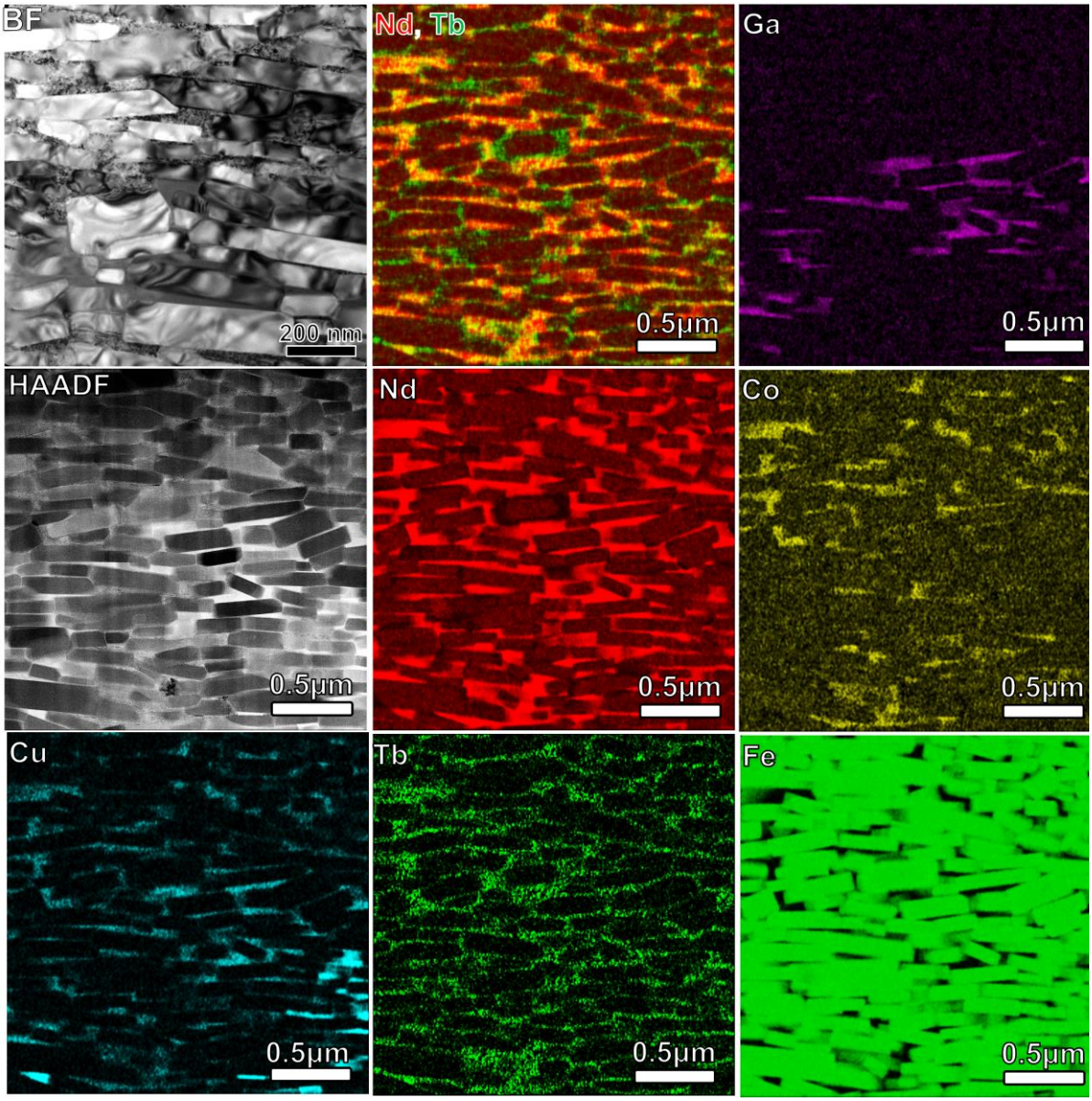

Fig. 5-11 BF-TEM, HAADF-STEM images of $Nd_{60}Tb_{20}Cu_{20}$ diffusion-processed sample and EDS elemental maps of Nd-L_α, Fe-K_α, Ga-K_α, Tb-M_α, Cu-K_α, Co-K_α taken from the very same region in the HAADF image.

To study the mechanism involved in the formation of Tb-enriched shells, EDS line-scan and STEM analysis have been carried out. Figure 5-12 indicates the results of EDS mapping and line-scan analysis performed within the shell regions. The EDS line scan shows that both Tb and Nd content remain constant within in the shell. Thus the formation of Tb-enriched shell is not likely by the bulk or volume diffusion mechanism and supports the model proposed in the report [13] in which they suggest the melting of the very surface regions of the $Nd_2Fe_{14}B$ grains and Dy-rich shell formed through solidification from the Nd and Dy enriched liquid system.

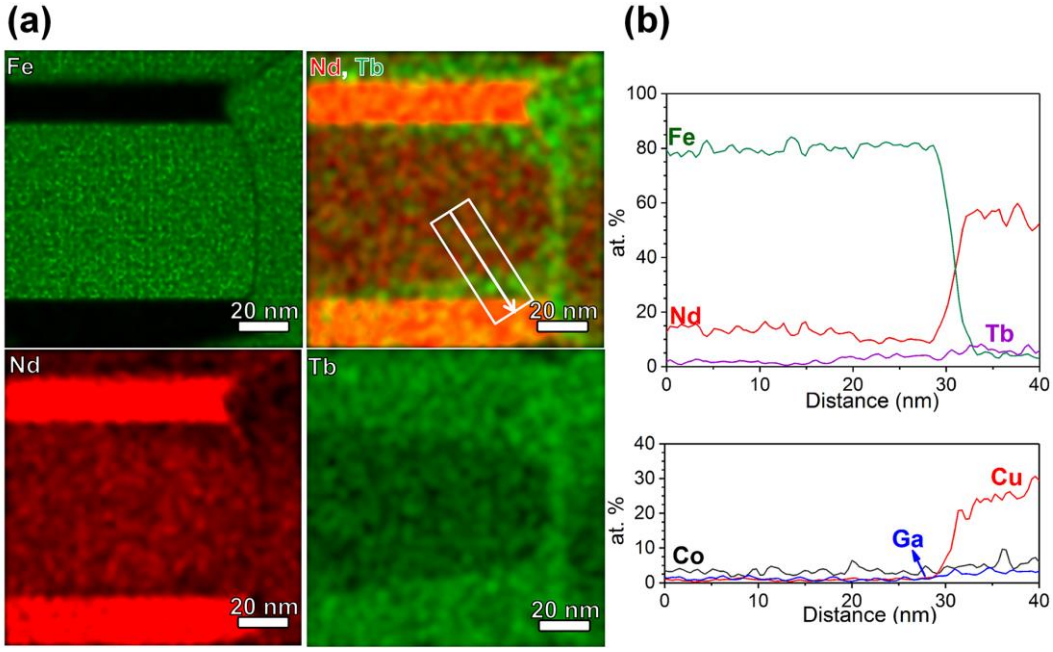

Fig. 5-12 BF-TEM, HAADF-STEM images of $Nd_{60}Tb_{20}Cu_{20}$ diffusion-processed sample and EDS elemental maps of Nd-L_α, Fe-K_α, Ga-K_α, Tb-M_α, Cu-K_α, Co-K_α taken from the very same region in the HAADF image.

5.4.4 Discussion

The work has shown that by Nd-Tb-Cu diffusion process, the coercivity of the hot-deformed Nd-Fe-B magnets can be improved without much sacrifice of remanent magnetization. $Nd_{60}Tb_{10}Cu_{30}$ diffusion-processed processed sample shows the coercivity of 2.36 T with a remanence of 1.44 T. On the other hand, $Nd_{60}Tb_{20}Cu_{20}$ diffusion process realized the enhancement of coercivity to 2.57 T with the remanence of 1.38 T.

No pronounced Tb-shell structure was observed for $Nd_{60}Tb_{10}Cu_{30}$ diffusion-processed sample. Modification of the very surface layer of $Nd_2Fe_{14}B$ grains by Tb substitution without diffusion to the inner region is one of the reasons for the small deterioration of remanence after $Nd_{60}Tb_{10}Cu_{30}$ diffusion. The enhancement in the magnetocrystalline anisotropy field along with this Tb substitution is believed to be able to suppress the nucleation of reverse domains at low magnetic field.

Anisotropic distribution of Tb-rich shell was shown by the STEM-EDS mapping result for $Nd_{60}Tb_{20}Cu_{20}$ diffusion-processed samples. This is a similar observation as has been described in Nd-Dy-Al diffusion process. However, $Nd_{60}Tb_{20}Cu_{20}$ diffusion-processed sample exhibits a superior thermal stability in terms of coercivity. Despite the smaller coercivity at room temperature, it retains the coercivity of 1.43 T at 150^{o}C, in comparison with 1.12 T for Nd-Dy-Al diffusion-processed sample. This is considered to be originated from the formation of Tb-rich shell since the anisotropic field of $Tb_2Fe_{14}B$ phase demonstrates much better temperature dependence than that of $Nd_2Fe_{14}B$ phase.

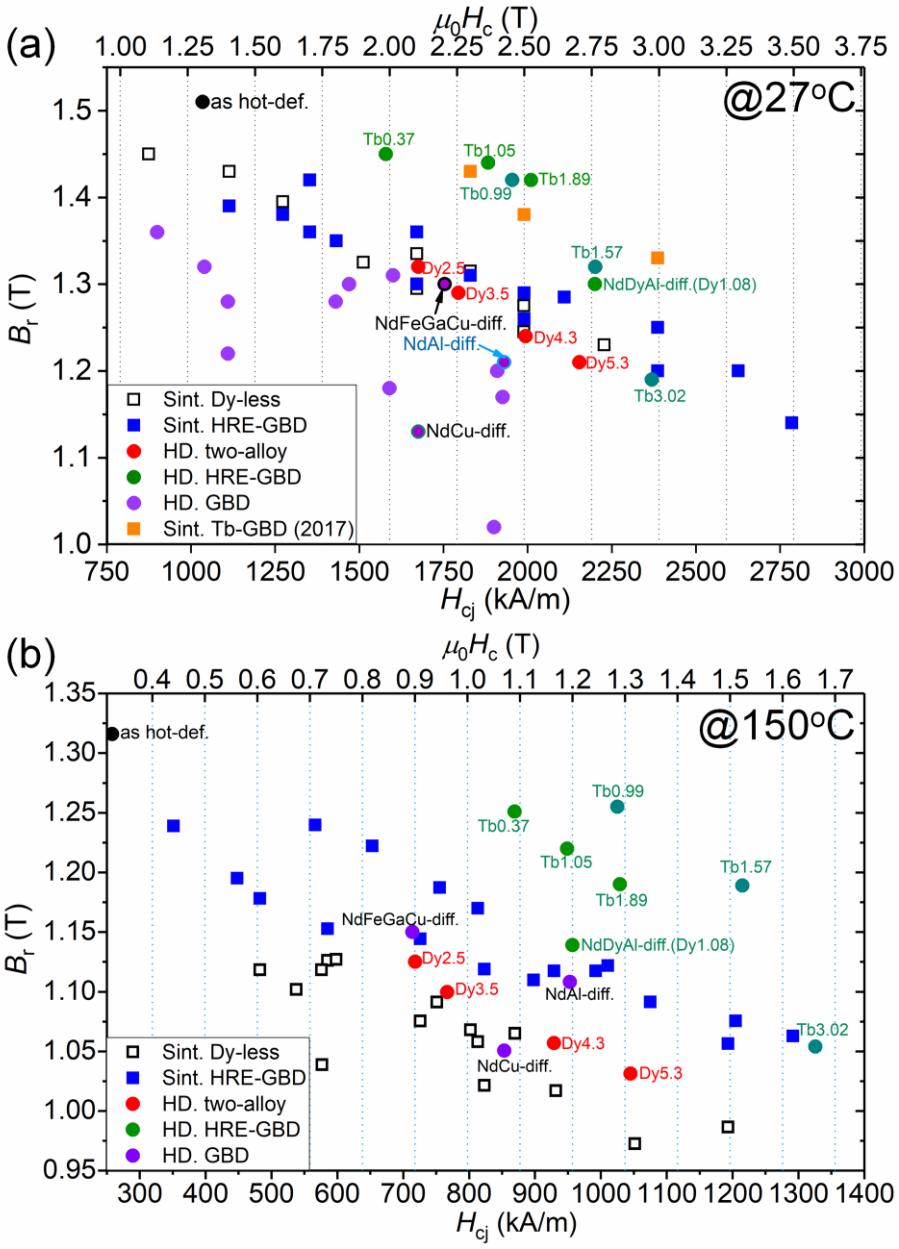

Fig. 5-13 Benchmark of magnetic properties including the commercial HRE-free, HRE GBD processed sintered magnets and the GBD processed hot-deformed magnets, composed with the coercivity and remanent magnetization both measured at 27°C (a) and 150°C (b).

The average Tb concentration analyzed by ICP-OES is 1.05 wt.% for the $Nd_{60}Tb_{10}Cu_{30}$ diffusion-processed sample and 1.57 wt.% for the $Nd_{60}Tb_{20}Cu_{20}$ diffusion-processed sample. If we take the benchmark as shown in Figure 5-13 which is comprised with HRE-free commercial sintered magnets and those with Dy or Tb GBD processed sintered magnets from the major magnet makers in Japan (Hitachi Matals, Shinetsu Chemical, TDK et al), to compare the magnetic properties that are achieved by the eutectic grain boundary diffusion processes, we can note that the Nd-Tb-Cu diffusion processed magnets possess superior properties over the current grade of sintered magnets. However, since the information of Dy or Tb content in these magnets remains confidential, it's difficult to make arbitrary comment as Nd-Tb-Cu eutectic grain boundary diffusion process makes more sufficient use of Tb.

The coercivity enhancement is estimated to be 1132 kA/m per weight % of the use of Tb with the $Nd_{60}Tb_{10}Cu_{30}$ as the diffusion source, and this value decreases to 864 kA/m in the case of $Nd_{60}Tb_{20}Cu_{20}$ diffusion process. Reasons for this are considered as the waste of Tb due to the volume diffusion into the $Nd_2Fe_{14}B$ grains that are not make effective contribution to the enhancement in coercivity since the average content is very low. Moreover, the non-uniform formation Tb-rich shells in the aspects the thickness variations as well as their distributions also limited further improvement of coercivity.

The most attracting perception of the Nd-Tb-Cu diffusion process lies in the supreme thermal stability of the $Nd_{60}Tb_{20}Cu_{20}$ diffusion-processed magnet with the temperature coefficient of coercivity β of -0.315%/^{o}C. In contrast, the typical value of the sintered magnets ranges from -0.5~0.6 %/^{o}C. The merit of improved thermal stability in terms of temperature dependence of coercivity of the Nd-Tb-Cu diffusion-processed magnets could be more manifest if the benchmark is taken with sintered magnets those are processed by two-alloy method as well as conventional HRE-grain boundary diffusion process (Fig. 5-13). When the comparison is taken for the magnetic properties measured near R.T., in this case 27 ^{o}C, Nd-Tb-Cu diffusion-processed magnets exhibit comparable properties as those of HRE-GBD processed sintered magnets (Fig. 5-13 (a)). However, comparing the magnetic properties measured at 150^{o}C revealed the fact that Nd-Tb-Cu diffusion-processed hot-deformed magnets demonstrated superior properties to those of sintered magnets, due to their obviously smaller temperature dependence of coercivity. This would enable the Nd-Tb-Cu grain boundary diffusion process a feasible technique to develop the HRE-saving high-performance hot-deformed Nd-Fe-B permanent magnets. Further effort is necessary to make optimization to minimize Tb utilization while realizing the coercivity of 1.0 T at 150^{o}C.

5.4.5 Conclusion on Nd-Tb-Cu GBDP

By applying the eutectic grain boundary diffusion process using Nd-Tb-Cu alloys, the coercivity hot-deformed Nd-Fe-B magnets was enhanced from 0.87 T to 2.35 T and 2.57 T for $Nd_{60}Tb_{10}Cu_{30}$ and $Nd_{60}Tb_{20}Cu_{20}$, with a small degradation in remanence from 1.50 T to 1.44 T and 1.38 T, respectively. In the meanwhile, the temperature coefficient of coercivity β was improved from -0.478 %^{o}C^{-1} to -0.379 and -0.315 %^{o}C^{-1}, respectively. This eutectic grain boundary diffusion process using Nd-Tb-Cu alloy is a feasible technique to develop the high-performance (with $\mu_0 H_c$ >1.0 T @150^{o}C, $\mu_0 M_r$ >1.3T @R.T.) hot-deformed Nd-Fe-B permanent magnets and it is also possible to extend the application of this method to sintered magnets.

5.5 Conclusion

In this chapter, the Dy and Tb alloyed diffusion sources have been applied in the eutectic grain boundary diffusion process on the hot-deformed Nd-Fe-B magnets. Major conclusions from the work of this chapter are listed as below,

(1) Alloying HREEs such as Dy, Tb et al to the low melting-point Nd-rich eutectics to form a ternary eutectic alloy is the only way to apply the HRE GBDP to the hot-deformed Nd-Fe-B magnets;

(2) Utilization the ability of formation of Dy or Tb-enriched shell structures, the applied amount of diffusion sources can be reduced to a large extent. This leads to the limited degradation of remanence which results from the formation of Nd-rich intergranular phases in the diffusion processed magnets;

(3) $Nd_{60}Tb_{20}Cu_{20}$ diffusion-processed magnet shows superior thermal stability to current commercial sintered magnets and the hot-deformed magnets processed with other diffusion sources. This makes $Nd_{60}Tb_{20}Cu_{20}$ an optimal diffusion source to apply in the eutectic GBDP for realizing our targeted magnetic properties.

References

[1] S. Hirosawa, Y. Matsuura, H. Yamamoto, S. Fujimura, M. Sagawa, and H. Yamauchi, "Magnetization and magnetic anisotropy of R2Fe14B measured on single crystals," *J. Appl. Phys.*, vol. 59, no. 3, pp. 873-879, Feb. 1986.

[2] K. Park, K. Hiraga, and M. Sagawa, "Effect of metal-coating and consecutive heat treatment on coercivity of thin Nd-Fe-B sintered magnets," REPM Proceedings of 16th International Workshop on RE Magnets and their Applications, *The Japan Institute of Metals*, Sendai, Japan, pp. 257-264, 2000.

[3] M. Komuro, Y. Satsu, and H. Suzuki, "Increase of coercivity and composition distribution in fluoride-diffused NdFeB sintered magnets treated by fluoride," IEEE Trans. Magn. vol. 46, no. 11, pp. 3831-3833, Nov. 2010.

[4] H. Suzuki, Y. Satsu, and M. Komuro, "Magnetic properties of a Nd-Fe-B sintered magnet with Dy segregation," *J. Appl. Phys.* , vol. 105, no. 7, 07A734, Mar. 2009.

[5] H. Nakamura, K. Hirota, T. MInowa, and M. Honshima, "Magnetic properties of extremely small Nd-Fe-B sintered magnets," *IEEE Trans. Magn*. vol. 41, no. 10, pp. 3844-3846, Oct. 2005.

[6] H. Sepehri-Amin, J. Liu, T. Ohkubo, K. Hioki, A. Hattori, and K. Hono,"Enhancement of coercivity of hot-deformed Nd-Fe-B anisotropic magnets by low-temperature grain boundary diffusion of $Nd_{60}Dy_{20}Cu_{20}$ eutectic alloy," *Scripta Mater*., vol. 69, no. 9, pp. 647-650, Nov. 2013.

[7] D. I. Paul, "General theory of the coercive force due to domain wall pinning, "J. Appl. Phys., vol. 53, no. 3, pp. 1649-1654, Mar. 1982.

[8] L. Liu, H. Sepehri-Amin, T. Ohkubo, M. Yano, A. Kato, T. Shoji, and K. Hono, "Enhancement of hot-deformed Nd-Fe-B magnets by the eutectic grain boundary diffusion process," J. Alloy. Compd., vol. 666, pp. 432-439, May. 2016.

[9] E. B. Boltich, E. Oswald, M. Q. Huang, S. Hirosawa, W. E. Wallacw, E. Bruzo, J. Appl. Phys. **57**, (1985) 4106.

[10]N. Watanabe, M. Itakura, M. Nishida, "Microstructure of high coercivity Nd-Fe-Co-Ga-B hot-deformed magnet improved by the Dy diffusion treatment," J. Alloys Compd., vol. 557, pp. 1-4, Apr. 2013.

[11] H. Haiduka, The Special Steel, 63,(2014) 45, in Japanese.

[12] K. Hioki, A. Hattori, T. Iriyama, IEEJ Transactions on Fundamentals and Materials, 136, (2016) 484.

[13] U.M.R. Seelam, T. Ohkubo, T. Abe, S. Hirosawa, K. Hono, "Faceted shell structure in grain boundary diffusion-processed sintered Nd-Fe-B magnets," J. Alloys Compd., vol. 617, pp. 884-892, Dec. 2014.

[14] T. G. Woodcock, Q. M. Ramasse, G. Hrkac, T. Shoji, M. Yano, A. Kato, O. Gutfleisch, "Atomic-scale features of phase boundaries in hot deformed Nd-Fe-Co-B-Ga magnets infiltrated with a Nd-Cu eutectic liquid,"Acta Mater., vol. 7, pp. 111-124, Sep. 2014.

[15] W. Rodewald, W. Fernengel, "Properties of sintered Nd-Fe-TM-B magnets," IEEE Trans. Magn. MAG-**24**, vol. 2, pp. 1638-1640, Mar. 1988.

6 Practical aspects of applications of the eutectic grain boundary diffusion process on bulky hot-deformed magnets

6.1 Introduction

So far in previous chapters, the study of the eutectic grain boundary diffusion process has been carried out the relatively small size hot-deformed magnets, which are in 4×4×2 mm^3 with easy axis along the 2 mm direction. The non-uniform distribution of Nd-rich intergranular phase from surface to the center regions has been observed as a common phenomenon in the diffusion processed magnets. For $Nd_{62}Fe_{14}Ga_{20}Cu_4$ which was investigated as diffusion sources in Chapter 4, despite the more uniform existence of intergranular phases, the coercivity was limited to 2.21 T due to the limited amount of applied diffusion sources. For HRE-containing ternary alloys, it is also necessary to explore how they would work when the diffusion process is carried out on bulky magnets. K. Löewe et al [1] investigated the temperature-dependent Dy diffusion in Nd-Fe-B sintered magnets and found higher temperature did not certainly lead to larger penetration depth since the bulk diffusion coefficient would be increased and they postulated the Dy-shell formation was due to the melting/solidification of a heavy-rare-earth-rich intermediate phase during high-temperature annealing. The diffusion depth of the eutectic diffusion sources, especially HRE-alloyed eutectics is a big concern and in this chapter Nd-Dy-Cu diffusion process is applied to the bulky hot-deformed magnets with the size of 7×7×5.6 mm^3, the easy axis is along 5.6 mm direction. The coercivity distribution and the microstructure of surface and center regions of the diffusion-processed magnet are discussed.

On the other hand, minimization of the degradation in remanent magnetization or looking for the possible way to rebuild the texture of $Nd_2Fe_{14}B$ grains are also very attracting from technological aspects.

The aim of the work in this chapter first is to investigate the Nd-Dy-Cu diffusion process on the bulky hot-deformed magnets with the size of 7×7×5.6 mm^3. The second part will focus on the study of the effect of the diffusion process under the expansion constraint [2] and will show the attempt to reconstruct the microstructure by a post-diffusion hot-pressing.

6.2 Coercivity enhancement of bulk hot-deformed Nd-Fe-B magnets by the eutectic grain boundary diffusion process using $Nd_{60}Dy_{10}Cu_{30}$ alloy

6.2.1 Experimental

Hot-deformed magnets with composition of $Nd_{12.9}(Fe,Co)_{81.1}B_{5.5}Ga_{0.5}$ (at.%) in 7×7×5.6 mm^3 size were used as the starting materials. The direction along 5.6 mm was the easy axis direction. $Nd_{60}Dy_{10}Cu_{30}$ alloy, which has the melting temperature of 560 ^oC (measured by DSC) was used as the diffusion material. As hot-deformed Nd-Fe-B magnet was dipped into a "solution" of $Nd_{60}Dy_{10}Cu_{30}$ powder suspension followed by heat-treatment at low temperature 650 ^oC for 3 hours.

Magnetic measurement of the as hot-deformed magnet and the bulk diffusion processed sample was carried out in a closed-magnetic circuit B-H tracer after fully saturation using a pulse high field of ~ 7 T. Partial coercivity measurement (surface and center part) was performed with a super conducting quantum interface device vibrating sample magnetometer (SQUID-VSM). Transmission electron microscopy was performed using Titan G2 80-200 transmission electron microscope with a probe corrector. Scanning transmission electron microscopy energy-dispersive spectroscopy (STEM-EDS) maps were constructed using Nd-Lα, Dy-Mα, Fe-Kα, Co-Kα and Cu-Kα spectrum. Atom probe experiment was carried out using a locally built laser assisted 3 dimensional atom probe. Atom probe specimens were prepared by lifting out and pasting a block of 2×2×5 μm^3 onto a sharpened W needle using a focused ion beam machine, FEI Helios Nanolab 650. The final sharpening of the needle-like specimen was made using a Carl Zeiss Cross-Beam 1540 EsB.

Finite element micromagnetic simulations were performed to study the effect of the magnetization of the intergranular layer and the higher anisotropy shell on the magnetization reversal of modeled samples comprising platelet-shaped grains with a mean grain size of ~200 nm in width and ~120 nm in height. The saturation magnetization ($\mu_0 M_s$), the magnetocrystalline anisotropy (K_1) and the exchange stiffness (A) of the $Nd_2Fe_{14}B$ phase were chosen to be 1.61 T, 4.5 MJ m^{-3} and 12 pJ m^{-1}, respectively [3]. The $\mu_0 M_s$ and A of the ferromagnetic and nonmagnetic thin intergranular phase were varied from 0.5 T and 12 pJ m^{-1} to 0 T and 0 pJ m^{-1}. The K_1 of the thin intergranular phase was set to be 0 MJ m^{-3}. The shell phase contains 0.1 at.% Dy with the thickness of 2 nm. Tetrahedron meshes with a maximum size of 2.5 nm were applied for the GBs, which grow to a maximum value of 15 nm in the $Nd_2Fe_{14}B$ grains, and the Landau-Lifshitz-Gilbert equation at each node was solved using FEMME software [4].

6.2.2 Result

a) Magnetic Properties

Fig. 6-1(a) shows the demagnetization curves of the as hot-deformed and the diffusion processed magnets. The coercivity ($\mu_0 H_c$) of the as hot-deformed sample was increased from 1.40 T to 2.52 T after the diffusion process, while remanence ($\mu_0 M_r$) decreased from 1.40 T to 1.25 T. The maximum energy product, $(BH)_{max}$, of the as hot-deformed and diffusion processed sample was calculated to be 380 and 305 kJ m^{-3}, respectively. Note that a slanted demagnetization curve is observed in the diffusion processed sample. This can be an indication of non-uniform distribution of coercivity in the diffusion processed magnet. Fig. 6-1(b) compares demagnetization curves obtained from two sliced samples from surface and center of the diffusion processed magnet showing a high coercivity of 2.7 T at the surface region and reduced coercivity of 2.3 T at the center of the sample. In addition, remanent magnetization also varies from surface to center region from 1.19 T to 1.32 T.

b) The overall microstructure of surface and center region of the diffusion processed magnet

Fig. 6-2(a) and (b) show the backscattered electron (BSE) SEM images of surface and center regions of the diffusion processed sample, in which, c-axis direction is indicated by the arrow. The dark contrast refers to the $Nd_2Fe_{14}B$ phase and the bright contrast corresponds to the Nd-rich intergranular phase. The

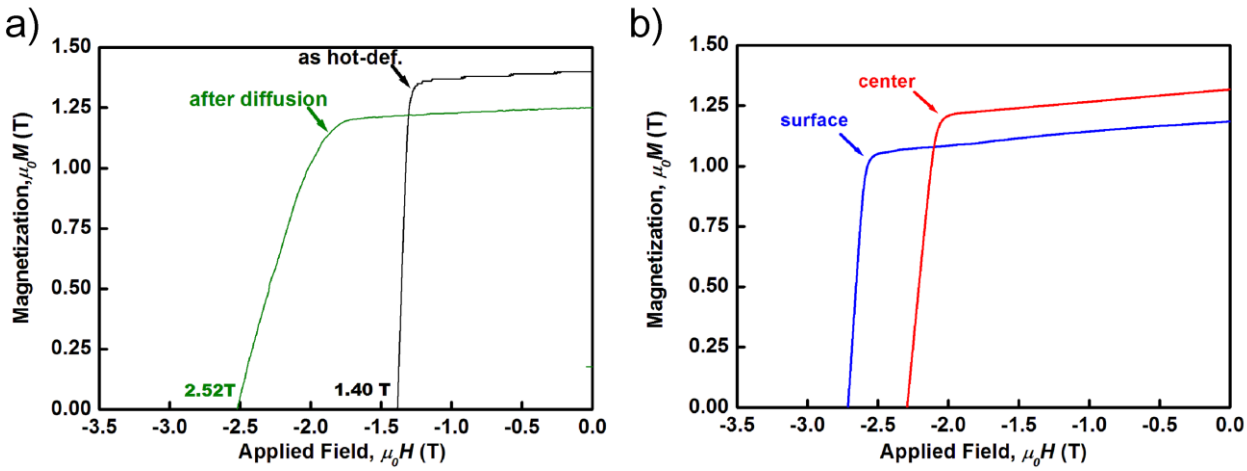

Fig. 6-1 Demagnetization curves of (a) the hot-deformed and Nd-Dy-Cu diffusion-processed magnets, (b) surface and center regions of the diffusion-processed magnets.

Nd-rich intergranular layer is preferentially formed along the platelet surface rather than platelet side. The areal fraction of the Nd-rich phase differs from 27 % at surface region to 15 % of center region. It is also of interest to note that two types of contrasts exist in the intergranular phase, as shown in Fig. 6-1(a): one is brightly imaged while the other in bright-grey contrast.

Fig. 6-2(c) and (d) display the low-magnification bright field (BF) transmission electron microscopy (TEM) images obtained from the surface and center regions of the diffusion processed sample. Figure 6-2(c) shows a strong strain contrast in the $Nd_2Fe_{14}B$ grains of the surface region; while this strain contrast cannot be observed in BF-TEM image obtained from the center region of the diffusion processed sample as indicated by Fig. 6-2(d). This might be due to the formation of much thicker Nd-rich crystalline intergranular phase at the surface compared to that of the center part. However, there is no conclusive experimental evidence so far showing a clear relationship between the coercivity value and the existence of strain field effect.

Fig. 6-3(a) and (b) show low magnification STEM-EDS maps obtained from the surface and center region of the diffusion processed sample, respectively. Depletion of Fe and enrichment of Nd, Co and Cu is both observed in the intergranular phase in both surface and center region. $Nd_2Fe_{14}B$ grains are well separated from each other by Nd-rich phase lying parallel to the flat surface of the platelets for either surface or center region after the diffusion process. In these low magnification STEM-EDS maps, segregation of Dy was found at the intergranular phase of the surface region. Comparison of element maps of Nd, Co and Cu shows that mainly two types of the intergranular phases exist in this magnet; (Nd,Co,Cu)-rich intergranular phase and Nd-rich intergranular phase with some small segregation of Cu.

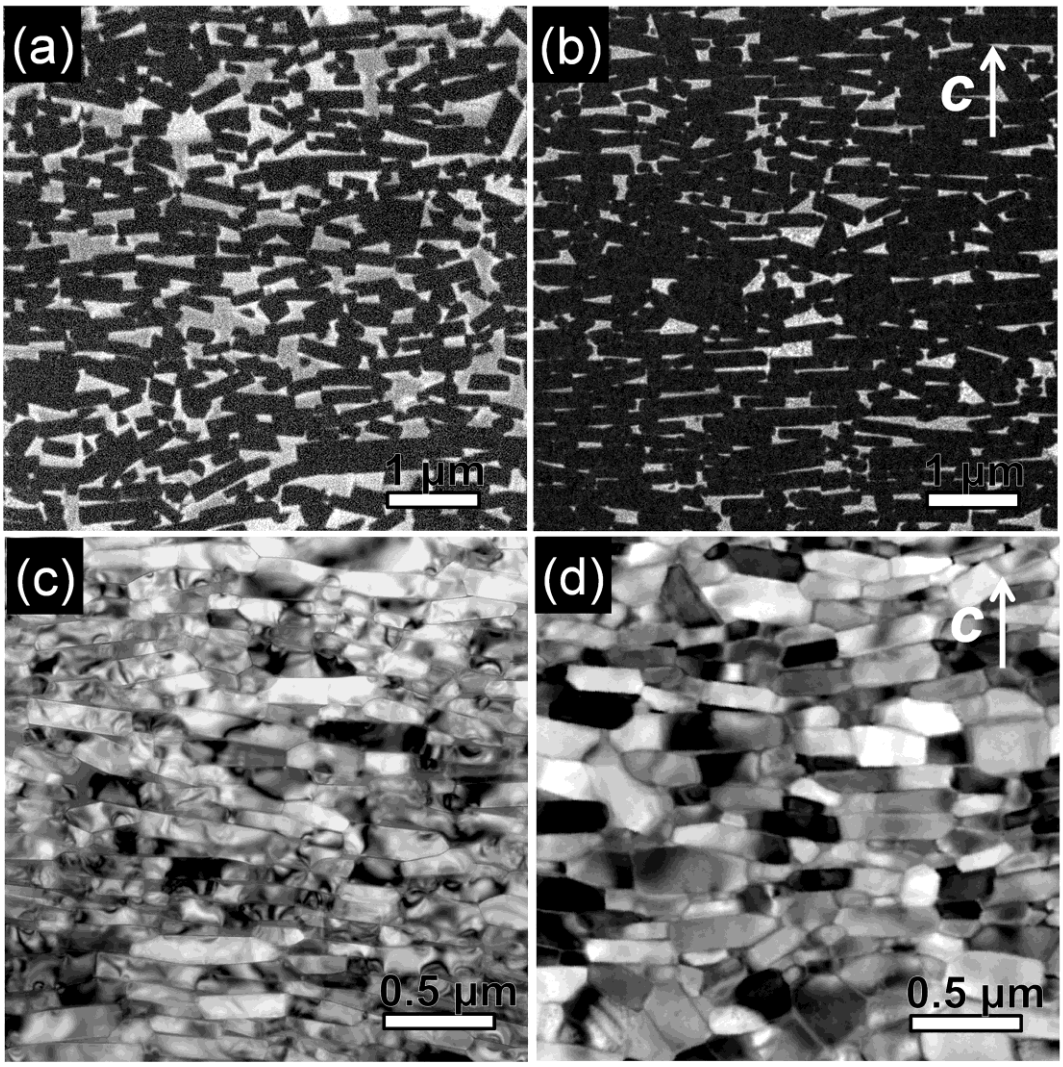

Fig. 6-2 SEM BSE images and Low-magnification BF images of surface regions (a, c) and center regions (b, d) of the diffusion-processed magnets. The c-axis is in-plane as indicated by the arrows.

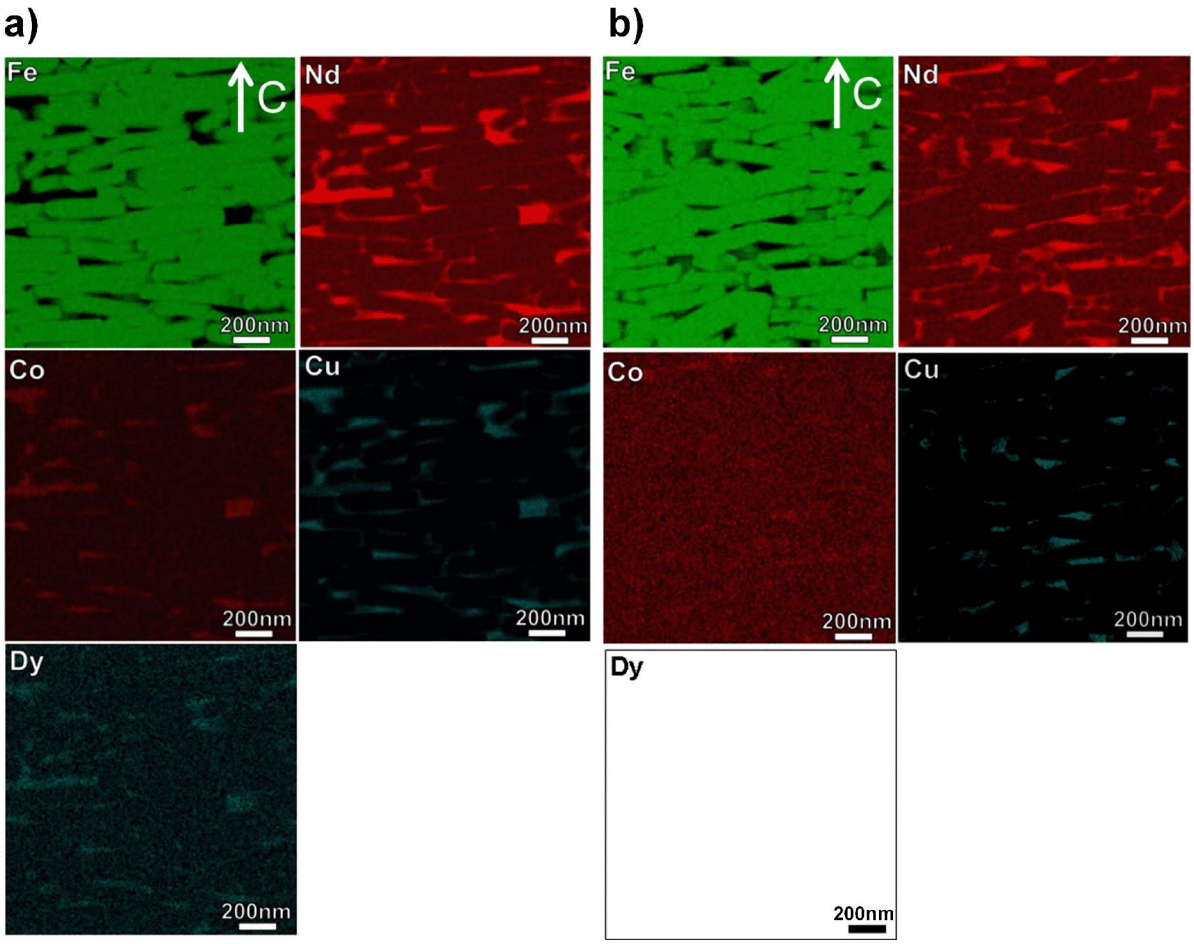

Fig. 6-3 STEM-EDS elemental mapping images of the diffusion-processed sample: (a) surface region and (b) center region with c-axis in-plane. The selected peaks in the EDS spectrum for these maps are Fe K_α, Nd K_α, Co K_α, Cu K_α and Dy M_α.

the intergranular phase can be resolved to contain 45±1 at.% Nd and 47±2 at.% Fe, with a Co enrichment of about 10±3 at.%. Dy content in the intergranular phase is confirmed to be zero for the center region of the diffusion processed sample. It is likely that Dy completely vanished ongoing to the center region of the sample during the Nd-Dy-Cu diffusion process.

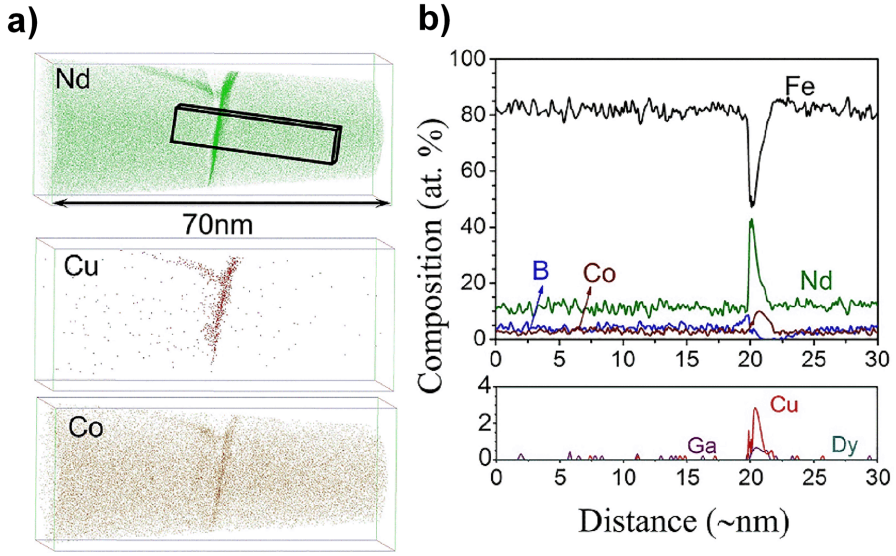

Fig. 6-4 (a) 3DAP maps of Nd, Cu, and Co of Nd-rich intergranular phase in the center regions of the diffusion-processed sample. (b) concentration depth profiles for Fe, Nd, Co, B, Cu, Ga and Dy, determined from the selected box shown in the Nd map in (a).

c) Characterization of intergranular phase of the surface region

Detailed characterizations are carried out to study the intergranular phase to figure out the mechanism of coercivity enhancement of the surface region of the diffusion processed sample. One important observation is that there are at least two types of intergranular phase lying parallel to the c-plane of the $Nd_2Fe_{14}B$ grains. One is amorphous intergranular phase that has the thickness around 15 nm, as shown in Fig. 6-5(a); in addition, another crystalline thin grain boundary with thickness of about 3 nm, displayed in Fig. 6-6(a), is also found in the surface region of the diffusion processed sample. This phenomenon is different with that found in the sintered magnets, where the thin metallic grain boundary layers tend to be amorphous when its thickness is below 1 nm and become crystalline at greater thickness [5]. However, the thick amorphous intergranular phase is not the majority phase observed in the surface region of the diffusion processed sample. Most of the case, intergranular phase(s) are found to be crystalline phase and lattice misfit between these phases and $Nd_2Fe_{14}B$ phase gives rise to the strain field contrast, as mentioned in the previous part.

The HAADF image in Fig. 6-5(a) shows the microstructure of the thick amorphous intergranular phase and the neighboring $Nd_2Fe_{14}B$ grain. The configuration of this type of grain boundary phase indicates it to be non-ferromagnetic. Lattice fringes can be resolved by the high resolution of HAADF-STEM imaging which are originated from Nd atoms in $Nd_2Fe_{14}B$ phase, out of which, the layers that have more outstanding

contrast correspond to the Basal plane of $Nd_2Fe_{14}B$ crystal. Circular blurred contrast surrounding the Nd-atoms stems from the projection of Fe atoms within [-110] direction. A tri-layer atomic interface can be seen between $Nd_2Fe_{14}B$ phase and this amorphous intergranular phase; at the termination layer of $Nd_2Fe_{14}B$ phase, Nd atoms have a slightly raised contrast compared to the equivalent Nd atoms inside the $Nd_2Fe_{14}B$ phase.

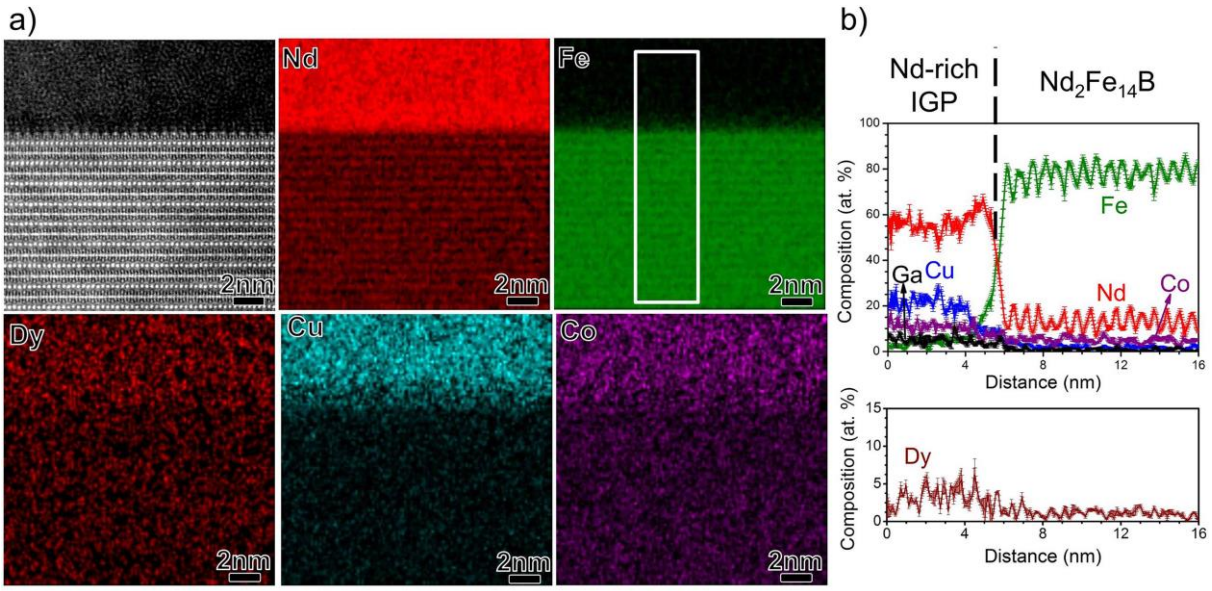

Fig. 6-5 (a) HAADF-STEM image of the thick amorphous intergranular phase and EDS maps for Nd-L, Fe-K, Dy-M, Cu-K and Ga-K from the same region in the surface of the diffusion-processed magnet, (b) line-scan profile for the region marked in Fe map (a).

STEM-EDS maps indicate enrichment of Nd, Ga as well as Cu in the intergranular phase, where Fe is depleted. Indeed, by combining the line-scan result (Fig. 6-5(b)), Fe concentration of this grain boundary phase is lower than 5 at.%, suggesting a much diluted ferromagnetism [6]. Ga and Cu segregation starts from the first atomic layer of the tri-layer interface, while Dy enrichment occurs from the second atomic layer till to the intergranular phase. Around 5 at.% Dy is enriched at the intergranular phase which contains more than 20 at.% Cu. Dy also shows around 2 at.% enrichment in the $Nd_2Fe_{14}B$ phase, which is within the noise level of the EDS spectra, where the 3σ (σ is the standard derivative of the content quantified from the collected EDS spectra). Co distribution in the intergranular phase is more or less similar to that in the $Nd_2Fe_{14}B$ phase.

Fig. 6-6 shows a second type of intergranular phase in the diffusion processed sample which is crystalline phase with the thickness around 2 nm. Similar segregation of Ga and Cu can be observed at the interface between $Nd_2Fe_{14}B$ phase and the thin grain boundary phase. According to the concentration profile taken from the region indicated by the rectangle in Fig. 6-6(a), Cu in this intergranular phase is much lean (<8 at.%) compared with that of the thick amorphous intergranular phase. Dy shows about 4 at.% enrichment in the intergranular phase. Co still shows relatively uniform distribution; slightly depleted in the thin intergranular phase. The interfacial plane of the upper neighbouring 2:14:1 grain, here, does not correspond to a low-index lattice plane; it seems that the segregation is not dependent on the lattice relationship between the $Nd_2Fe_{14}B$ phase and the grain boundary phase.

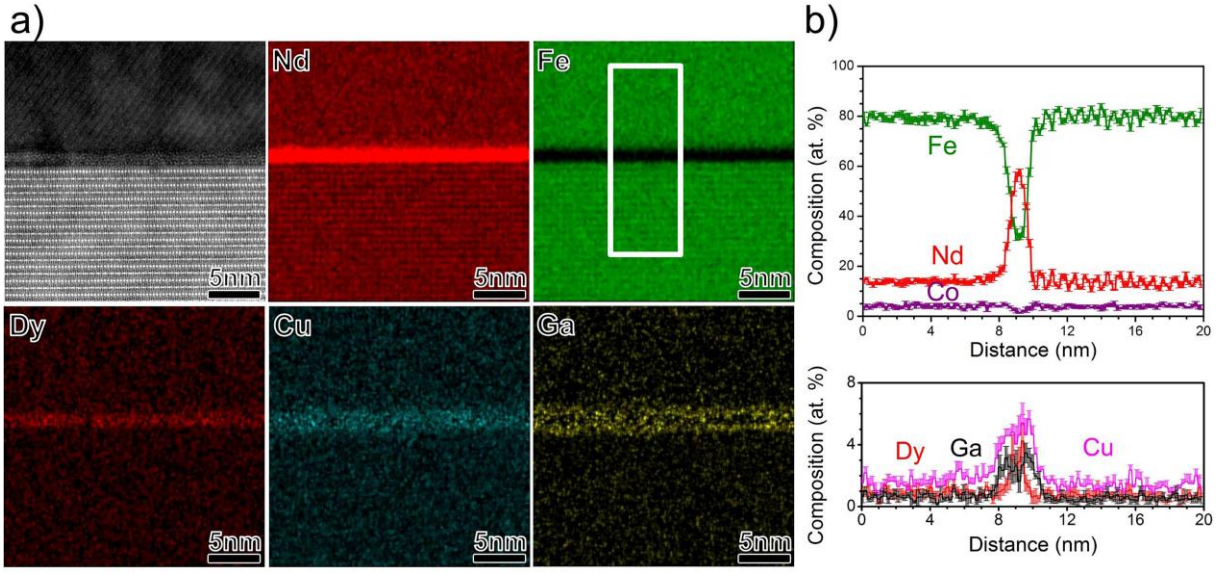

Fig. 6-6 (a) HAADF-STEM image of the thin grain boundary phase and EDS maps for Nd-L, Fe-K, Dy-M, Cu-K and Ga-K from the same region in the surface of the diffusion-processed magnet, (b) line-scan profile for the region marked in Fe map (a).

Fig. 6-7 demonstrates a third type of intergranular phase in the surface region of the diffusion-processed sample. As this kind of intergranular phase does not neighbor with the c-plane of any $Nd_2Fe_{14}B$ phase, it is called here side grain boundary phase. A unique ledge shape is found on the surface of the $Nd_2Fe_{14}B$ grains. This kind of step defect is believed to form during the solidification of the intergranular phase, has very uniform pattern, which maintains a periodic height of the whole unit cell of $Nd_2Fe_{14}B$ phase along c-axis. It is obvious that the termination layer of $Nd_2Fe_{14}B$ phase to the intergranular phase at this side grain boundary is composed by both Nd and Fe atoms. The first-principle and LDA (local density approximation) simulation has shown the strong in-plane anisotropy feature of "bad" Nd atoms located at terminated (001) plane next to the grain boundary phase and those exposed to oxides at side surfaces [7] However, further investigations are necessary to figure out the factors that lead to the formation of these step defects and how these step defects would work on the magnetization process. Combining the quantitative analysis afterwards, shown in Fig. 6-7(b), segregation of Cu and Ga is also observed at the interface between the side grain boundary phase and the $Nd_2Fe_{14}B$ phase. Nd concentration in the grain boundary phase is close to 60 at.%, while content of Fe+Co is only around 20 at.%, indicating a much diluted ferromagnetism by the diffusion process. It is of interest to notice that segregation of Dy at both interfaces between the side grain boundary phase and $Nd_2Fe_{14}B$ phase can be found, approaching the concentration of 5 at.%.

The segregation behavior is caused by the complex eutectic reactions among multi-elements. During the solidification of the liquid of the intergranular phase and even the very surface of the $Nd_2Fe_{14}B$ phase, excessive Cu and Ga would tend to be ejected to the interface between two phases. With high-resolution HAADF-STEM imaging and EDS mapping images, information of microstructure and concentration of the

three types of intergranular phase have been elucidated. However, the question remains as to what exactly these phases are and how they will function during the magnetization and demagnetization process.

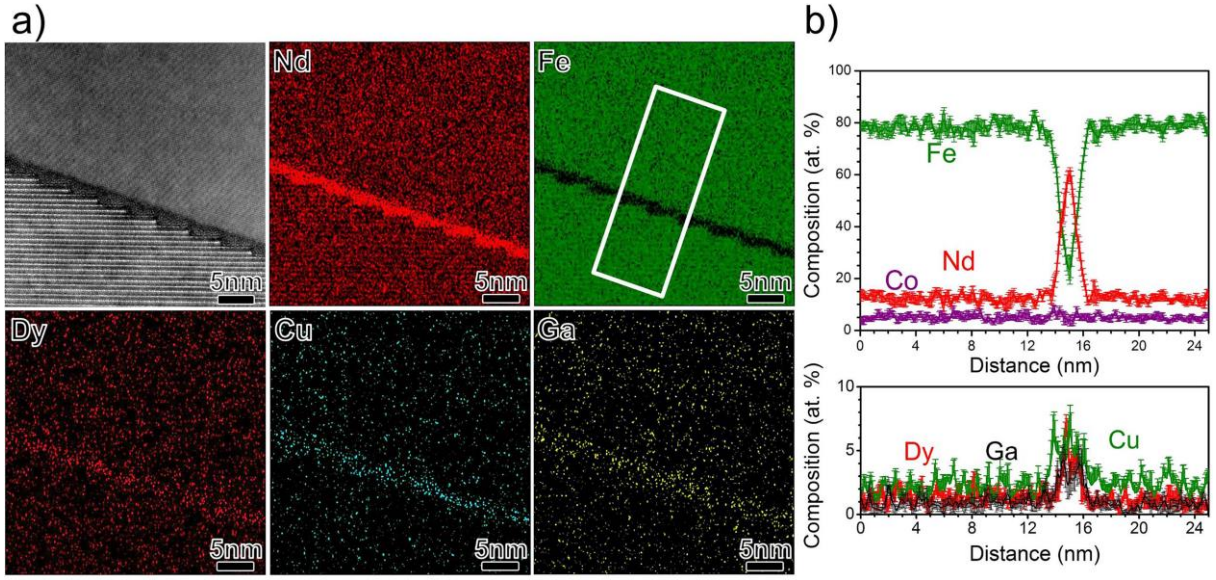

Fig. 6-7 (a) HAADF-STEM image of the side grain boundary phase and EDS maps for Nd-*L*, Fe-*K*, Dy-*M*, Cu-*K* and Ga-*K* from the same region in the surface of the diffusion-processed magnet, (b) line-scan profile for the region marked in Fe map (a).

6.2.3 Discussion

The grain boundary diffusion process using eutectic composition $Nd_{60}Dy_{10}Cu_{30}$ consists of two important diffusion processes [8]: one is diffusion through Nd-rich grain boundary phase; another is the volume diffusion to the $Nd_2Fe_{14}B$ grains with the formation of Dy-rich shells. The diffusion coefficient of the former process is much larger than the latter one. Diffusion through the grain boundary phase would progress rapidly because of the liquid phase diffusion. It is expected to be complete once heat up the magnet to the melting-point of $Nd_{60}Dy_{10}Cu_{30}$.

We have seen that the increase in coercivity is accompanied by the increment of the areal fraction and the thickness of the Nd-rich intergranular phases, also the dilution of ferromagnetism of the intergranular phase due to the depletion of Fe content after the diffusion process. At least two types of intergranular phase that lies parallel to the c-plane of $Nd_2Fe_{14}B$ grains can be observed after the diffusion process: one has thick amorphous structure, comprising with the phase in which Nd to Cu ratio is about 7:3; another forms a lamellar structure which is more depleted in Cu compared the former intergranular phase and has a thin amorphous structure.

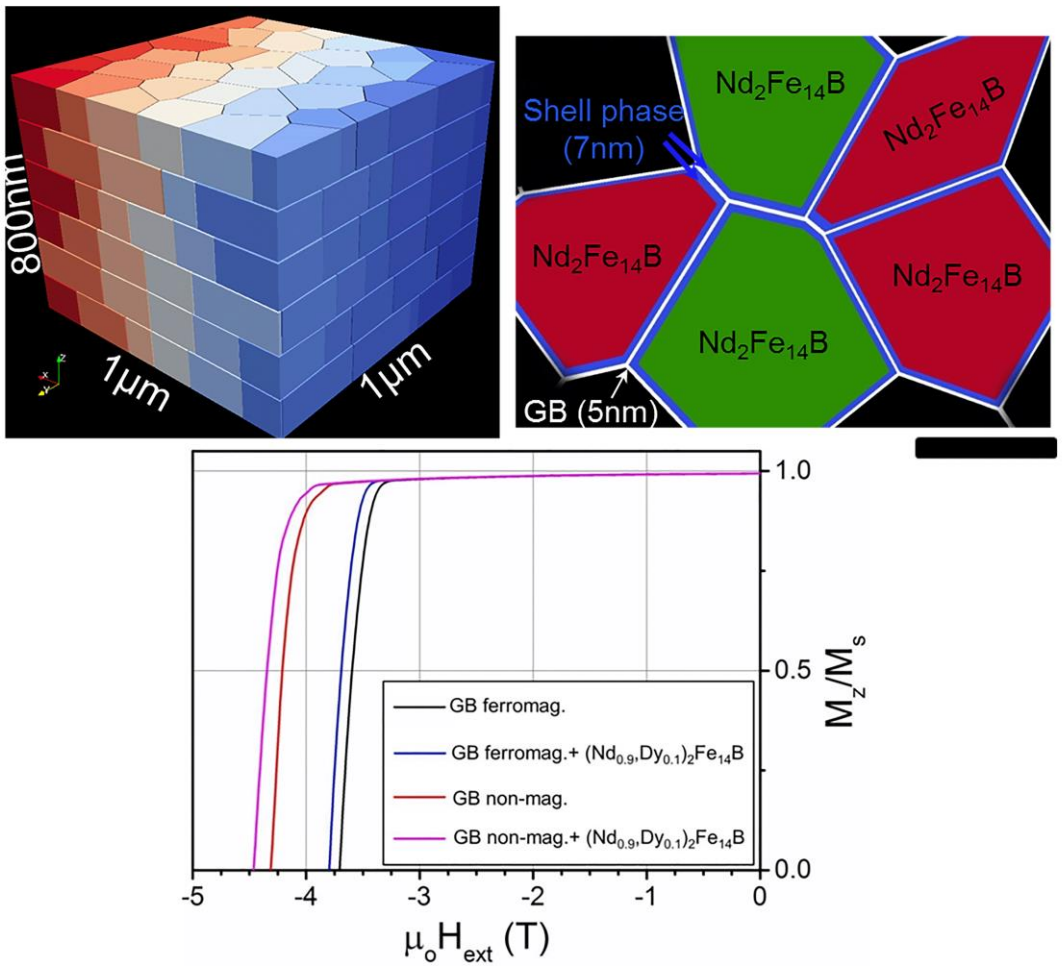

Fig. 6-8 (a) The microstructure of a finite element model with a size of 1×1×0.8 μm^3, showing the grain size. (b) The schematic image of the microstructure of the modeled hot-deformed magnet. (c) The demagnetization curves of the simulated samples with different magnetization (0 and 0.5 T) and w/o Dy-rich shell phase.

Segregation layer enriched with Cu and Ga can be found at the interface between $Nd_2Fe_{14}B$ grains and the intergranular phase, which is considered to be able to accommodate the defects located at the surface of $Nd_2Fe_{14}B$ grains, thus increasing the nucleation field of the reversal magnetic domains. However, there are also some reports [9] suggesting that the Cu segregation plays a very important role in the formation of the distorted lattice at the interfacial plane between the $Nd_2Fe_{14}B$ phase and the intergranular phase, and claiming this would lead to the reduction of localized anisotropy field at the 2:14:1 grains, thus decrease the coercive force. But the recent report by Murakami et al [10] conducted a direct measurement of the interfacial strain from the artificial moiré fringes in STEM images shows only 1% of strain exist at Nd-rich phase(s)/$Nd_2Fe_{14}B$ interface. The effect caused by this magnitude of strain is so small to have crucial influence on the anisotropy field of interfacial layers. Indeed, the interfacial features in this work is more

complicated, further investigations are very essential to find out how these characteristics will affect the magnetization reversal process.

If we seek for explanation of coercivity enhancement by domain wall pinning theory of coercivity, we can refer to the function derived by Paul [11, 12], i.e.$H_c \propto \frac{K_1 W}{\delta_0}(\frac{A_1}{A_2} - \frac{K_2}{K_1})$ which is feasible when the defect width is under or comparable to the domain wall width. In the equation, K_1 and K_2 denote the magnetocrystalline anisotropies of $Nd_2Fe_{14}B$ and GB phases, respectively; A_1, A_2 represent exchange energy of $Nd_2Fe_{14}B$ and GB phases, respectively; W and δ_0 stand for width of defect and domain wall, respectively. Formation of the thick intergranular phase after the diffusion process results in the increment of pinning site width. A diluted ferromagnetism of the intergranular phase caused by Fe depletion and Nd, Cu enrichment leads to a reduction of magnetocrystalline anisotropy K_2 and exchange energy, A_2 of GB phases. In particular, if the intergranular phase forms amorphous microstructure, it will have the magnetocrystalline anisotropy close to zero. All these factors will contribute to the increment of pinning force provided by the grain boundary phases, thus gives rise to the coercivity enhancement.

The areal fraction and thickness of the Nd-rich intergranular phase both decreased from the surface region to the center region. Indeed, we have better magnetic isolation between $Nd_2Fe_{14}B$ grains by the intergranular phase for surface region than that of center region. In addition, since Dy has higher affinity to oxygen, which probably causes Dy easier to be trapped by the oxygen from the surface region of the bulk magnet. Dy content is confirmed to be zero when goes to the center of the diffusion-processed sample. This explains the large coercivity distribution of grain boundary diffusion for the bulk magnets. The partial coercivity is high at the surface but it decreases on going towards the center of the magnet. This kind of laminated structure of Nd-Fe-B magnets, reported by Nakamura et al. [13], can be used as heat resistive magnets.

In order to figure out the role of the thin nonmagnetic intergranular phase and the Dy-rich shell layer on the magnetization reversal process and coercivity, micromagnetic simulation was performed using the model that has the geometry similar to the experimental observation, as shown in Figure 6-8. The intergranular phase layers lying parallel to the flat surface of the platelets were assumed to be nonmagnetic with a thickness of 10 nm. The thickness of the intergranular phase layer located at the sides of the $Nd_2Fe_{14}B$ platelets (parallel to the c-axis) was set to be 3 nm. The magnetization of the intergranular phase was varied from 0.0 T to 0.5 T. The exchange stiffness of the ferromagnetic intergranular phase was selected the same as that of the $Nd_2Fe_{14}B$ phase, given that no reports on the exchange stiffness value of the thin intergranular phase of the hot-deformed magnets. The shell phase, with the thickness of around 2 nm, contains 10 at% Dy. The demagnetization curves demonstrate that the coercivity of the modeled hot-deformed sample increases from 3.75 T to 4.25 T by the reduction of the magnetization of the thin intergranular phase. In both cases, if the Dy-rich shell layer was introduced to the surface of the $Nd_2Fe_{14}B$ grains, coercivity value of the modeled hot-deformed magnets can be further enhanced to 3.85 T and 4.35 T, respectively.

6.2.4 Conclusion on Nd-Dy-Cu GBDP

In this work, $Nd_{60}Dy_{10}Cu_{30}$ grain boundary diffusion process was applied to the bulky hot-deformed Nd-Fe-B magnets in the size of 7×7×5.6 mm^3. The average coercivity was improved from 1.4 T to 2.52 T, with the remanence degradation from 1.40 T to 1.25 T. There exists a large coercivity distribution of the diffusion-processed magnet from surface to the center region. The coercivity measured for the surface part of the magnet shows the coercivity of 2.70 T while 2.30 T for the center. The remanence also varied from 1.19 T to 1.32 T, respectively.

From microstructural analysis, better isolation between $Nd_2Fe_{14}B$ grains by the Nd-rich intergranular phase was observed. No Dy-rich shell can be observed both for surface and center regions in the diffusion processed magnet. In the surface region, Dy is mainly partitioning in the Nd-rich intergranular phase and substitutes Nd on the very surface layer of the $Nd_2Fe_{14}B$ grains. However, in the center region of the magnet, Dy can no longer be detected, as analyzed with the atom probe.

By precise ICP-OES (Inductively Coupled Plasma-Optical Emission Spectrometer) analysis, the average Dy concentration of the diffusion-processed magnets is evaluated to be 0.78 wt.%. When we put the property of $Nd_{60}Dy_{10}Cu_{30}$ diffusion processed magnet in the Figure 6-9 [14, 15] that make plot between coercivity and Dy contents in sintered magnets processed by various methods including conventional binary alloy method, Dy-nitride, Dy-fluoride, Dy-oxide doping and the electropheric deposition of DyF_3, the enhancement of coercivity yielded by every weight percentage of Dy utilization shows 1.29 T which is superior to the conventional GBDP and also the EPD method. This also suggests us we might also apply this eutectic GBDP to the sintered magnets with HREEs-alloyed eutectics as the diffusion sources to retain the merit of minimizing HREEs doping amount.

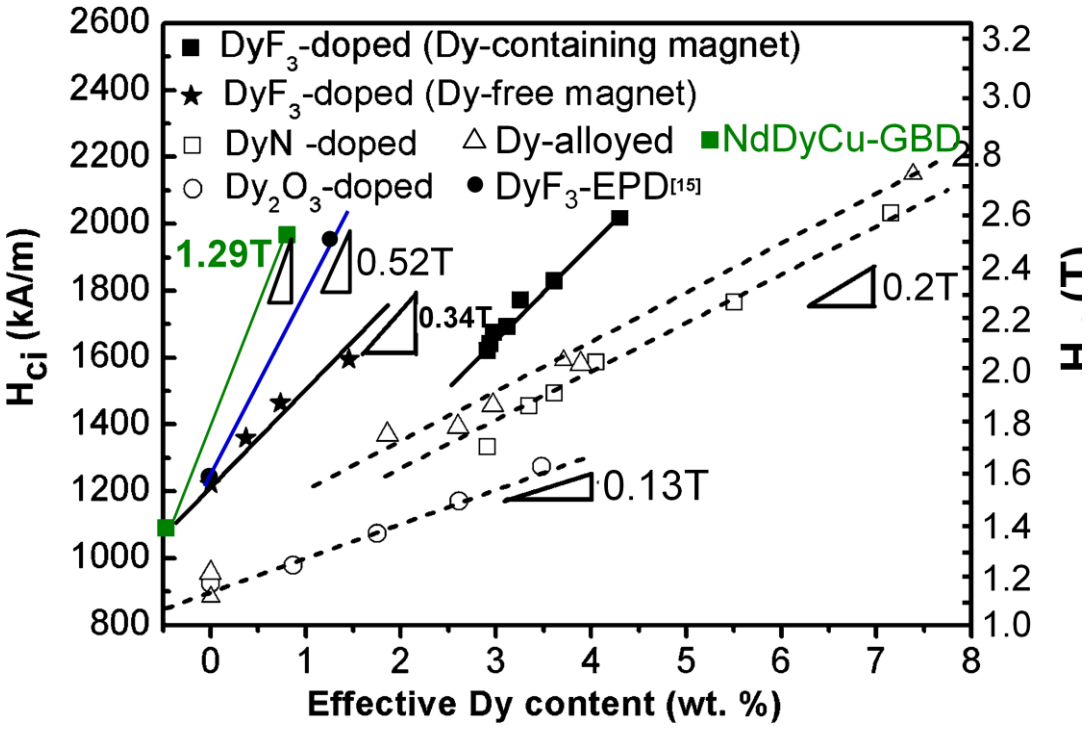

Fig. 6-9 Improvement of coercivity against effective Dy content of the processed magnet by various methods [14].

6.3 Effect of expansion constraint on the eutectic GBDP

As described in the previous section, the limited diffusion depth is one of the crucial factors limiting the application of the grain boundary diffusion process with surface diffusion poles to bulky magnets as so to the commercial production line. In the study of Dy powder diffusion in Nd-Fe-B sintered magnets [1], they observed the Dy content in the shell decreased from ~6 at.% of coating surface to ~1 at.% after a diffusion depth of 400 μm in the sample with the size of 10×10×3 mm^3 when the Dy powder was coated on both 10×10 surfaces. However, in the report by U. M. R. Seelam et al [16] on the Dy vapor diffusion process on the sintered magnets in the size of 5×5×3.5 mm^3, the Dy content of the shell only varied from 1.35 at.% to 0.79 at.% going from surface to the center of the bulk sample.

Despite the HREEs diffusion process is closely correlated with the mechanism of HRE-rich shell formation which have totally different behavior as the eutectic GBDP on hot-deformed magnets, we are actually facing the same problem in terms of the diffusion depth of Nd-rich intergranular phase. This is also believed a product of the equilibrium melting-solidification process between the intergranular phase and $Nd_2Fe_{14}B$ phase. In the report by Akiya et al [2], the application of the expansion constraint during Nd-Cu diffusion process realized the coercivity enhancement from 1.4 T to 1.92 T with a much smaller remanence drop to from 1.39 T to 1.36 T. In contrast, the Nd-Cu diffusion-processed magnet without constraint showed the deterioration in remanence to 1.27 T. They postulated the main reasons for this improvement were improvement of the $Nd_2Fe_{14}B$ phase (001) texture. However, the direct microstructural evidence of a quantitative analysis of alignment degree in the report was not provided. It's worthy to explore this method to other diffusion sources and to perform the in-depth analysis for the coercivity distribution and microstructure change for the bulk sample after the diffusion process.

6.3.1 Experimental

In this study, the hot-deformed magnets with the nominal composition of $Nd_{13.2}Fe_{76}Co_{5.6}B_{4.7}Ga_{0.5}$ at. % in the size of 5×5×4 mm^3 were used as the starting materials. $Nd_{80}Ga_{15}Cu_5$ alloy was selected as the diffusion sources. Melt-spun Nd-Ga-Cu ribbons were applied on the lateral surface parallel to easy-axis, which means the surface with the dimension of 5 mm×4 mm. The coated samples were heat treated at 600^oC for 3h under vacuum of 10^{-3} Pa. The expansion constraint was applied on both c-planes i.e. the 5 mm×5 mm surfaces. The freedom left for the magnet to expand along c-axis, i.e. the distance between the sample surfaces to the constraint plate, was designed as 0.1 mm and 0 mm, hereafter this distance will be referred as *t* for convenience. For demonstrating the effect of expansion constraint, the applied diffusion sources were kept the same as 20 wt.% of the initial hot-deformed sample.

The hysteresis curves were measured with a super conducting quantum interface device vibrating sample magnetometer (SQUID-VSM) for the specimen sliced along the easy-axis from different depths of the diffusion-processed samples. The specimen dimension was in ~1×1×0.1 mm^3. Demagnetization factor correction was determined based on the dimensions of the prism-shaped specimen. The microstructure

characterization by SEM observations was carried out to the region within the same depth as the SQUID-VSM specimen for a correlative analysis.

6.3.2 Results

Figure 1-10 shows the hysteresis curves of the initial hot-deformed magnets, Nd-Ga-Cu diffusion-processed magnets under different conditions. Under free expansion, the diffusion processed magnet shows the coercivity of H_{ci}= 2.32 T improved from 1.2 T of the initial hot-deformed magnets, with the remanent magnetization $\mu_0 M_r$ drop from 1.52 T to 0.98 T. However, the magnet under expansion with t= 0.1mm exhibited a pronounced higher remanent magnetization $\mu_0 M_r$ of 1.32 T with lower coercivity H_{ci} of 2.03 T. On the other hand, if the expansion freedom t was set as 0 mm, the diffusion processed magnet no longer shows the obviously large recovery in remanent magnetization. It has slightly higher remanence of 1.04 T and a reduced coercivity of 2.07 T with respect to the sample under free expansion. It can also be seen from the hysteresis loops that applying expansion constraint with t= 0.1mm leads to an improvement in the squareness when the comparison is taken with the magnet left for free expansion, while with t= 0 mm an obvious deterioration in squareness induced. M_r/M_s ratio of the three samples which were calculated to be 0.91(5), 0.93(1) and 0.89(4) for the free expansion, t= 0.1mm and t= 0 mm constrainted magnets, respectively. This comparison reveals that the expansion constraint with t= 0.1mm leads to an improvement of the easy-axis alignment of the diffusion processed magnets, whereas for t= 0 mm, the reduced the value indicates the complete constraint process fails in texture recovery.

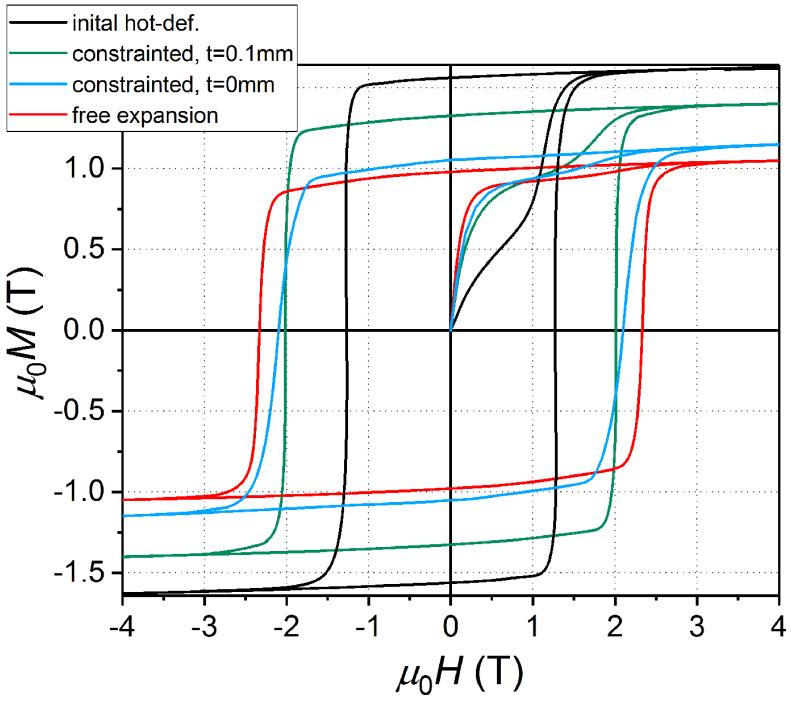

Fig. 6-10 Hysteresis loops of the initial hot-deformed and Nd-Ga-Cu diffusion-processed magnets.

Further investigation was done by carrying out the magnetic property measurement and microstructural characterization to the specimen sliced from several depths of the diffusion-processed magnets. The Fig. 6-11 indicates the comparison of demagnetizations curves measured for the specimens prepared from different depths for diffusion-processed magnets under the expansion constraint with t= 0.1mm(a) and the magnet left for free expansion (b). This comparison indicates for both samples, the variations in coercivity from surface to the center were very small whereas there is degradation of remanent magnetization $\mu_0 M_{r,}$ especially for the magnet diffusion-processed without applying expansion constraint.

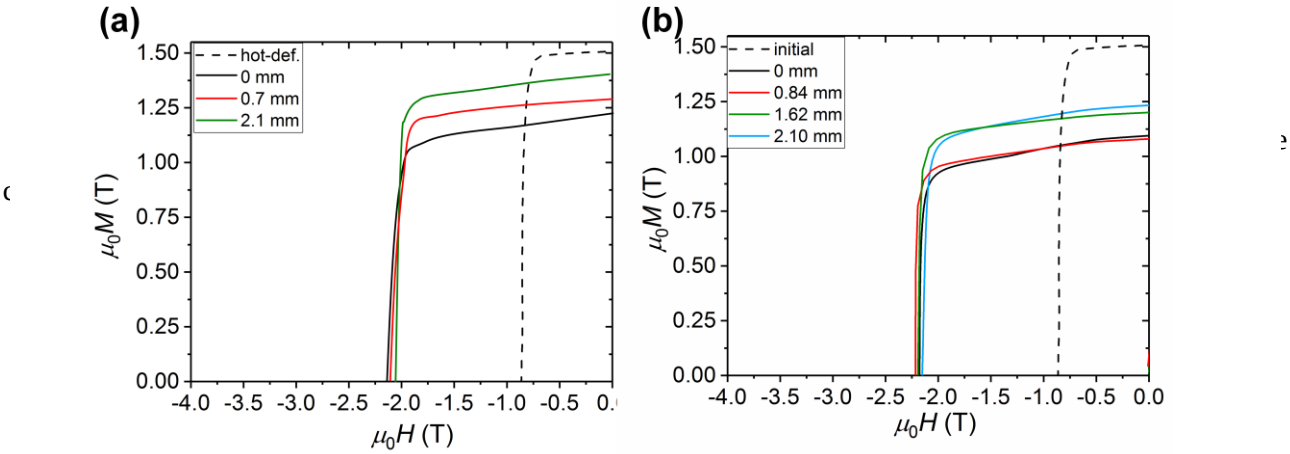

Fig. 6-11 Demagnetization curves of the Nd-Ga-Cu diffusion-processed magnets under expansion constraint with t= 0.1mm (a) and without expansion constraint applied (b) measured for the specimen taken from different distances from surfaces of the magnets.

Fig. 6-12 shows the BSE-SEM images for the region within the same depths as the vsm specimen were prepared of the expansion-constrainted (a) and freely expanded magnets (b). It can be clearly seen that in the diffusion-processed magnet without expansion constraint, Nd-rich intergranular phases decreased abruptly from surface to center regions while they keep almost constant distribution in the magnet under expansion constraint (with t= 0.1mm). Along with the agglomeration into triple junctions of Nd-rich intergranular phases, abnormal grain growth was also frequently observed. Besides, these regions will also display poor alignment of $Nd_2Fe_{14}B$ grains. For the region lying at the very surface of the diffusion processed magnet without constraint, this was the most pronounced. Moreover, we could find the texture was getting gradually improved for the magnets left for free expansion when the observed region was located deeper from the magnet surface. In contrast, $Nd_2Fe_{14}B$ phase of the diffusion processed magnet under expansion constraint with t= 0.1mm demonstrates the high texture from the surface region and it got even higher in the center region.

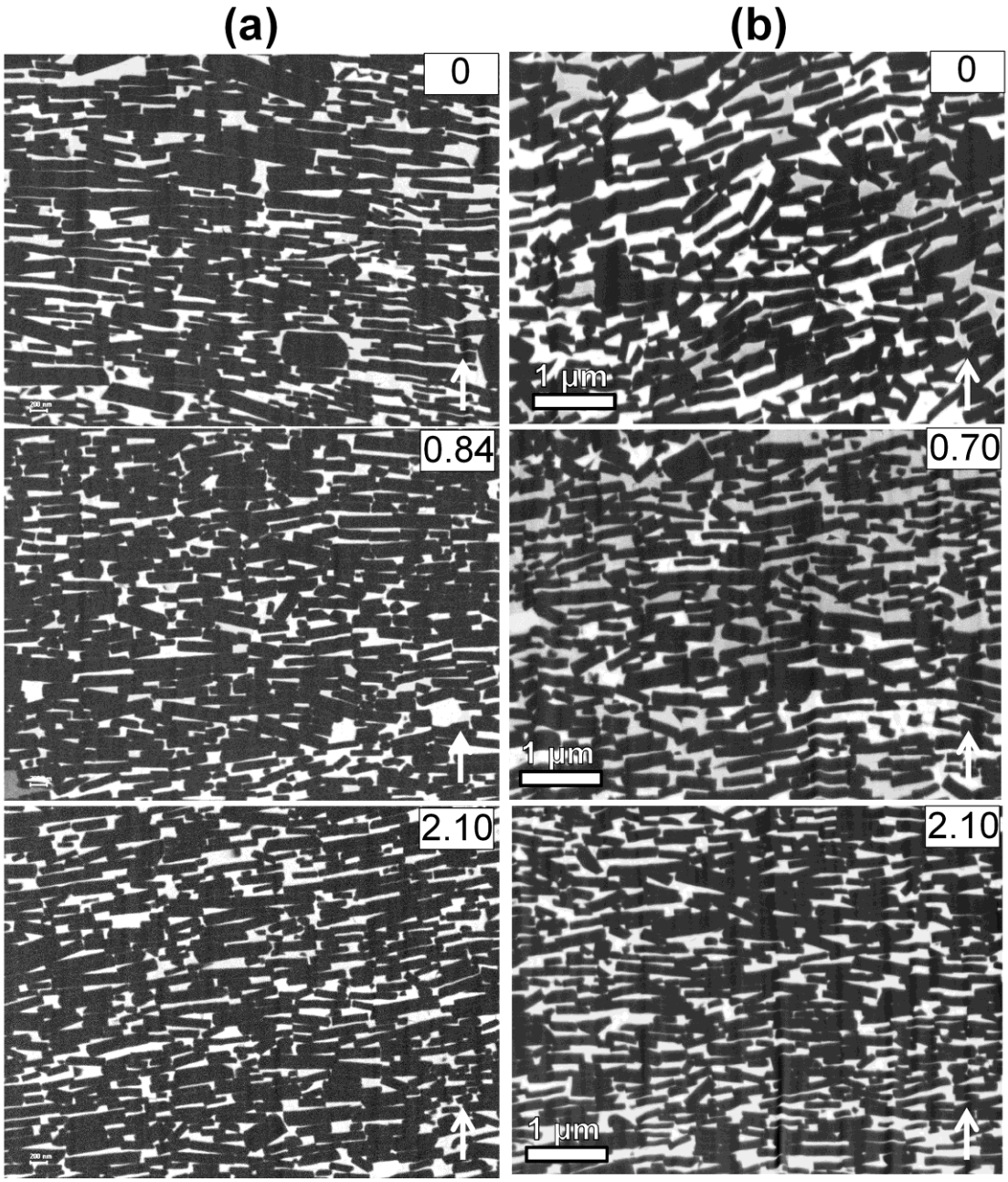

Fig. 6-12 BSE-SEM images of the Nd-Ga-Cu diffusion-processed magnets under expansion constraint with *t*= 0.1mm (a) and without expansion constraint applied (b) taken from regions within the same distances from surfaces of the magnets as the vsm specimens. The observation direction is along c-axis in-plane; as indicated by the arrows.

If the comparison is made by putting all these data in the plot as shown by Figure 6-13, in which the coercivity H_{ci}, remanent magnetization $\mu_0 M_r$, and the areal fraction of Nd-rich intergranular phase against different depths of the analyzed regions for the Nd-Ga-Cu diffusion processed magnets without were included. The areal fraction of the Nd-rich intergranular phase was calculated by the different contrasts in the BSE-SEM images. We can find applying the expansion constraint with leaving the expansion freedom *t* of 0.1mm leads to higher remanent magnetization compared with the magnet processed without constraint. When we compare the change in the distribution of Nd-rich intergranular phase which formed on solidification from the reaction between the infiltrated diffusion sources with the initial grain boundary phase and most likely also with the $Nd_2Fe_{14}B$

phase, it reveals the mechanism of the enhanced remanent magnetization with the proper expansion constraint in most part lies in the effect of providing more uniform distribution of the Nd-rich intergranular phase. Which means a larger diffusion depth of the eutectic grain boundary diffusion was realized by applying the expansion constraint. Moreover, the enhancement in (001) texture of $Nd_2Fe_{14}B$ phase in the magnet processed with expansion constraint (t =0.1 mm) was also confirmed from the BSE-SEM observation despite the limited sampling size of the electron microscopy.

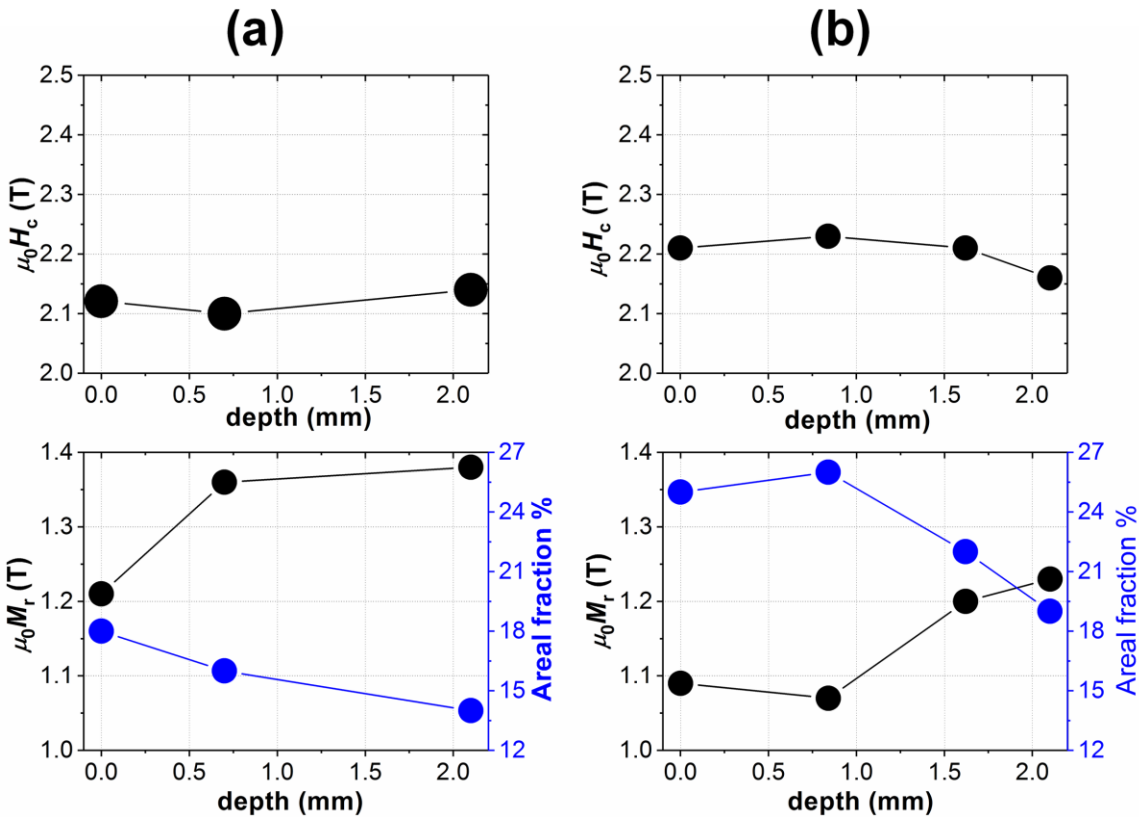

Fig. 6-13 Plot of the coercivity, remanent magnetization and areal fraction of Nd-rich intergranular phase against the depths of the analyzed regions of the Nd-Ga-Cu diffusion-processed magnets under expansion constraint with t= 0.1mm (a) and without expansion constraint applied (b).

However, when we attempted to further take advantage of the expansion constraint during the diffusion process to bring up the remanent magnetization further by leaving zero freedom (t = 0 mm), we found the disappointing result in this case as described before. Apart from no more gaining remanent magnetization, the coercivity also decreased for the magnet processed with a full constraint. The SEM observation of this full-constrainted Nd-Ga-Cu diffusion processed magnet as shown in Figure 6-14 obviously tells us what is happening to our magnets. Although the center region of the sample is exhibiting nice alignment of the $Nd_2Fe_{14}B$ grains with full constraint, the surface region shows a catastrophically destroy of (001) texture and the drastically increased areal fraction in Nd-rich intergranular phases. The completely distorted texture and the extremely non-uniform distribution of Nd-rich intergranular phase are the main reasons for the low remanent magnetization of the magnet diffusion processed under a fully expansion constraint (t = 0 mm) and these also resulted the poor squareness.

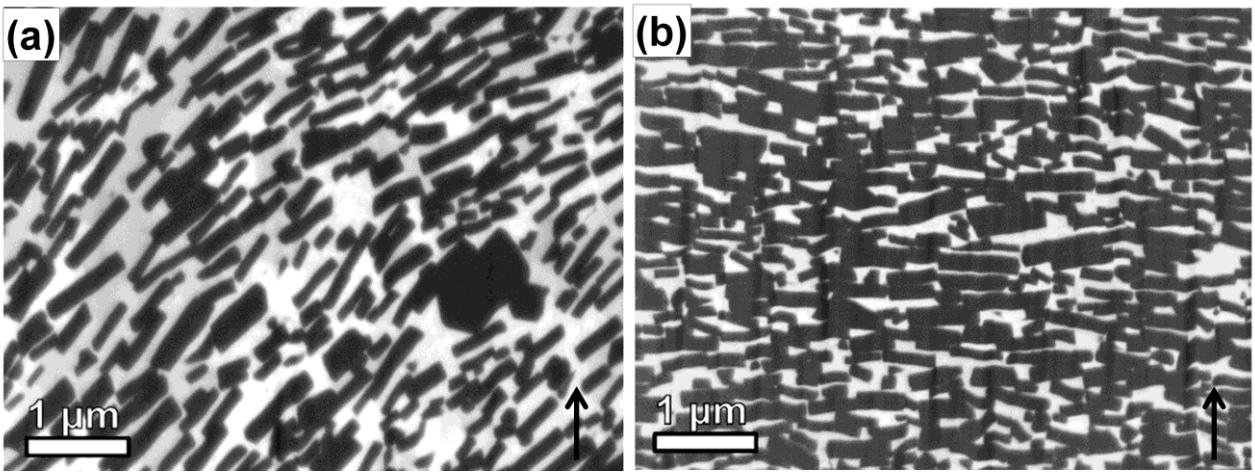

Fig. 6-14 BSE-SEM images of surface (a) and center (b) regions of the Nd-Ga-Cu diffusion-processed magnets under expansion constraint with *t*= 0 mm. The observation direction was along the easy axis as indicated by the arrows.

6.3.3 Discussion

The application of the expansion constraint during the eutectic GBDP has been proved to be effective in improving the degradation of remanent magnetization that originates from the formation of non-ferromagnetic Nd-rich intergranular phase and the distortion of (001) texture of $Nd_2Fe_{14}B$ grains. Previous report by Akiya et al [2] has considered the effect mainly was from the improvement of texture.

For the Nd-Fe-B hot-deformed magnet in the size of 5×5×4 mm^3 in the Nd-Ga-Cu eutectic diffusion process, when the expansion freedom was 0.1 mm, the remanent magnetization degradation was from 1.51 T to 1.32 T with the coercivity improved from 1.2 T to 2.03 T. While the magnet processed without applying expansion constraint exhibited the significant deterioration in remanent magnetization to 0.98 T. The in-depth characterization showed the improved distribution of Nd-rich intergranular phases from surface to center regions indicating a larger diffusion depth was achieved under the expansion constraint. There is report addressing this arises by the generated cracks by the constraint due to the different thermal expansion coefficient between the matrix phase and the Nd-rich phases. These tiny cracks would act as rapid diffusion paths and got filled in by the Nd-rich liquid during the solidifications [17]. However, the experimental evidence for this claim was not provided.

The improved (001) texture of $Nd_2Fe_{14}B$ phase was also observed in the Nd-Ga-Cu diffusion processed magnet under partial expansion constraint with 0.1 mm expansion constraint. On the other hand, the fully constraint induced a totally destroy of alignment of $Nd_2Fe_{14}B$ grains from the surface region which was in direct contact of the constraint plate. The texture distortion as seen from the SEM image is caused by the grain rotation and grain boundary sliding aided with the liquid Nd-rich phases. This effect was even enhanced probably due to the friction force introduced to the magnet surface. However, the investigation of how the grain boundary motion is carrying on during the infiltration under the full expansion constraint requires the model study by simulation, for which purpose the thermal expansion coefficient, mobility and

diffusion coefficient of the $Nd_2Fe_{14}B$ phase and Nd-rich phases will be necessary. The optimization of the expansion freedom would need to take considerations of the initial magnet dimensions, the amount of applied diffusion sources, heat treatment temperature and if possible the material of the constraint plate.

6.3.4 Conclusion on the employment of expansion constraint

Employing the expansion constraint on the eutectic grain boundary diffusion process will lead to a smaller degradation of remanent magnetization if proper expansion freedom was set for the samples Microstructural investigations have also shown the improved distribution of Nd-rich intergranular phases and the easy-axis alignment of $Nd_2Fe_{14}B$ grains with proper constraint. However, when the freedom was set as 0 mm as for the magnet in the dimension of 5×5×4 mm^3 the benefit of the constraint vanished and instead, it completely ruined the texture of $Nd_2Fe_{14}B$ phase.

6.4 Conclusion

In this chapter, the practical aspects of application of the eutectic grain boundary diffusion process to bulky Nd-Fe-B hot-deformed magnets are investigated, focusing on the Nd-Dy-Cu diffusion process on the magnet in 7×7×5.6 mm^3 and the effect of expansion constraint on the Nd-Ga-Cu diffusion process on the magnet in 5×5×4 mm^3 Major conclusions from the work of this chapter are listed as below,

(1) The eutectic GBDP using $Nd_{60}Dy_{10}Cu_{30}$ alloy shows clear merit in the coercivity enhancement compared with conventional two-alloy method, Dy metal, Dy-oxides, Dy-fluorides and also EPD process in terms of the minimization of Dy utilization;

(2) There is a large distribution in coercivity of the $Nd_{60}Dy_{10}Cu_{30}$ diffusion processed sample. As Dy-rich shell was not observed neither from surface nor center regions, this difference in coercivity was mainly attributed to the non-uniform formation of Nd-rich intergranular phases;

(3) Employment of the expansion constraint in the eutectic GBDP will restore the remanent magnetization with respect to the free expansion process only when the constraint freedom is properly designed.

References

[1] K. Löewe, C. Brombacher, M. Katter, and O. Gutfleisch, “Temperature-dependent Dy diffusion processes in Nd-Fe-B permanent magnets,” *Acta Mater.*, vol. 83, pp. 248-255, Jan. 2015.

[2]T. Akiya, J. Liu, H. Sepehri-Amin, T. Ohkubo, K. Hioki, A. Hattori, and K. Hono, “High-coercivity hot-deformed Nd-FeB permanent magnets processed by Nd-Cu eutectic diffusion under expansion constraint,” *Scripta Mater.*, vol. 81, pp. 48-51, Jun. 2014.

[3] M. Sagawa, S. Fujimura, H. Yamamoto, Y. Matsuura, and S. Hirosawa, "Magnetic-Properties of Rare-Earth-Iron-Boron Permanent-Magnet Materials," *Journal of Applied Physics,* vol. 57, pp. 4094-4096, 1985.

[4] T. Schrefl and J. Fidler, "Micromagnetic simulation of magnetizability of nanocomposite Nd-Fe-B magnets," *Journal of Applied Physics,* vol. 83, pp. 6262-6264, Jun. 1998.

[5] Y. Shinba, T. J. Konno, K. Ishikawa, K. Hiraga, and M. Sagawa, “Transmission electron microscopy study on Nd-rich phase and grain boundary structure of Nd-Fe-B sintered magnets,” *J. Appl. Phys.*, no. 5, pp. 053504, Feb. 2005.

[6] A. Sakuma, T. Suzuki, T. Furuuchi, T. Shima and K. Hono, “Magnetism of Nd-Fe films as a model of grain boundary phase in Nd-Fe-B permanent magnets,” *Appl. Phys. Exp.*, vol. 9, no. 1, Jan. 2016.

[7] S. Tanaka, H. Moriya, H. Tsuchiura, A. Sakuma, M. Diviš, and P. Novák, “First principles study on the local magnetic anisotropy near surfaces of $Dy_2Fe_{14}B$ and $Nd_2Fe_{14}B$ magnets,” *J. Appl. Phys.*, vol. 109, no. 7, 07A702, Mar. 2011.

[8] L. G. Harrison, “Influence of dislocations on diffusion kinetics in solids with particular reference to the alkahi halides,” *Trans. Faraday Society,* vol. 57, pp. 1191-1199, Jan. 1961.

[9] G. Hrkac, T. G. Woodcock, C. L. Freeman, A. Goncharov, I. Dean, T. Schrefl and O. Gutfleisch, “The role of local anisotropy profiles at grain boundaries on the coercivity of $Nd_2Fe_{14}B$ magnets,” *Appl. Phys. Lett.*, vol. 97, no. 23, pp. 232511, Dec. 2010.

[10] Y. Murakami, T.T. Sasaki, T. Ohkubo, and K. Hono,”Strain measurement from $Nd_2Fe_{14}B$ grains in sintered magnets using artificial moiré fringes,” *Acta Mater.*, vol. 101, pp. 101-106, Dec. 2015.

[11] D. I. Paul, “Extended theory of the coercive force due to domain wall pinning,” *J. Appl. Phys.*, vol. 53, no. 3, pp. 2362-2364, Mar. 1982.

[12] D. I. Paul, “General theory of the coercive force due to domain wall pinning,” *J. Appl. Phys.*, vol. 53, no. 3, pp. 1649-1654, Mar. 1982.

[13] H. Nakamura, K. Hirota, T. Ohashi, and T. Minowa, “Coercivity distributions in Nd-Fe-B sintered magnets processed by the grain boundary diffusion process,” *J. Phys. D: Appl. Phys.*, vol. 44, no. 6, pp. 064003, 2011.

[14] F. Xu, L. Zhang, X. Dong, Q. Liu and M. Komuro, “Effect of DyF_3 additions on the coercivity and grain boundary structure in sintered Nd-Fe-B magnets,” *Scripta Mater.*, vol. 64, no. 12, pp. 1137-1140, Jun. 2011.

[15] M. Soderžnik, K. Rožman, S. Kobe, and P. McGuiness, “The grain-boundary diffusion process in Nd-Fe-B sintered magnets based on the electrophoretic deposition of DyF_3,” *Intermetallics*, vol. 23, pp. 158-162, Apr. 2012.

[16] U. M. R. Seelam, T. Ohkubo, T. Abe, S. Hirosawa, and K. Hono, “Faceted shell structure in grain boundary diffusion-processed sintered Nd-Fe-B magnets,” *J. Alloy. Compd*., vol. 617, pp. 884-892, Dec. 2014.

[17] J. Liu, W. Li, Q. Wang, K. Xu, Q. Zhou, X. Zhong and Z. Liu, “The impact of pressure on the grain boundary diffusion process with NdCu alloys on Nd-Fe-B sintered magnets,” *Trans. Mater. Heat Treatment*, vol. 38, no. 7, pp. 8-12, Jul. 2017, *in Chinese*.

7 Summary and future prospect

In this thesis, the research interest has been focused on the coercivity enhancement of Nd-Fe-B hot-deformed magnets by the eutectic grain boundary diffusion process. The journey started with searching for the champion diffusion source among Nd-rich eutectics, as discussed in Chapter 3. We and a quick start given to the help of the existing binary Nd_xM_y (M=Fe, Co, Al, Ga, Cu, Mn, Zn, et al) phase diagrams. The exploration was targeted for the diffusion source which gives the largest effect on the enhancement of "saturated" coercivity. I use the word of "saturated" because in this exploration, the amount of the diffusion sources applied was giant. We completed nearly 50 sets of diffusion trials within less than 2 months and when we summarized the data, we found our champion diffusion source as $Nd_{90}Al_{10}$ alloy, which by the saturation point will give us the coercivity of ~2.6 T. Although detailed analysis show $Nd_{90}Al_{10}$ diffusion processed magnets exhibit poorer thermal stability in the aspect of temperature dependence of coercivity when the comparison was taken with $Nd_{70}Cu_{30}$ diffusion processed magnets. At 150^{o}C, they possess a same coercivity of 1.0 T even though $Nd_{90}Al_{10}$ diffusion processed magnet had higher room temperature coercivity. Nevertheless, the practice of carrying out detailed microstructural characterization of $Nd_{90}Al_{10}$ diffusion processed magnets brought me more knowledge on the Nd-Fe-B hot-deformed magnets, especially about the various types of Nd-rich phases. I had the idea of how the formation of Nd-rich intergranular phase and tuning intrinsic property (that time was Al partitioning in the $Nd_2Fe_{14}B$ phase) would give rise to the enhancement of coercivity. However, the data analysis also told us the fact of the coercivity enhancement was a trade-off of remanent magnetization, which I know from long time ago. But this seems more serious problem in the eutectic grain boundary diffusion process due to the non-uniform distribution of Nd-rich intergranular phases. This is the common phenomena which also observed in the Nd-Fe-B sintered magnets. The anisotropy of interfacial free energy between the (001) basal plane and higher-index crystal planes of $Nd_2Fe_{14}B$ grains would always cause the difference in chemistry and as a result also in crystal structure and even the interfacial feature.

We were feeling stuck due to the lack of supporting literature and spend a bit long time struggling with the optimization of $Nd_{90}Al_{10}$ diffusion process by changing the applied amount, heat treatment temperature and even with different coating method of the ribbons. The results were not included in this thesis because indeed it did not turn out well. The beak point came with the characterization work by my senior of Showa Denko's Ga-doped sintered magnets. With 0.5 at.% Ga doping, this magnet demonstrated a much larger jump in coercivity upon post-sinter annealing. This was addressed to due to the formation of thicker, uniformly distributed, more continuous Nd-rich grain boundary phase. Although at that time, the underlying mechanism of how the phase formed was not yet clarified, we were very much inspired by the observation and redirected our journey to Ga-based alloys. In Chapter 4 the comparison between the eutectic GBDP using $Nd_{62}Fe_{14}Ga_{20}Cu_5$ and $Nd_{80}Ga_{15}Cu_5$ alloys as diffusion sources indicated the unique merit of Nd-Fe-Ga-Cu to lead to a better distribution of Nd-rich intergranular phases from surface till center in the diffusion

processed magnet, i.e. a larger diffusion depth. The (001) texture of $Nd_2Fe_{14}B$ phase was also observed to be retained higher with respect to Nd-Ga-Cu diffusion processed magnets. However, the microstructure study didn't give us the evidence for possible mechanism of texture evolution during the solidification of Nd-rich intergranular phase, and $Nd_{62}Fe_{14}Ga_{20}Cu_5$ was indeed not a simple compound but a mixture of alloys. The work of Nd-Fe-Ga-Cu diffusion process actually brings the coercivity at 150^{o}C of 0.87 T with the remanence at room temperature of 1.30 T, which has already been much close our targeted magnetic properties. Although this chapter is not giving any great value of coercivity, neither it gives nice explanation of the texture evolution nor points out what kind of feature we should seek from our diffusion sources, it tells us where to go and how to think during the struggle in looking for the balance point or compromise between the coercivity enhancement and remanent magnetization.

Utilization of heavy rare earth elements (HREEs) in the eutectic GBDP was actually a compromise we made during the battle of coercivity enhancement with minimum deterioration in remanence. In chapter 5, Dy and Tb were alloyed in the Nd-rich eutectic alloys forming the ternary eutectics. We chose Nd-Dy-Al alloy for coupled effect of Dy-rich shell and the increment of anisotropy field further with Al substituting Fe in $Nd_2Fe_{14}B$ phase. The $Nd_{62}Dy_{20}Al_{18}$ diffusion processed magnets have the coercivity of 1.2 T at 150^{o}C and the room temperature remanence of 1.30 T. This work also made the investigation on the conventional Dy-vapor GBDP on the Nd-Fe-B hot-deformed magnets. We found the catastrophically abnormal grain growth in Dy-vapor processed magnet (at 900^{o}C) due to the necessary high heat treatment temperature (the typical hot-deformation temperature ~750^{o}C) and claimed that using the HREEs containing ternary eutectics as diffusion sources is probably the only way to sufficiently take advantage of the higher anisotropy field of $(HRE,Nd)_2Fe_{14}B$ phase. With Nd-Tb-Cu alloy as the diffusion source, we succeeded in retaining even higher remanent magnetization than Nd-Dy-Al diffusion process. With the average 1.05 wt.% and 1.57 wt.% of Tb in the diffusion processed magnets, the realized coercivity enhancement was 1.49 T and 1.7 T with the remanence deterioration from 1.50 T to 1.44 T and 1.38 T, respectively. Although it was no surprise that if Tb-rich structure was intruded to the surface of $Nd_2Fe_{14}B$ grains, we would gain higher coercivity or realize the same level of coercivity with smaller amount of diffusion sources, as a result, the higher magnetization would be achieved. However, when we were examining the temperature dependence of coercivity, we found $Nd_{60}Tb_{20}Cu_{20}$ diffusion processed showed an astonishingly good thermal stability as the calculated temperature coefficient of coercivity β of -0.315%^{o}C^{-1} in comparison with -0.478%^{o}C^{-1} that of the initial hot-deformed magnets. Note the typical β of HRE-free commercial sintered magnets ranges from -0.55~-0.7 %^{o}C^{-1}. Chapter 5 clearly demonstrated the merit of the eutectic GBDP as the HRE-saving method to develop the high-performance Nd-Fe-B hot-deformed magnets.

We have been already satisfactory with the results that have been achieved so far. However, all the demonstrations were made on small-sized Nd-Fe-B hot-deformed magnets. The demonstration on "bulky" magnets is crucial for enabling the eutectic GBDP feasible technique in the current commercial production lines. In chapter 6, the practical aspects in terms of limited diffusion depth and the effect of employing expansion constraint during diffusion were illustrated. Despite the large coercivity distribution of Nd-Dy-Cu

diffusion processed magnet, the achieved coercivity increase by the same amount of Dy addition is superior to the sintered magnets processed by conventional binary alloy methods, Dy metal, Dy-oxides, Dy-fluorides and even the electrophoretic deposition (EDP) of DyF_3. In the second part of Chapter 6, the expansion constraint was applied to the hot-deformed magnets, succeeding in retaining higher remanent magnetization compared to the diffusion process without constraint. Microstructural study indicated the improved distribution of Nd-rich intergranular phase from surface to center regions, i.e. more sufficient diffusion was realized by the expansion constraint. Besides, the (001) texture of $Nd_2Fe_{14}B$ grains was also found to be kept well from the initial hot-deformed magnets. Nevertheless, when the expansion freedom was set as zero for the "rigid" or "full" constraint, the benefit of restoring texture as well as the more sufficient diffusion will be diminished. Thus, the utilization of expansion constraint is a potential method for overcome the problem of limited diffusion depth and the distortion of texture but is a method needs more technical efforts to make the optimization.

The progress has been made towards the development of high-performance Nd-Fe-B hot-deformed magnets by the HRE-saving technique through the exploration of diffusion sources and the optimization of the eutectic GBDP. During the blind optimization through countless times of trial-and-error experiments, the author feel the lack of science directing the big map and the big gap between fundamental understanding and the technical problems. However, the area of magnetism and magnetic materials will be the one I would pledge my faith in and pursue more knowledge not only on technical but physical prospective.

Lihua LIU

List of Publications

First author:

1. **Lihua Liu**, H. Sepehri-Amin, T. Ohkubo, M. Yano, A. Kato, T. Shoji, and K. Hono, "Coercivity enhancement of hot-deformed Nd-Fe-B magnets by the eutectic grain boundary diffusion process", ***Journal of Alloys and Compounds***. **666**, 432 (2016). http://dx.doi.org/10.1016/j.jallcom.2015.12.227

2. **Lihua Liu**, H. Sepehri-Amin, T, Ohkubo, M. Yano, A. Kato, N. Sakuma, T. Shoji, and K. Hono, "Coercivity enhancement of hot-deformed Nd-Fe-B magnets by the eutectic grain boundary diffusion process using $Nd_{62}Dy_{20}Al_{18}$ alloy", ***Scripta Materialia***. **129**, 44 (2017). http://dx.doi.org/10.1016/j.scriptamat.2016.10.020

3. **Lihua Liu**, H. Sepehri-Amin, T. T. Sasaki, T. Ohkubo, M. Yano, N. Sakuma, A. Kato, T. Shoji, and K. Hono, "Coercivity enhancement of Nd-Fe-B hot-deformed magnets by the eutectic grain boundary diffusion process using Nd-Ga-Cu and Nd-Fe-Ga-Cu alloys", ***AIP Advances***. **8**, 056205 (2018). http://dx.doi.org/10.1063/1.5006575

Co-author:

1. H. Sepehri-Amin, Lihua Liu, T. Ohkubo, M. Yano, A. Kato, T. Schrefl, and K. Hono, "Microstructure and temperature dependent of coercivity of hot-deformed Nd-Fe-B magnets diffusion processed with Pr-Cu alloy", ***Acta Materialia***. **99**, 297 (2015). http://dx.doi.org/10.1016/j.actamat.2015.08.013

2. U.M.R. Seelam, Lihua Liu, T. Akiya, H. Sepehri-Amin, T. Ohkubo, N. Sakuma, M. Yano, A. Kato, and K. Hono, "Coercivity of the Nd-Fe-B hot-deformed magnets diffusion-processed with low melting temperature glass forming alloys", ***Journal of Magnetism and Magnetic Materials***. **412**, 234 (2016). http://dx.doi.org/10.1016/j.jmmm.2016.04.005